SYNTHESIS, CHARACTERIZATION AND APPLICATIONS OF FERRITE NANOMATERIALS AND COMPOSITES

Thesis

Submitted in partial fulfilment of the requirements for the degree of

DOCTOR OF PHILOSOPHY

By

BINDU K

(Register Number: PH13F01)

DEPARTMENT OF PHYSICS

NATIONAL INSTITUTE OF TECHNOLOGY KARNATAKA,

SURATHKAL, MANGALORE-575025

July, 2019

SYNTHESIS, CHARACTERIZATION AND APPLICATIONS OF FERRITE NANOMATERIALS AND COMPOSITES

Thesis

Submitted in partial fulfilment of the requirements for the degree of

DOCTOR OF PHILOSOPHY

By

BINDU K

(Register Number: PH13F01)

Under the Guidance of

Dr. Nagaraja. H. S

And

Dr. Ajith. K. M

DEPARTMENT OF PHYSICS
NATIONAL INSTITUTE OF TECHNOLOGY KARNATAKA,
SURATHKAL, MANGALORE-575025

July, 2019

DECLARATION

I hereby declare that the Research Thesis entitled **"SYNTHESIS, CHARACTERIZATION AND APPLICATIONS OF FERRITE NANOMATERIALS AND COMPOSITES"** which is being submitted to the National Institute of Technology Karnataka, Surathkal in partial fulfilment of the requirements for the award of the Degree of **Doctor of Philosophy** in **Physics** is a *bonafide report of the research work carried out by me*. The material contained in this Research Thesis has not been submitted to any University or Institution for the award of any degree.

Bindu K

(Register No. 135063PH13F01)

Department of Physics

Place: NITK, Surathkal

Date:

CERTIFICATE

This is to *certify* that the Research Thesis entitled **"SYNTHESIS, CHARACTERIZATION AND APPLICATIONS OF FERRITE NANOMATERIALS AND COMPOSITES"** submitted by **Bindu K** (Register Number: **135063PH13F01**) as the record of the research work carried out by her, is accepted as the Research Thesis submission in partial fulfilment of the requirements for the award of degree of **Doctor of Philosophy**.

Research Supervisors

Dr. Ajith K M

Associate Professor

Department of Physics

NITK, Surathkal

Date:

Dr. H. S. Nagaraja

Associate Professor and Head

Department of Physics

NITK, Surathkal

Date:

Chairman-DRPC

Acknowledgement

I would like to express my deepest appreciation to all those who provided me the possibility to complete this thesis. I express my gratitude to Dr. Nagaraja. H. S, Head and Associate professor, and Dr. Ajith K M, Associate Professor, Dept. of Physics, NITK, for their guidance and support throughout my Ph.D. Also, a special thanks to my RPAC members, Dr. Partha Pratim Das, Department of Physics and Dr. D. N. Gaonkar, Department of EEE, NITK, for their kind suggestions and support. I would like to thank Dr. M N Satyanarayana for providing LCR meter for dielectric study and Dr. N. K. Udayashankar for providing pellet press, which were helpful for my work. I would also like to thank all teaching and non-teaching staffs of Physics department for their support.

I am grateful to Dr. Justin Joyesephus, Associate professor, Department of Physics, NIT Tiruchirappalli and Dr. Prashanth Chowdhury, NAL, Bangalore for providing VSM facility. I would also like to thank Ms. Rashmi (SEM operator, NITK, Surathkal), Mr. Murari (FESEM operator, Mangalore University). I would like to thank, BIT, Bangalore for BET, STIC-SAIF, Cochin for TEM, Department of Chemistry, NITK for FTIR, Department of Chemical Engineering, NITK for TGA facility.

I would like to thank my friends, Mrs. Subahashini, Ms. Shankramma.K, Ms. Amudha. A, Mrs.Suchitra.S.M, Mr.Santhosh.T.C.M, Mr.Mahendra.K, Mr.Brijesh.K, Mr.Achyutha.K, Mr.Bharath.S.P, Dr.Jyothi.J, Mrs.Manju, Dr. Nagaraja.B.S, Dr. Devaraja.H.M, Dr. Shrisha.B.V, Mr. Dhanush Shanbhag, Dr. Shreejesh M, Dr. Santhosh Kumar A, Mr. Rizwan, Mr. Shreyas, Mr. Karthik Bhat and all my colleagues for their help and support.

A special thanks to my friends who encouraged me to join NITK and helped in everything. Last but not the least, I would like to thank my family for being with me and support me in every step of my life.

(Bindu K)

Dedicated to my family

CONTENT

List of Figures

List of tables

Abbreviations

LIB	Lithium ion battery
CNM	Carbon based nanomaterials
GO	Graphene oxide
rGO	Reduced graphene oxide
SWCNT	Single walled carbon nanotubes
MWCNT	Multi walled carbon nanotubes
DNA	Deoxyribonucleic acid
XRD	X-ray diffraction
FESEM	Field emission scanning electron microscopy
TEM	Transmission electron microscopy
CV	Cyclic voltammograms
CA	Chronoamperometry
CP	Chronopotentiometry
EIS	Electrochemical impedance spectroscopy
VSM	Vibrating sample magetometer
TGA	Thermogravimetric analysis
FTIR	Fourier transform infrared spectroscopy
GCE	Glassy carbon electrode
GCD	Galvanostatic charge-discharge
LOD	Lowest limit of detection
EDS	Energy dispersive X-ray spectroscopy
AC	Alternating current
DC	Direct current
CFSE	Crystal field stabilization energy
CNM	Carbon nano materials
EDLC	Electrochemical double layer capacitance
BET	Brunauer-Emmett-Teller analysis

Nomenclature

d	Inter planar spacing
λ	Wavelength of X-rays
ω	Angular frequency
σ	AC conductivity
δ	Dislocation density
τ	Relaxation time
χ	Magnetic susceptibility
ϵ^*	Complex dielectric constant
ϵ'	Real part of dielectric constant
ϵ''	Imaginary part of dielectric constant
Z	Complex impedance
Z′	Real part of impedance
Z″	Imaginary part of impedance
h k l	Miller indices
B	Magnetic induction
M_s	Saturation magnetisation
H_c	Coercivity
K	Anisotropy constant
k	Boltzmann's constant
F	Faraday's constant
R_{ct}	Charge-transfer resistance
C_{dl}	Double layer capacitance
R_g	Grain resistance
C_g	Grain capacitance
R_{gb}	Grain boundary resistance
C_{gb}	Grain boundary capacitance

Abstract

Iron oxide is one of the most available iron compound in nature and it has wide range of applications in day-to-day life. The 3d electrons of Fe in the ferrites are the reason for the electrical, magnetic and electrochemical properties of ferrite. Doping of ferrites with different cation influence these properties and enhances their performance in many electrochemical applications. The present thesis focused on the study of electrical and magnetic properties of doped ferrites and their applications in electrochemical supercapacitors and sensors. The electrochemical properties of ferrites are enhanced by the incorporating graphene oxide and multiwall carbon nanotubes. The preparation of *nickel and tin doped hematite nanoparticles* using microwave assisted method has been discussed. The variation in the electrical and magnetic properties of nickel doped ferrite on different concentration of nickel and annealing temperature has been studied. XRD and TGA studies showed a phase transition from hematite phase to magnetite phase on nickel doping. They form hematite phase at high temperature. In these ferrite both Fe ions and Ni ions contribute for the conduction mechanism and dielectric behaviour. Magnetic studies show the magnetization increases with increase in the nickel concentration. Tin doped ferrites prepared using microwave assisted method have rhombohedral structure. AC conductivity and dielectric constant increases with increase in tin concentration. Tin doped hematite nanoplates are antiferromagnetic in nature with high coercivity. Stannous ferrite microbes prepared using microwave assisted method has a high specific capacitance and specific sensitivity towards the H_2O_2 sensor with lowest limit of detection.

The electrical properties of *magnetite, zinc ferrite, tin ferrite and nickel ferrite nanoparticles* prepared using hydrothermal method have been studied. Zinc ferrite and tin ferrite have higher ac conductivity and lower loss factor than that of magnetite and nickel ferrite. Also, zinc ferrite and tin ferrite have high performance of sensing towards H_2O_2 than magnetite and nickel ferrite. Nanocomposite of $SnFe_2O_4$@rGO/MWCNT is studied as anode of lithium ion battery. It revealed a specific capacity of 1992 mAh/g at initial cycles and 91% coulombic efficiency. It retained 50 % of its initial capacity even after 250 cycles.

Keywords: *tin ferrite, nickel ferrite, zinc ferrite, dielectric properties, magnetic properties, supercapacitor, H_2O_2 sensor, lithium ion batteries. $SnFe_2O_4$@rGO/MWCNT nanocomposite*

`

CHAPTER 1

INTRODUCTION

1.1 Background and motivation

Nanotechnology is one of the most fascinating area of research because of its presence in every field, such as chemistry, physics, magnetism, electrochemistry, energy, and material science, etc. During the last few decades, most of the research has been concentrated on the design and development of nanomaterials, for their applications in different fields due to their unique physical, chemical, electrical, and magnetic properties. A material behaves differently than its bulk, when it sizes down to nano scale. The surface to volume ratio a material increases with a decrease in the particle size, which increases their surface activity of the material (Ma et al. 2019, Khan et al. 2017).

Because of high surface activity of nanomaterials, they are useful in an electrochemical applications. Due to the presence of more number of atoms and functional groups at the surface of nanoparticles, the number of active sites available for the interaction is more, which helps in high electrochemical activity. During the last few decades, a large number of works have been done to improve the efficiency of electrochemical storage devices and electrochemical sensors. The rapid increase in the world population requires efficient energy storage systems. Lithium ion batteries (LIB) and supercapacitors are electrochemical energy storage devices, in which chemical energy is converted into electrical energy. Compared to electrolytic energy storage devices, electrochemical energy storage devices have high energy and power density with long shelf life. Both are electrochemical cells with two electrodes, an electrolyte, and a separator. Whereas, charge storage mechanisms differ from each other. The double layer capacitance along with pseudo-capacitance is responsible for the charge storage in supercapacitors, whereas, LIB store charges by lithium-ion intercalation. For useful applications, an electrode should have high theoretical capacitance/capacity, high mechanical and chemical stability, and high cyclic stability. In commercial LIBs,

carbonaceous materials are used as anodes, due to their high reversibility and safety, which have discharge capacity of ~350 $mAhg^{-1}$. Silicon can be an alternative to carbon anodes because of its high theoretical capacity of 4000 $mAhg^{-1}$. However, the usage of silicon is hindered by few challenges, such as, huge volume change on lithiation/delithiation, formation of the unstable solid electrolyte interface (SIE), low coulombic efficiency, etc. (Liu, Zhu, et al. 2018, Qi et al. 2017). To overcome these drawbacks, various nanostructures are designed and developed by researchers, still, there is a need for research in electrode materials to improve the efficiency of supercapacitor and LIB (Qi et al. 2017).

Electrochemical sensing is another fast growing application of electrochemistry, which is important in the biomedical field. There are different methods to detect biomolecules, namely, titrimetry, spectrometry, resistive sensing, and electrochemical sensing. Among them, electrochemical sensing is more reliable, easy-to-operate, fast, cost effective, repeatable, selective and sensitive to biomolecule. The electrochemical detection approach is subdivided into two categories *viz*., enzymatic and non-enzymatic. Though, enzymatic approach is capable of detecting relatively low concentrations of biomolecules with good sensitivity, they have few drawbacks such as, high cost, instability, and low immobilization ability. The drawbacks of enzymatic sensors have been successfully addressed through non-enzymatic sensors fabricated using various materials on modified electrodes. However, obtaining very high sensitivity together with lowest detection limits on modified electrodes is a challenging task (Abo et al. 2011, Marinho et al. 2014, Chen et al. 2012).

Hydrogen peroxide and dopamine are the two important biomolecules, which have a key role in biological cycles. Hydrogen peroxide (H_2O_2) is a simple molecule, which has great importance in nature. In living organisms, it regulates diverse biological processes like, root growth, vascular remodelling, immune cell activation, and apoptosis, other than these, it has cytotoxic effects, and also, a by-product of a number of biochemical reactions. Dopamine is an amine with chemical name 3,4,-dihydroxyphenethylamine synthesized from precursor L-dopa in the brain and kidneys. Neurons release this organic chemical to send signals to other organs of the body. In brain it acts as a neurotransmitter and potent neuromodulator. It affects the brain

circuitry, neuronal plasticity, and motivated behaviour, renal and cardiovascular systems. The depletion of this in the central nervous system causes neurological diseases like Parkinson's disease, Schizophrenia, etc. Because of its physiological and pathophysiological implications, it is important to detect and monitor the dopamine levels in the body fluids (Fayemi et al. 2018, Lhommée et al. 2014).

Nanomaterials like, metal oxide nanostructures, carbon nanomaterials, metal nanoparticles, conducting polymers and composites have been studied for electrochemical applications (Khomenko et al. 2006, Hassoun et al. 2014, Zhu et al. 2015). The presence of redox couples in metal oxides makes them electrochemically active materials (Lipparoni et al. 2002). Especially, transition metal oxide nanomaterials are of great interest because of their diverse behaviour on sizing down to nano scale. In the case of transition metal oxides, as the particle size decreases, the lattice parameter increases, which leads to an increase in the unit cell volume. They can also act as excellent electroactive materials because of the presence of redox couples of metal ions in their active sites. A wide range of iron oxide nanomaterials are being studied for electrochemical applications. $MnFe_2O_4$, $NiFe_2O_4$, $ZnFe_2O_4$, $CoFe_2O_4$ etc. exhibit good electrochemical properties and are studied for their applications in supercapacitors, LIB, electrochemical sensors, electrocatalytic and photocatalytic water splitting, etc. (Gao et al. 2017, Chen et al. 2016, Taffa et al. 2016). Tin doped hematite and nickel doped hematite have proved to be efficient catalysts for photocatalytic water splitting applications. Also, $NiFe_2O_4$ and carbon nanomaterial composites show a good performance as electrochemical electrodes in energy storage devices and sensors.

Transition metal oxide nanomaterials have wide number of applications in many areas, which include, magnetic memory devices, catalysis, electrochemical energy conversion and storage devices, electrochemical sensors, biomedical applications, etc. Transition metal oxide nanomaterials are being studied for electrochemical applications due to their lower redox potential, multivalent redox couples, compatible morphology, high specific surface area, high mechanical and chemical stability and low cost of production (Huang et al. 2015, Wang et al. 2002, Dai et al. 2018). RuO_2 was the first metal oxide based electrode material used for supercapacitor and battery, which has high theoretical specific capacity of 806 $mAhg^{-1}$ (Subramanian et al. 2004, Choi et al.

2004). But its toxic nature and high production cost lead researchers to investigate other transition metal oxides for these applications (Rajendra Prasad et al. 2004, Liu, Luo, et al. 2018, Wang et al. 2015, Fan et al. 2017, Chen et al. 2015). Among other transition metal oxides, iron oxides are the centre of interest due to their unique magnetic, electric, dielectric and magnetic properties along with their non-toxic nature. In addition, transition metal ferrites, like Fe_3O_4, Fe_2O_3 etc. show superparamagnetic relaxation below their critical size (Salunkhe et al. 2016, Medvedeva et al. 2017, Kalaie et al. 2016, Mikhaylova et al. 2004, Bødker et al. 2000). A detailed study of dielectric and magnetic properties of both nickel and tin doped iron oxides are discussed in the present work. In addition, electrochemical applications of different ferrites and composites are discussed.

1.2 Structure and properties of iron oxides

A brief introduction to the structural, electrical and magnetic properties of Magnetite (Fe_3O_4) and hematite (α-Fe_2O_3) is discussed in this section.

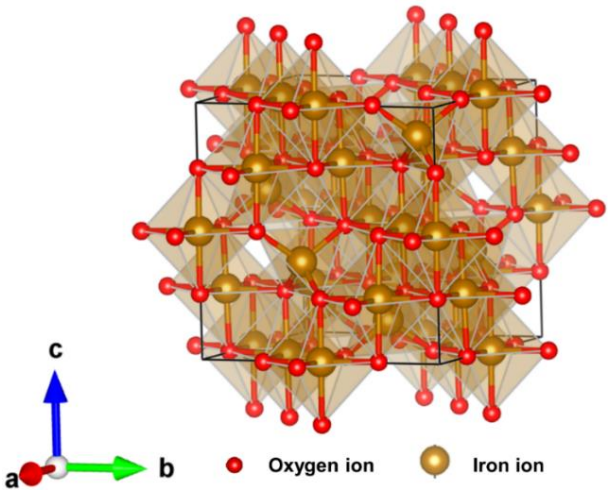

Figure 1.1. Unit cell of magnetite

Magnetite (Fe_3O_4) belongs to O_h^7 , $fd\bar{3}m$ space group, with face centred cubic crystal structure. The spinel compounds are made up of a closely packed array of anions with in equivalent tetrahedral (A) and octahedral (B) cation sites, which differ in oxygen coordination. A general formula for a spinel ferrite can be written as AFe_2O_4, where A is the metal cation (Skinner et al. 2007). 8 out of 64 tetrahedral sites and 16

out of 32 octahedral sites are occupied by iron ions in a unit cell of cubic magnetite. The distances between anions, cations and anion-cation may vary by the displacement of anions from their ideal position. These distances play an important role in the ion interactions. A unit cell of magnetite is shown in the Figure 1.1.

3d electrons of the Fe decide the electronic, magnetic and spectroscopic properties of ferrites. In a solid, the electrons of iron ion interact with other ions, which can change its energy states. In iron oxides, the cations are coordinated tetrahedrally or/and octahedrally to the negatively charged O^{2-}/OH^- ions and the d-orbitals of Fe atom experience an attraction because of the electrostatic field arising from these ligands. This results in the splitting up of the five d-orbitals into two sets of energy levels namely, t_{2g} (d_{xy}, d_{yz}, d_{zx}) and e_g (d_{z2}, d_{x2-y2}) as shown in Figure 1.2. t_{2g} and e_g sets have lower energies at octahedral and tetrahedral sites respectively. Fe^{3+} is always have a high spin state regardless of its position. The crystal field stabilization energy Fe^{3+} is zero for high spin octahedral site and 2Δ for low spin octahedral and high spin tetrahedral sites. The crystal field stabilization energy of Fe^{2+} is 2/5Δ, 12/5Δ and 3/5Δ for high spin octahedral, low spin octahedral and high spin tetrahedral sites respectively. This energy influences the thermodynamical properties of iron oxides (Liu et al. 2017).

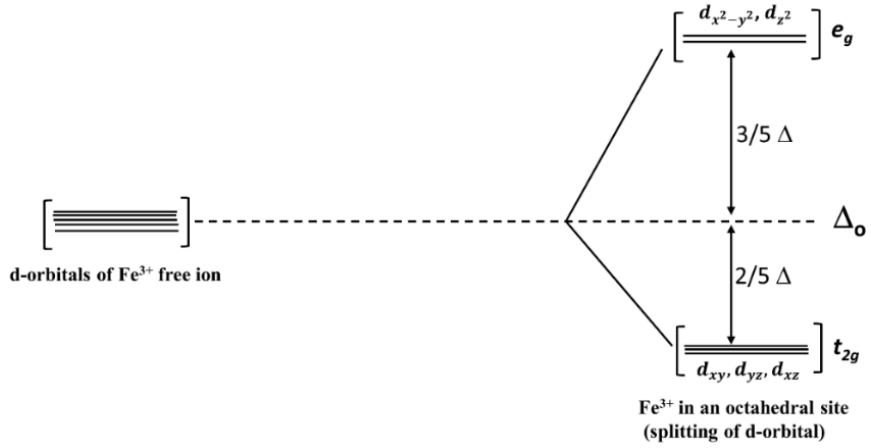

Figure 1.2 d-orbital splitting of Fe^{3+}ion in octahedral site.

Magnetite possesses both n and p-type semiconducting properties with the smallest band gap of 0.1 eV and lowest resistivity of among all iron oxide. The Fe^{2+}

and Fe^{3+} ions in the octahedral sites of edge sharing octahedra are close together and holes migrate easily from Fe^{2+} to Fe^{3+}, which leads to the good conductivity. The thermal delocalization of electrons near the Fe^{3+} and Fe^{2+} ions is also responsible for high conductivity of magnetite, whereas, maghemite (γ-Fe_2O_3) is an n-type semiconductor with a bandgap of 2.03 eV.

Magnetite exhibits a ferrimagnetic behaviour at room temperature. In magnetite, Fe^{3+} ions occupy both tetrahedral (A) sites, and Fe^{2+} ions occupy only octahedral (B) sites, which form two interpenetrating magnetic sublattices. Fe_A-O-Fe_B antiferromagnetic coupling is stronger and it is the main type of magnetic interaction in Fe_3O_4 structure. Below T_c (i.e. 850 K) the electron spins are antiparallel with an unequal magnitude, which results in ferrimagnetism (Coey 1988).

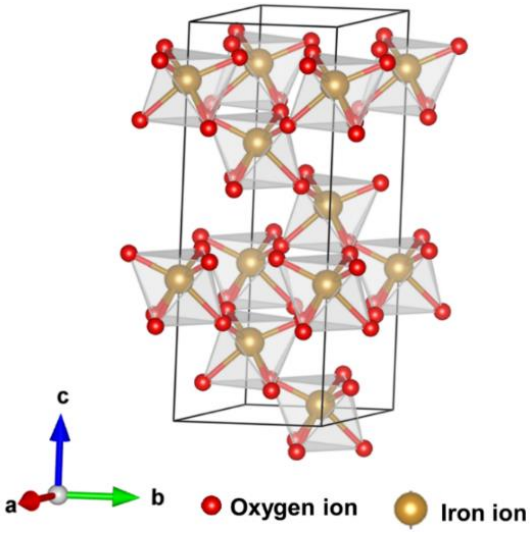

Figure 1.3 Unit cell of hematite with hexagonal symmetry.

Hematite is the most stable form of oxide among all iron oxides with a chemical formula α-Fe_2O_3. Hematite crystallizes to a rhombohedral structure with lattice parameters, a=0.5427 nm and α= 55.3° and a unit cell of hematite consists of two formula units. Hematite can also indexed to the hexagonal symmetry with a=0.5434 nm and c=1.375 nm, and a unit cell consists of six formula units. A unit cell of hematite with hexagonal symmetry is shown in Figure 1.3. The structure of hematite consists of hexagonally close packed oxygen ion arrays stacked along [001] direction and planes

of these oxygen anions are parallel to (001) plane. Only 2/3rd of the sites are filled with Fe^{3+} ions in a regular manner, with two filled sites followed by one vacant site (Tamirat et al. 2016).

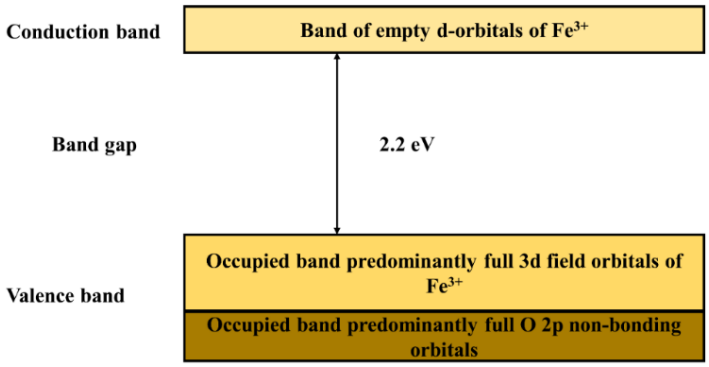

Figure 1.4 Band diagram of hematite (Zhang et al. 1993).

A stoichiometric hematite is an n-type semiconductor with a band-gap of 2.2 eV, in which the conduction band is made up of empty d orbitals of Fe^{3+} and the valance bands are composed of completely filled 3d ligand field orbitals of Fe with some admixture from the oxygen antibonding 2p orbitals as shown in Figure 1.4 (Coey 1988, Zhang et al. 1993).

Hematite is weakly ferromagnetic at room temperature and paramagnetic above its Curie temperature (956 K). At 260 K (Morin temperature, T_M) it undergoes a phase transition from weakly ferromagnetic to antiferromagnetic phase, and exhibits superparamagnetic relaxation in particles smaller than 8 nm (Bødker et al. 2000) . Hematite has two antiferromagnetic interpenetrating sublattices in its basal plane. A weak ferromagnetic interaction occurs because of a small distortion in the antiparallel electron spins in the sublattice and the distortion is less than 0.1°. The distorted sublattices are known as spin canted. At room temperature, spin canted effect dominates, which results in the weak ferromagnetic behaviour of the hematite. At T_M, the interaction between the dipolar anisotropy and the weak magnetic anisotropy of Fe^{3+} ions reorient the electron spins in basal plane to an angle of 7° to the c-axis. Then, the electron spins are exactly antiparallel and hematite shows antiferromagnetic behaviour. The magnetic behaviour of hematite depends on the particle size,

crystallinity and the concentration of cation substitution (Coey 1988, Cornell et al. 2003).

1.3 Substitution of cations into ferrite structure

Many ferrites are isostructural with some other metal oxides. For example, hematite (α-Fe_2O_3) is isostructural with corundum (Al_2O_3) and magnetite is isostructural with manganese oxide (Mn_3O_4). Therefore, substitution of Fe in iron oxides with different cations doesn't change their crystal structure. The possibility of other cations substituting iron ion depends on ionic radii and the valence of the cations.

In magnetite and maghemite, both octahedral and tetrahedral positions are available for the substitution of a large range of cations. Co, Ni and Zn can replace octahedral Fe^{2+} ions and distribute randomly in octahedral sites. Whereas, Mn, Cu and Cd concentrate near the surface of the crystals. On transformation from magnetite to hematite, the divalent trace elements eject and concentrate on the surface layers because of their valency and size mismatch. M^{2+} and M^{4+} cations can also substitute for Fe^{3+} in oxide structure, but substitution is usually less than 0.1 mol-mol^{-1}. In addition to ionic radii, the crystal field stabilization energy (CFSE) and the change in the lattice energy also influence the probability of a cation substituting a Fe^{2+} ions in Fe^{3+} oxides. The imbalance of charge in the structure arises on substitution by divalent or tetravalent cations because of the uptake or release of protons/electrons by substituted cations.

Most of the iron oxides and oxy-hydroxides transform to hematite structure in critical conditions like high temperatures and pressures. Magnetite and maghemite undergo phase transition to hematite on heating above 450 °C. The mechanism of phase transition of magnetite to hematite on heating can be written as (Boda et al. 2015)

$$Fe_3O_4 \overset{O_2\ 302\,℃}{\longleftrightarrow} \gamma - Fe_2O_3 \overset{500\,℃}{\longrightarrow} \alpha - Fe_2O_3 \ldots\ldots\ldots\ldots \quad (1)$$

The redox chemistry of transformation of magnetite to hematite can be written in two different oxidation reactions as follows,

$$4Fe_3O_4 + O_2 \rightarrow 6Fe_2O_3 \ldots\ldots\ldots\ldots \quad (2)$$

$$3Fe_3O_4 \rightarrow 4Fe_2O_3 + Fe \ldots\ldots\ldots\ldots (3)$$

There are approaches of doping magnetite with different cations to suppress the transition of magnetite to hematite phase. De Boer and Selwood increased the stability of maghemite phase by the substitution of Fe ions with aluminium ions (DeBoer et al. 1954). Lund et al. increased the stability of magnetite nanoparticle above 800°C by the addition of silica. The increase in the stability is due to the interaction between the magnetite and silica because of the Si^{4+} ion substitution to the Fe^{2+} ions in tetrahedral sites (Lund et al. 1982). Sidhu et al. showed the transition temperature of magnetite increase with the addition of trace amount of Co, Ni, Zn, Cu Mn, Cr and Al ions and the stability of the spinel structured magnetite nanoparticles also increased (Sidhu et al. 1978). In another work they showed that, the substitution of Fe ions with same trace elements in maghemite doesn't change the transformation but reduce the rate of transformation from maghemite to hematite (Sidhu et al. 1980). Pati et al. worked on the suppression of transition of magnetite to hematite by substituting Fe ions by different cations (S. S. Pati et al. 2012, Pati et al. 2015).

The structure of ferrites also depends on the doped cations. The substitution of iron ions by yttrium can form garnet structure or perovskite structure depending on the concentration of yttrium (Gatelytė et al. 2011). Rare earth material like La, Nd, Sm, Gd and Dy prefer octahedral sites because of their ionic radii and crystalize to normal spinel structure (Sattar et al. 1997). Substitution of iron ion by nickel ion forms inverse spinel structure, whereas substation by zinc forms a normal spinel structure. In hematite, substitution of Fe^{+2} by divalent ions like Ni can distort the structure and ions can accumulate near the grain surface of the crystals. In mixed ferrites, substituted ions distribute randomly without any preference towards the octahedral or tetrahedral sites (Atif et al. 2014).

The substitution of iron ions by multi valent ion like Sn^{4+} and Ti^{4+} ions have not been understood well. Elmoussaoui et al. suggested the inverse spinel structure for $SnFe_2O_4$ nanoparticles. They concluded that Sn^{2+} ions occupy the octahedral sites of the spinel structure and Fe^{3+} ions distribute equally between tetrahedral and octahedral sites (Elmoussaoui et al. 2012).

1.4 Literature on properties of pure and doped ferrite nanoparticles

The preparation method and physical parameters like, temperature, pressure, pH and concentration of the precursor solution, etc. influence the size of the nanoparticles, there by influencing the dielectric and magnetic properties of the iron oxide nanoparticles. The substitution of iron ions by different cations in iron oxides influences the physical, chemical, electrical, magnetic and electrochemical properties of iron oxides. The position of the substituted cation influences the properties of iron oxide and makes it applicable in many fields.

Ferrite nanoparticle below their critical size exhibit superparamagnetic behaviour. Zinc ferrite nanowires (Liu et al. 2006). Zinc ferrite nanoparticles of 3 to 4 nm, Tin ferrite nanoparticles prepared using precipitation exchange showed superparamagnetic behaviour (Elmoussaoui et al. 2012). $SnFe_2O_4$ nanoparticles prepared using co-precipitation method have inverse spinel structure with an energy band gap of 3.08 eV and they exhibit paramagnetic behaviour at room temperature (Liu et al. 2004). Wang et al. synthesized single phase polycrystalline $Ni_{1-x}Cu_xFe_2O_4$ nanoparticles using egg white method at low temperatures. The saturation magnetization increasing, while electrical resistivity, dielectric constant and permittivity are decreasing with increasing Cu^{2+} ion concentration (Wang, Li, Liang, et al. 2014).

Cu ions increases the magnetization and decreases the electrical resistivity and dielectric constant of the nickel ferrite(Wang, Li, Liang, et al. 2014). About 4% of cobalt doping increases the coercivity to 1608 Oe, which is because of the unreacted Fe ions present in the sample (Chakradhary et al. 2019). Copper doping also increases the DC conductivity and dielectric constant of nickel ferrite (Maqsood et al. 2011). Kumar S et al. prepared Mn, Ti mixed ferrites of composition $Mn_{1+x}Fe_{2-2x}Ti_xO_4$ by conventional solid -state reaction technique to study the impedance properties of the prepared ferrites. They observed the grain and grain boundary effect on electrical properties of ferrites and doping of Ti^{4+} ions reduces the porosity and results in densification in the system (Kumar et al. 2010).

Vara Prasad et al. prepared nickel ferrite nano-crystallines using sol-gel and auto-combustion method to determine the influence of preparation method on cationic distribution in ferrites. The nickel ferrite nano-crystallines find applications in data storage due to their excellent magnetic properties (Vara Prasad et al. 2018). Nickel ferrite nanoparticles with different morphologies were grown using hydrothermal method to study the effect of morphology on the magnetic properties. The magnetization of octahedron like nickel ferrite is greater than that of the sphere-like and irregularly shaped nanoparticles (Shen et al. 2018).

1.5 Literature on electrochemical applications of ferrite nanoparticles.

Ferrite finds applications in variety of fields like energy conversion and storage, electronics, waste water purification, biomedical applications, etc. The electrochemical applications like LIB anode materials, electrodes of supercapacitors, electrochemical sensors of biomolecules, etc. are the current interests of research. The doped iron oxides show good performance as electrode materials and electrochemical sensors because of their structure and cationic redox couples present in them. The presence of Fe^{2+}/Fe^{3+} and M^{2+}/M^{3+} redox couples makes iron oxides good candidates in the application of electrochemical sensors. Few examples showing high electrochemical performance of ferrites given in the table1.1.

Table.1.1 List of ferrite nanomaterials based electrochemical applications from literature.

Material and preparation method	Results	Reference
$MnFe_2O_4$ octahedrons via Triethanolamine (TEA) assisted hydrothermal route	The $MnFe_2O_4$ octahedrons delivers a large discharge capacity of 893 mA hg^{-1} at 0.1 mA-cm^{-2}, 972 mA hg^{-1} at 0.2 mA-cm^{-2} as a Li-ion battery electrode material.	(Zhang et al. 2006)

$CoFe_2O_4$ and $NiFe_2O_4$ spinel ferrites via sol-gel process based on vacuum sublimation of citrate precursor	$CoFe_2O_4$ and $NiFe_2O_4$ have high electrochemical performance. $CoFe_2O_4$ heated at 1000 °C for 24 h revealed more than 700 mAh g^{-1} capacity after 75 cycles.	(Lavela et al. 2007)
Nickel ferrite ($NiFe_2O_4$) nanoparticles prepared using hydrothermal method.	Discharge capacity of 1314 $mAhg^{-1}$ at first cycle and reduced to 790 and 709 $mAhg^{1}$ at second and third cycles respectively at a current density of 0.2 $mAcm^{-2}$.	(Zhao et al. 2007)
$NiFe_2O_4$ nanorods by co-precipitation of Ni^{2+}, Fe^{2+} and $(C_2O_4)^{2-}$ ions in a micro-emulsion solution	$NiFe_2O_4$ nanorods 600 °C have a specific capacity of 816.4 mA h g^{-1} at first cycle.	(Zhang et al. 2009)
Spinel cobalt ferrite ($CoFe_2O_4$) nano-flakes by simple chemical route from an alkaline bath containing Co^{2+} and Fe^{2+} ions.	Electrochemical properties of $CoFe_2O_4$ were studied in 1 M NaOH solution at a scan rate of 5 mVs^{-1} and it was found that $CoFe_2O_4$ has a specific capacitance of 366 Fg^{-1} with equivalent series resistance 1.1 Ω	(Kumbhar et al. 2012)
$ZnFe_2O_4$ nano-octahedrons synthesized by hydrothermal method.	$ZnFe_2O_4$ nano-octahedrons exhibit a specific capacity of 910 $mAhg^{-1}$ at 80^{th} cycle at 60 mAg^{-1} and has a reversible specific capacity of 730 $mAhg^{-1}$ after 300 cycles at 1000 mAg^{-1} current density.	(Xing et al. 2012)

Nickel ferrite ($NiFe_2O_4$) nano-crystalline particles synthesized by sol-gel combustion method.	The discharge capacity of $NiFe_2O_4$ at 0.1C was 1440 $mAhg^{-1}$ and 180 $mAhg^{-1}$ at 50^{th} cycle.	(Kumar et al. 2013)
Spinel Cobalt Ferrite ($CoFe_2O_4$) Nanoparticles	$CoFe_2O_4$) Nanoparticles exhibit a high discharge capacity of 890 $mAhg^{-1}$ at 0.1C rate. Even at high current density of 20C rate it exhibits 470 $mAhg^{-1}$.	(Mitra et al. 2014)
Nanocrystalline $NiFe_2O_4$ synthesised by sol-gel method.	Discharge capacity of nanocrystalline $NiFe_2O_4$ was 786 $mAhg^{-1}$at 0.5C rate after 100 cycles and had a high capacity of 365 $mAhg^{-1}$ at high current rate of 10C.	(Islam et al. 2017)
Nanocrystallites of three mixed ternary transition metal ferrite (MTTMF), $CuCoFe_2O_4$, $NiCoFe_2O_4$ and $NiCuFe_2O_4$	Electrochemical supercapacitance performance was studied using two electrode method. $CuCoFe_2O_4$ had the highest performance and $NiCuFe_2O_4$ had the lowest performance among them.	(Bhujun et al. 2017)
Mesoporous metal ferrites (MFe_2O_4, M = Fe, Co, Ni, Mn, Cu, Zn) nanoassemblies synthesized using solvothermal method in ethylene glycol solvent with the assistance of PEG 600 as co-solvent.	The specific capacitance of metal ferrites (MFe_2O_4, M = Fe, Co, Ni, Mn, Cu, Zn) were calculated to be 101, 444.78, 109.26, 190, 250, and 138.95 F g^{-1} respectively, at a scan rate of 2 mV s^{-1} in 3M KOH electrolyte.	(Aparna et al. 2018)

Mesoporous spinel manganese zinc ferrite nano-needles synthesized using one-pot co-precipitation method	Mesoporous spinel manganese zinc ferrite nano-needles exhibit a specific capacitance of 782 Fg^{-1} with high coulombic efficiency and long term stability. It has an energy density of 15.8 Wh kg^{-1} and a power density of 899.7 W kg^{-1}.	(Ismail et al. 2018)

1.6 Carbon based nanocomposites

The electrochemical properties of metal oxides can be enhanced by the incorporation of carbon based nanomaterials. Carbon based nanomaterials (CNM) have unique electrical, mechanical, chemical and electrochemical properties. They have wide applications in the field of sensors, catalysis, photo degradation, water purification, and energy. There are different allotropes of carbon nanostructures such as, graphene, carbon nanotubes, and fullerenes. The main carbon nanomaterials of our concern are graphene and carbon nanotubes. Graphene is a single-atom thick carbon sheet with sp2 configuration, in which carbon atoms are arranged in a 2D lattice. Graphene is an extraordinary carbon nanomaterial because of its unique properties like elasticity, stiffness and high electron mobility, surface area, thermal conductivity and mechanical strength. Carbon nanotubes are made up of rolled graphene sheets. Single walled carbon nanotubes (SWCNT) are made up of single sheet of graphene, and in multi walled carbon nanotubes (MWCNT), two or more graphene sheets are rolled coaxially. The distance between the layer of two adjacent tubes is nearly equal to the inter layer distance of graphite layers i.e. 0.34 nm. The diameter and length of CNTs are 2-2.5 nm and few microns respectively.

In metal oxide-CNM nanocomposites, the carbon material either acts as a functional component or a substance for immobilization of other components. In the case of graphene composites, graphene facilitates the mechanical strength, charge transfer and redox reaction, because of its large surface area and conductive structure. In the case of carbon nanotube composites, interaction between CNT and attached

nanoparticles contributes to the unique physical and chemical properties. Carbon nano material-metal oxide nanocomposite can be tailored to exhibit electrical, magnetic and optical properties of guest metal oxide nanoparticles, along with the functional properties of carbon nano structure. The electrochemical properties of these materials facilitate modulation of their charge transfer properties and aid in the design of catalyst for electrochemical, water splitting, electrodes of supercapacitors and LIB. Some examples of ferrites/CNM composites based electrochemical applications are given below.

$ZnFe_2O_4$-Graphene quantum dots prepared using hydrothermal method were tested as DNA sensor. The composite possesses higher peroxidase-like activity. The sensor exhibited lowest limit of detection of 6.2×10^{-17} M DNA, which is due to the unique properties of GQDs and the synergistic effect of the GQDs and $ZnFe_2O_4$ (Liu et al. 2014).

Santhosh et al. synthesized graphene/ manganese ferrite ($MnFe_2O_4$-G) composite by a solvothermal process. This was tested for the adsorption of lead and cadmium ions and the antibacterial activity. $MnFe_2O_4$-G composite revealed more adsorption capacity and antibacterial activity compared to graphene (Chella et al. 2015).

Li et al. 2014 synthesized $CoFe_2O_4$/Graphene nanocomposite by in situ one step hydrothermal method and studied the performance of this material as anode for Li-ion batteries. They got a high reversible specific capacity up to 937.73mAhg^{-1} with high charge/discharge reversibility at current densities of 1000mAg^{-1}. They concluded that the composite offers a fast diffusion of Li-ions and low internal resistance (Li et al. 2014).

Yang et al. 2015 synthesized $ZnFe_2O_4$/ reduced graphene oxide nanocomposite using hydrothermal synthesis to enhance the microwave absorption properties of reduced graphene oxide. They concluded that, $ZnFe_2O_4$/RGO nano-hybrids exhibit enhanced microwave absorption properties, showing great promise as a microwave absorption material to minimize the harmful effects of EMI at high frequency bands (Yang et al. 2015).

1.7 Scope and objectives

Ferrites are excellent materials with unique electrical, magnetic and electrochemical properties. The presence of redox couples makes them useful in electrochemical applications. Tin and tin oxides are excellent electrochemically active materials because of multivalent Sn-ion (Sn^{2+}/Sn^{3+}) in it. The doping of Sn ion to ferrites enhances their electrochemical properties. Nickel doped and tin doped Fe_2O_3 have been extensively studied by researchers as photo-catalyst for water splitting, but their dielectric properties needs to be studied thoroughly.

1.7.1 Objectives

Objectives proposed are,

1. The preparation of MFe_2O_4 [M- metal cation] nanostructures and MFe_2O_4-CNM (Carbon nano materials) composites using various chemical methods
2. The structural and compositional characterizations of prepared samples
3. The study of electrical, dielectric and magnetic properties of the prepared samples
4. The study of electrochemical properties of prepared metal ferrites
5. The applications of the metal ferrites and metal ferrite composites in electrochemical sensors and energy storage devices-supercapacitors and Li ion battery electrode.

1.8 Outline of the thesis

Chapter 1: This chapter gives an introduction to properties and applications of ferrites (hematite and magnetite) and their carbon nanocomposites. The literature on the properties of pure and doped ferrite nanoparticles and their applications in electrochemical supercapacitors, sensors and lithium ion batteries are included in this chapter.

Chapter 2: The principles of working and theoretical background of the experimental methods used are discussed in this chapter.

Chapter 3: This chapter discusses the preparation of nickel and tin doped ferrite nanomaterials using microwave assisted method. The dielectric and magnetic properties of the prepared samples are discussed in detail.

Chapter 4: The preparation of different spinel ferrites (Fe_3O_4, $ZnFe_2O_4$, $NiFe_2O_4$ and $SnFe_2O_4$) using hydrothermal method, their dielectric properties and application in hydrogen peroxide sensor are discussed in this chapter.

Chapter 5: This chapter consists of preparation of Fe_2O_3 nanorods and $SnFe_2O_4$ microcubes using microwave assisted method and $SnFe_2O_4$@rGO/MWCNT nanocomposites using hydrothermal method. Fe_2O_3 nanorods and $SnFe_2O_4$ microcubes based supercapacitors and hydrogen peroxide sensor are discussed. Also, $SnFe_2O_4$@rGO/MWCNT nanocomposites based dopamine sensor and application as electrode for lithium ion battery are discussed.

Chapter 6: Overall summary and conclusion of the thesis along with the future direction is given in this chapter.

CHAPTER 2

Experimental Methods and Theoretical Background

This chapter explains the theory and methodology of the various experimental techniques used in the present work. A brief introduction on the hydrothermal and microwave assisted methods is given, which is used for preparation of ferrite nanoparticles. The characterization techniques include X-ray diffraction (XRD), Thermogravimetric analysis (TGA), field emission scanning electron microscopy (FESEM), transmission electron microscopy (TEM), Brunauer-Emmett-Teller (BET) surface area analysis, Impedance spectroscopy, dielectric spectroscopy and vibrating sample magnetometers. Cyclic voltammetry, electrochemical impedance spectroscopy, galvanostatic charge-discharge, and chronopotentiometry were used for applications. Working principles and construction of supercapacitor, electrochemical sensors and lithium ion batteries are discussed.

Chemicals used in this work along with chemical formula are given in the list below and all are procured from Sigma Aldrich,

Chemical name	**Chemical formula**
Iron sulphate heptahydrate	$FeSO_4\ 7H_2O$
Tin chloride dehydrate	$SnCl_2\ 2H_2O$
Nickel acetate dehydrate	$Ni(CH_3CO_2)_2{\cdot}2\ H_2O$
Zinc acetate dehydrate	$Zn(CH_3CO_2)_2{\cdot}2\ H_2O$
Hydrazine hydrate	$N_2H_4\ H_2O$
Sodium hydroxide	NaOH
Hydrogen peroxide	H_2O_2
Dopamine hydrochloride	$C_8H_{11}NO_2\ HCl$
Uric acid	$C_5H_4N_4O_3$
Ascorbic acid	$C_6H_8O_6$
Dextrose	$C_6H_{12}O_6$

2.1 Preparation methods

The structure, morphology, physical and chemical properties of iron oxides depend on the preparation method and conditions of the experiments. One can obtain nanoparticles of desired properties by the proper selection of preparation method and control parameters. In this work, we have selected hydrothermal method and microwave assisted method because of their simplicity and control on the properties by varying the experimental parameters.

2.1.1 Hydrothermal method:

The word “hydrothermal”, means ‘hydro (water)’ and ‘thermal (heat)’, it is a chemical synthesis technique of single crystal and nanoparticles. In hydrothermal method, material crystallizes in water medium at high temperature and high vapour pressures. If the solvent used is other than the water, the method is known as “solvothermal” synthesis (Deng et al. 2003).

Figure 2.1 Stainless steel jacket and teflon jar of a hydrothermal setup.

The hydrothermal method works on the principle that, the solubility of the reactants and the products are different. The precursors (nutrients) of the reaction are unstable at high temperature and pressure created in the autoclave and reach metastable state. When the solubility of the metastable phase reaches the saturation level, it starts crystallising. In some cases, this technique is combined with one or two other techniques to obtain desired material.

In the present work, 50 ml and 120 ml hydrothermal reactors were used. Only $3/4^{th}$ volume of the teflon jar was filled with the reaction mixture in the experiment and maintained at 180 °C. A photograph of hydrothermal reactor used is given in the Figure 2.1.

2.1.2 Microwave assisted synthesis

Microwave heating is one of the efficient mode of heating, which rapidly increases the temperature of reaction mixtures by dipolar coupling. In this method, microwaves of frequency 2.45 Hz (frequency of commercial and domestic microwave reactors) are used to irradiate the reaction mixture. The applied microwave energy gets converted to thermal energy due to rotation of water/solvent molecules for the reaction to take place. In the conventional heating methods, the reaction vessel heats up first, and then does the reaction mixture. So, there will be a temperature gradient in the initial stage of the heating process. Whereas, in the microwave heating, the reaction container doesn't heat up as it will be microwave transmitter, instead, the reaction mixture in the vessel heats up directly by absorbing microwave radiations.

In the present work, a commercial microwave oven (Samsung made) was used, of which power can vary from 100 W to 750 W. A photograph of commercial microwave oven used for experiments is shown in Figure 2.2

Figure 2.2 Commercial microwave oven used in the experiments.

2.2 Characterization Techniques

2.2.1 Structural and morphological characterization techniques

2.2.1.1 Powder X-ray Diffraction (XRD)

Powder XRD is a non-destructive technique used to study the structural properties of a material. XDR is the most reliable way to identify the material, because it is based on the long-range order of the atoms, whereas most other methods characterize the atoms and their immediate (short range) environment. It is used to study the phase, crystal structure, crystallite size, and internal stress and strain of a material. XRD technique depends on the dual nature of the X-rays. When an incident beam of monochromatic X-rays scatters from the orderly arranged atoms in the crystal, it undergoes constructive or destructive interference. The diffraction of X-rays follows the Bragg's law,

$$2d\ sin\theta = n\lambda \quad \ldots\ldots\ldots\ldots (4)$$

where, d is the inter-planar distance, θ is the reflected angle and λ is the wavelength of the X-rays. An illustration of Bragg's law is given in the Figure 2.3

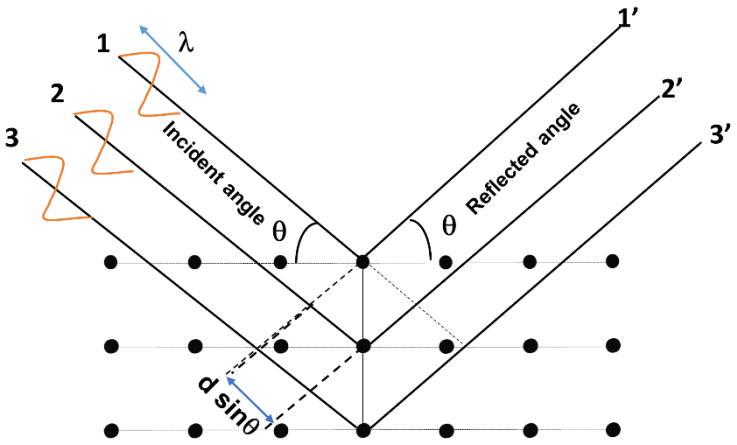

Figure 2.3 An illustration of X-ray diffraction in crystal (Bragg's law).

The powder XRD pattern is a plot of the observed diffraction intensity against the Bragg angle (θ). Depending on the interference condition, a series of reflections

produced from each atomic planes. Bragg's law ($2d \sin\theta = n\lambda$) can be used to calculate the inter-planar spacing from these diffraction patterns. A compound can be identified by its characteristic set of d values and intensities of diffracted X-rays. (Izumi, 1993)

The X-ray diffraction pattern of an iron oxide provides three parameters, viz. diffraction angle, width and intensity of the diffraction, from which the nature of the oxide, its quantity in a mixture, its cell parameter and crystallinity can be deduced. The crystal structure of an unknown compound can also be determined using XRD.

The deviation of cell parameters on substitution of other cations (different ionic radius than that of Fe^{3+}) into iron oxide can be determined using XRD. The broadening of the reflection indicates the small crystallite size and structural strain in the material. Differences in broadening of different reflections peaks provide information about the crystal shape.

The diffractogram of maghemite is identical to that of magnetite with some line shift towards higher angles, whereas the tetragonal form displays additional X-ray lines indicating a superlattice.

The lattice parameters of cubic spinel structured samples are estimated using,

$$a^2 = (h^2 + k^2 + l^2)\, d^2 \ldots\ldots\ldots\ldots (5)$$

and hexagonal structure using,

$$\frac{1}{d^2} = \frac{4(h^2 + hk + k^2)}{3a^2} + \frac{l^2}{c^2} \ldots\ldots\ldots\ldots (6)$$

The crystallite size can be calculated using Scherrer's formula,

$$t = \frac{0.9\,\lambda}{\beta\, cos\theta} \ldots\ldots\ldots\ldots (7)$$

The dislocation density can be estimated using the relation,

$$\delta = \frac{1}{t^2} \ldots\ldots\ldots\ldots (8)$$

In the present work, Rigaku mixiflex-600 X ray diffractometer (shown in Figure 2.4) was used to study the XRD. All the samples were characterized in the 2θ range of 5 to 80° under Cu-Kα (1.542 Å) radiation.

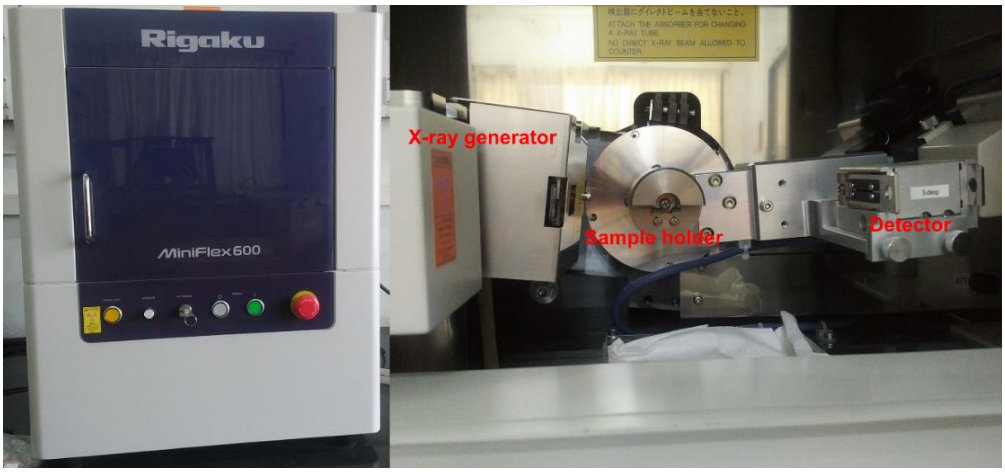

Figure 2.4 Photograph of Rigaku-miniflex 600 table top X-ray diffractometer.

2.2.1.2 Electron microscopy

An electron microscope is a microscope that uses accelerated electron beam as a source of illumination. The electrons interact with atoms of the samples to produce information signals of the samples. Electron microscopes give information about the topology and composition of samples. Transmission electron microscope (TEM) and scanning electron microscope (SEM) are two types of electron microscopy techniques. Morphology and the compositional analysis were conducted using a field emission scanning electron microscope (FESEM, *ZIESS*) fitted with an energy dispersive X-ray spectrometer (EDS). FESEM was conducted with an electron beam of kinetic energy 20 keV.

Scanning Electron Microscopy (SEM) and Transmission electron microscope (TEM)

The electron beam in SEM scans in a raster pattern and the signals detected are combined with the position of the beam to produce the image. Whereas, in TEM, the electron beam passes through the specimen to form a microscopic image. When, the incident electron beam enters the specimen, various signals are emitted from the

specimen. Different types of electronic interaction with a specimen. Signals from the interaction of electron beam with the specimen are,

- Secondary electrons
- Back scattered electrons
- Cathodo-luminescence
- X-rays
- Auger electrons

These signals are utilized by the SEM and TEM to observe and analyse the surface or just beneath the surface of the specimen. SEM is a versatile instrument, which can be used for the elemental analysis and state analysis along with simple morphological observation. TEM can be used study the plane arrangement and core structure of the sample.

Energy Dispersive X-ray Spectrum (EDS)

When the incident electron beam enters the specimen, electrons and electromagnetic waves are emitted from the specimen. When electrons in the inner shells of the constituent atoms of the material are emitted, the vacant orbits are filled with the outer-shell electrons, then the substance emits the characteristic X-rays corresponding to the energy difference between the outer-shell and inner-shell. These can be used for the elemental analysis, which is the principle of the Energy Dispersive X-ray Spectrometer (EDS). A qualitative analysis can be performed to identify the constituent elements of a specimen using the X-ray spectra. Three modes of EDS are available namely, point analysis, line analysis and area analysis (or mapping). Point analysis gives the spectrum from a point of interest, line analysis gives distribution of elements in one-dimension on a specified line of interest and mapping displays the elemental distribution in two dimensions for a specified area of interest.

2.2.1.3 Fourier Transform Infrared Spectroscopy

Infrared spectroscopy is an important analytical technique used to identify the presence of functional groups and vibrational bonds in a molecule. When an infrared

light of frequency ranging from 4000 cm^{-1} to 200 cm^{-1} passes through a material, some of the radiations get absorbed and some will be transmitted. The resultant spectrum is the IR spectrum of the material. The molecules in the material absorb their characteristic frequencies. The absorbed frequencies represent the vibrations bonds between the atoms of the molecule. Since each material is made up of different atoms and bonds, IR spectrum is a fingerprint of the material. Both qualitative and quantitative identification of different kinds of material is possible using the FTIR spectroscopy.

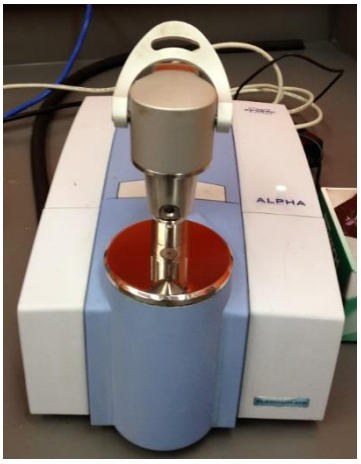

Fig 2.5 Photograph of Bruker Alfa FTIR spectrometer.

FTIR technique was used to find out the characteristic vibrational bond of the prepared iron oxides. Fourier transform infrared (FTIR, *Bruker Alfa FTIR spectrometer,* Figure 2.5) spectra were recorded from 400 to 4000 cm^{-1} using KBr pellet.

2.2.1.4 Thermogravimetric analysis

In thermal analysis, the properties of a material are studied as a function of applied temperature. Thermal analysis can be done to monitor endothermic and exothermic processes of the material. Thermal gravimetric analysis or thermogravimetric analysis (TGA) is one of the very important and widely used techniques of thermal analysis. In TGA, the mass of the sample is measured as a function of temperature or time in a controlled atmosphere. The change in the mass on increasing temperature can be attributed to the physical or chemical changes in the

material. TGA instrument consists of a furnace with a microbalance in it and has a sample chamber, which can be purged with gases like nitrogen, oxygen or air to maintain the required atmosphere. Change in the sample weight can be measured as a function of time and temperature. TGA helps us to find out the thermal stability, melting point, transition temperature of the material. A schematic diagram of construction of TGA instrument is given in the Figure 2.6.

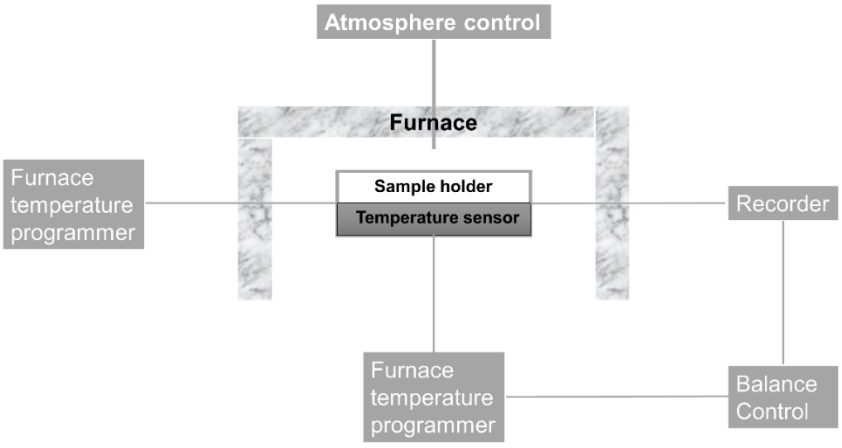

Figure 2.6 A schematic diagram of TGA instrument.

Thermal studies using both thermogravimetric analysis (TGA) were conducted using a TGA-DSC (*DSC SDT Q600*) system under nitrogen atmosphere by heating the samples from room temperature to 800 ˚C.

2.2.1.5 Brunauer, Emmett and Teller (BET) surface area analysis

The specific surface area of the samples can be calculated using Brunauer, Emmett and Teller (BET) method. This works on the basis of physical adsorption of a gas on the solid surface. The amount of gas adsorbed on the surface as a monolayer can be used to determine the specific surface area of the solid. It is also dependent on the temperature, pressure and the interaction of the gas with the surface. The specific surface area, pore volume and pore diameter of the samples were evaluated using a BELSORP mini II instrument (*BEL Japan Co., Ltd*) by the nitrogen adsorption-desorption isotherms.

2.2.2 Electrical characterization techniques

Electric and dielectric characterization of the samples were done using HIOKI LCR meter with the bias voltage of 2 V. A photograph of LCR meter and two-probe station used is given the Figure 2.7(b). Prior to electrical studies, powder samples were made into pellets of 1 cm dia using a hydraulic press (Indfurr, Chennai, India made, shown in Figure 2.7(a)).

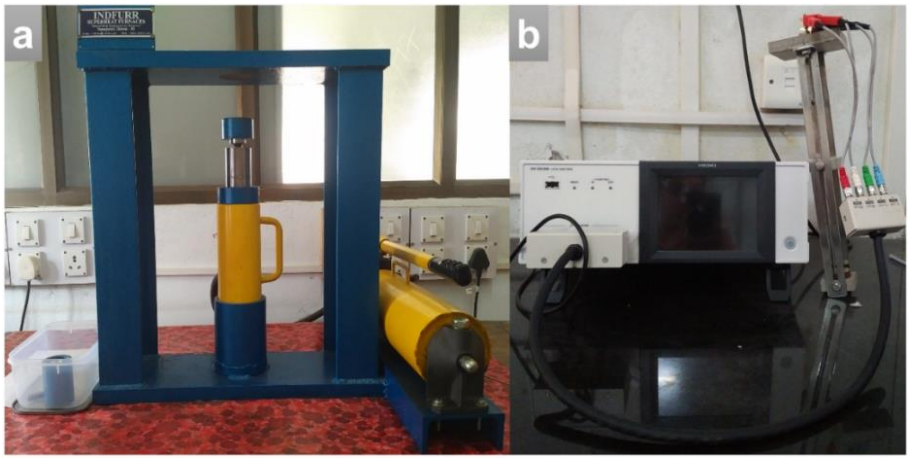

Figure 2.7 Photographs of (a) hydraulic press and (b) Hioki LCR meter.

2.2.2.1 Impedance spectroscopy

AC impedance spectroscopy is a method, which can be used in dielectric and electrochemical systems. In this method, an electric field is applied and the impedance of the system with respect to the frequency of the applied field is recorded. In electrical systems, it helps us to separate the contribution of different components to the impedance. We can understand the dielectric properties of the material with known dimension. Impedance spectroscopy is a non-steady-state measuring technique, which can be used to study the electrode kinetics of complex electrochemical system.

In impedance spectroscopy, when we apply an excitation of sinusoidal potential, a pseudo-linear AC signal is obtained as the response. The impedance of the sample for the applied monochromatic alternating potential $U(t)$ is,

$$Z = \frac{U(t)}{I(t)} = |Z|e^{i\varphi} = Z' + jZ'' \ldots\ldots\ldots\ldots \quad (9)$$

Where, *I(t)* is the resulting current, φ is the phase difference of alternating field, Z′ is the real part and Z″ is the imaginary part of the complex impedance. The admittance Y can be written as,

$$Y = \frac{1}{Z} = Y' + jY'' \ldots\ldots\ldots\ldots \quad (10)$$

Further, Z′ (R) is the resistance, Z″ (X) is the reactance, Y′ (G) is the conductance and Y″ (B) is the susceptance.

The amount of energy loss relative to the energy loss of the system is known as quality factor and define as, $Q = \left|\frac{Z''}{Z'}\right|$ *or* $\left|\frac{Y''}{Y'}\right|$ and the loss factor 'D' can be written as, $D = \frac{1}{Q} = tan\delta$, where δis the loss angle of the system under study.

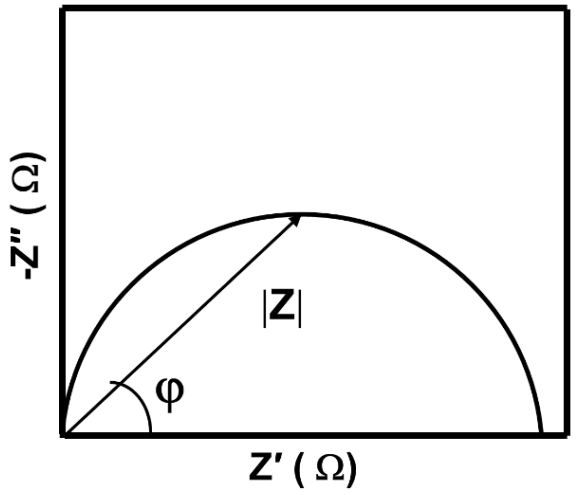

Figure 2.8 Representation of Nyquist plot.

A plot of imaginary impedance versus real impedance is called as 'Nyquist plot' (shown in Figure 2.8). Impedance at a frequency on the Nyquist plot can be represented as a vector of length $|Z|$. The angle between the X-axis and $|Z|$ is known as phase angle. The semicircle a Nyquist plot is the characteristic of a single time constant with

$$\tau = \frac{1}{2\omega} = \frac{1}{2\pi f} \ldots\ldots\ldots\ldots (11)$$

where 'τ' is the relaxation time, ω is the angular frequency.

EIS data can be generally analysed by fitting to an equivalent circuit model with simple electrical Components. Common electrical components in the most of the models are resistors, capacitors and inductors.

The relations that can be used to fit the equivalent circuits are,

$$Z' = R_s, Z'' = {}^{-1}/_{(\omega C_s)} \ldots\ldots\ldots\ldots (12)$$

$$Y' = {}^{1}/_{R_p}\ , Y'' = \omega C_p \ldots\ldots\ldots\ldots (13)$$

$$R_p = R_s\left(1 + {}^{1}/_{tan^2\delta}\right) \ldots\ldots\ldots\ldots (14)$$

$$C_p = C_s/(1 + tan^2\delta) \ldots\ldots\ldots\ldots (15)$$

Where, R_s and R_p are series and parallel resistances respectively, and C_s and C_p are series and parallel capacitance respectively.

Generally, resistors and capacitors of an equivalent circuit represent a physical parameter of the system under study. In electrochemical system, solution resistance, charge transfer resistance, constant phase angle, and double layer capacitance can be distinguished using equivalent circuit models. While in solid state system, the contribution of grains, grain boundaries, bulk properties like particle size, electrode material, etc. can be distinguished using equivalent circuit parameters (Mansour et al. 2017).

Electric modulus is one of the important formalisms for the study of conduction and relaxation behaviour of ceramic materials. The real part (M') and imaginary part (M″) of complex modulus M^*, explain the energy given to the system and the energy dissipated from it during conduction process respectively (Farid et al. 2017, Nobre et al. 2003),

$$M^*(\omega) = \frac{1}{\varepsilon^*(\omega)} = j\omega C_o Z^*(\omega) \ldots\ldots\ldots\ldots \quad (16)$$

$$M^* = \frac{1}{\epsilon^*} = \frac{\epsilon'}{\epsilon'^2 + \epsilon''^2} + j\frac{\epsilon''}{\epsilon'^2 + \epsilon''^2} = M' + jM'' \ldots\ldots\ldots\ldots \quad (17)$$

2.2.2.2 Dielectric spectroscopy

A material, which is an electrical insulator but can be polarised by applying an external electric field, is known as dielectric or dielectric material. Unlike electrical conductors, dielectric materials don't let electrical charges to flow through them, instead they let the charges to shift from their equilibrium position, which causes a dielectric polarisation. In an external electric field, positive charges displace in the applied field direction and negative charges displace in the opposite direction creating an internal electric field, which reduces the overall field within the material. The dielectric properties of the materials help us to explain the different phenomena in electronics, optics, etc. The relative permittivity (dielectric constant) is one of the important properties of a dielectric material, which is independent of the electric field strength for most of the materials, but depends on the frequency of the applied electric field, chemical structure, imperfections in the materials and physical parameters (temperature, pressure, etc.). The complex dielectric constant can be written as $\varepsilon^* = \varepsilon' + j\varepsilon''$, where ε' and ε'' are the real and imaginary part respectively. ε' and ε'' can be calculated using the relations,

$$\varepsilon' = \frac{C_d}{\varepsilon_0 A} \ldots\ldots\ldots\ldots \quad (18)$$

and

$$\varepsilon'' = \varepsilon' \tan\delta \ldots\ldots\ldots\ldots \quad (19)$$

The response of a dielectric material under the varying electric field provides information about the structure and the dielectric behaviour. There are different kinds of polarization phenomena exists depending on the structure of the material, namely,

1. Electronic polarization or optical polarization is the displacement of outer electron cloud with respect to the positive nucleus. This can be caused by the deformation of the symmetrical distribution of electron clouds of molecules.
2. Atomic or ionic polarization is the displacement of negative and positive atoms or ions relative to each other in a polyatomic molecule in the presence of electric field. This is also known as vibrational polymerization, because it is a normal lattice vibration.
3. Orientation polarization is the alignment of dipoles in the direction of the applied electric field in a molecule with a permanent dipole moment.
4. Space charge polarization is the polarization associated with mobile and trapped charge carriers, in which migration of charges towards the grain boundaries and interfaces occurs.
5. Hopping polarization is the jumping of localized charge carriers from one cationic site to another.

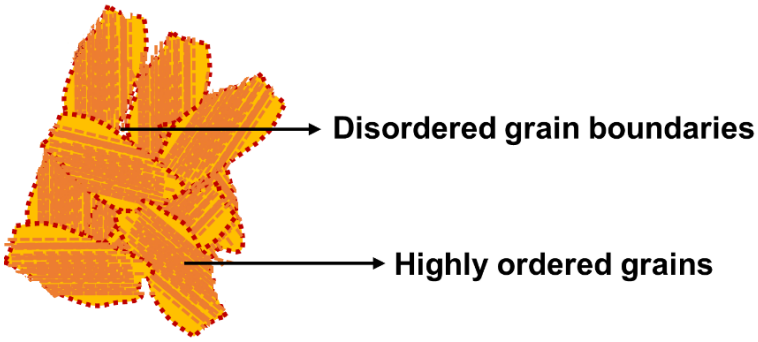

Figure 2.9 Schematic representation of Maxwell-Wagner bilayer arrangement of grains and grain boundaries.

Iron oxides exhibit space charge polarization and hopping polarization under the influence of external electric field. The polarization phenomena and dielectric properties of iron oxides depend on the doped cations, preparation method, temperature, frequency of the applied electric field, etc. The AC conductivity and dielectric properties of iron oxides can be explained on the basis of Maxwell-Wagner bilayer model of iron oxide with Koop's phenomenological theory. According to Maxwell-Wagner model, an iron oxide is made up of highly ordered conducting grains separated by the disordered (defective) insulating grain boundaries. When an external electric

field is applied to iron oxide, both charge carriers move towards the grain boundaries by hopping and collect at the grain boundaries, which induces the space charge polarization in it. A schematic representation of Maxwell-Wagner bilayer model is shown in the Figure 2.9.

Polarization consists of two major regimes namely, the resonance regime and the relaxation regime. When, the frequency of the applied filed is equal to the natural frequency of the hopping, the resonance occurs. It associates with the vibrations of charge carriers or atoms. The polarization associated with movement of charge carriers by the orientation or migration, belongs to the relaxation regime.

2.2.3 Magnetic characterization techniques

2.2.3.1 Magnetic properties

The magnetic properties of a material can be described as the behaviour of magnetic moment of the material in an external magnetic field. The magnetic moment of a material arises due to the interaction between the spin moment of an electron and the orbital moment. If we consider a material in an external magnetic field of strength H, then the magnetic induction B of the material can be written as,

$$B = \mu\,(H + J) \ldots\ldots\ldots\ldots \quad (20)$$

where, μ is the magnetic permeability and *J* is the magnetic moment of the material per unit volume. The magnetic moment '*m*' and susceptibility 'χ' of the material are related by the equation,

$$\chi = \mu_o \frac{Nm^2}{3kT} \ldots\ldots\ldots\ldots \quad (21)$$

where, *N* is the Avogadro's number, *k* is the Boltzmann constant and μ_o is the permeability of free space.

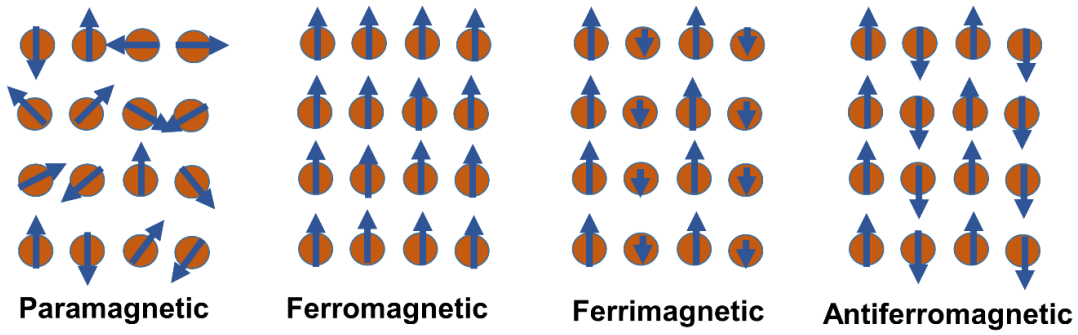

Figure 2.10 An illustration of arrangement of magnetic moments in different types of magnetic materials.

Magnetic materials can be classified as, diamagnetic, paramagnetic, ferromagnetic, antiferromagnetic and ferrimagnetic materials. A diamagnetic material repel the magnetic field applied. In a paramagnetic material, magnetic moments are oriented randomly and net magnetic moment is zero in the absence of external magnetic moment. The relative magnetic permeability of paramagnetic material is greater than one. In a ferromagnetic material, all magnetic moments are aligned in a single direction even in the absence of external magnetic fields. Whereas, in a ferrimagnetic material, two magnetic moments with different magnitude will be aligned in opposite directions, there will be a net magnetic moment because of the different strength of the moments. If a material has magnetic moments of same strength aligned opposite to each other, then the net magnetic moment is zero, and the material is known as antiferromagnetic. The alignment of magnetic moments in different types of material are illustrated in the Figure 2.10.

The ferromagnetic, antiferromagnetic and ferrimagnetic materials exhibit magnetic domains. Only the nanoparticles having dimensions less than 500 nm consists of single domain and the particles larger than that have multi domain structure. Within a domain, spins are oriented either parallel or antiparallel to each other, but they are oriented in different directions in different domains. A high external magnetic field can remove the domains in ferrimagnetic and antiferromagnetic materials. As the strength of the external magnetic field increases, all spins in domains orient in the direction of the applied magnetic field and reach saturation magnetization.

Fe^{3+} is a high spin ion with five unpaired d electron and zero angular momentum. The magnetic momentum of Fe^{3+} is 5.9 Bohr magneton (BM) from both theoretical and experiment. Whereas, Fe^{2+} ion has a measured magnetic moment of 5.1 to 5.5 BM, which is different from its theoretical magnetic momentum (i.e. 4.9 BM). The difference in this theoretical and experimental values of magnetic moments of Fe^{2+} ion is due the contribution from orbital angular moment.

The unpaired electrons of Fe 3d shell are responsible for the strong moment of iron atom and iron compounds. Fe^{2+} ion has 4 unpaired electrons and Fe^{3+} ion has 5 unpaired electrons in 3d shell. These unpaired electrons are responsible for the magnetic states of iron compounds. In iron compounds, the electrostatic exchange interaction between Fe ions on adjacent sites is the main type of magnetic interaction, which causes parallel or antiparallel alignment of the spins. The exchange reaction proceeds through the intervening ligands, O^{2-} or OH^{-}, which is called as super exchange. The super exchange interaction depends on the Fe-O bond length and bond angle. It is stronger for the Fe^{3+} bonds with angles 120-180° and weaker for the FeO_6 octahedron that shares face with the neighbouring FeO_6 octahedron. It is same in Fe^{2+} oxides.

2.2.3.2 Vibrating sample magnetometer (VSM)

Magnetometry is a technique of measuring and mapping patterns of magnetism in the sample. The instrument that is used to measure and map the magnetic patterns of a samples is known as magnetometer. It can be used to measure magnetization, direction or relative change of magnetic field.

Basically there are two types of magnetometers, vector magnetometer, which measures the direction of a magnetic field, and scalar magnetometer, which measures the magnitude of the magnetic field. Vibrating sample magnetometer comes under the category of laboratory scalar magnetometers, which measures the magnetization by vibrating a sample mechanically inside an inductive pickup coil. In VSM, a sample is first magnetized in a uniform magnetic field and then vibrated sinusoidally using a piezoelectric transducer. The induced voltage in the pickup coil will be recorded, which is directly proportional to the magnetic moment of the sample. The hysteresis curve of a material is recorded by sweeping the magnetic field.

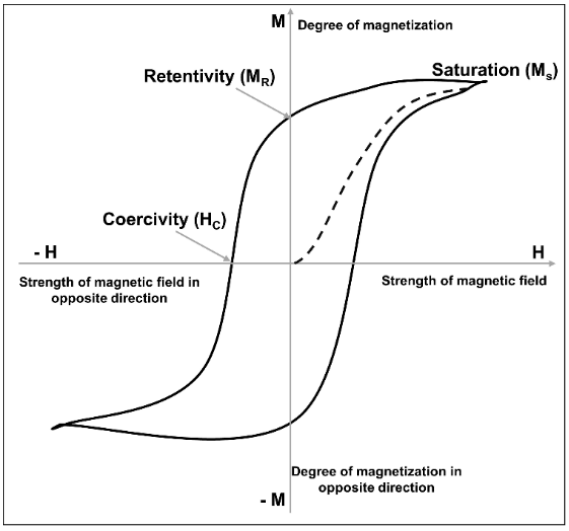

Figure 2.11 A model magnetic hysteresis (M-H) curve.

Hysteresis is the most common way of representing bulk magnetic properties of a material. It is a plot of magnetic induction (B) versus field strength (H) as shown in the Figure 2.11. Alternatively, magnetization (M) versus filed strength (H) can also be used in many case. A hysteresis curve gives the information about the type of magnetization (i.e., paramagnetic or ferromagnetic), strength of magnetic material (hard magnetic or soft magnetic material), saturation magnetization (M_s), coercivity (H_c) and retentivity (M_r) of the material. The saturation magnetization is the condition, when all of the magnetic moments in the magnetic material align themselves in the direction of the applied magnetic field, which depends only on the magnitude of the total atomic moments of the material. The retentivity is the residual magnetization in the material after the removal of external magnetic field, which helps us to distinguish between the paramagnetic and ferromagnetic materials. The coercivity is the reverse magnetic field strength (H_c) required to reduce the magnetization to zero, which strongly depends on the structural properties of a material. It is affected by the factors such as, preparation method, particle size, particle shape, etc. The coercivity is also depends on the magnetic anisotropy constant (K),

$$H_c = \frac{0.96\,K}{M_s} \quad \ldots\ldots\ldots\ldots \quad (22)$$

The magnetic properties of samples were studied by vibrating sample magnetometry using Lakeshore VSM-7404.

2.2.4 Electrochemical characterization techniques

Biologic SP-150 electrochemical workstation was used to study electrochemical properties of the prepared samples. A photograph of SP-150 electrochemical workstation with three electrode setup is given in Figure 2.12.

Figure 2.12 Photograph of SP-150 electrochemical workstation.

2.2.4.1 Cyclic voltammetry (CV)

Voltammetry is the study of current as a function of applied potential. In voltammetry experiments, potential of the electrode in contact with the analyte is controlled, while measuring the resultant current across it.

Minimum of two electrodes are required to run a voltammetry experiment. One is working electrode, to which the desired potential is applied in a controlled way, which facilitates the charge transfer between working electrolyte and analyte. The second electrode acts as the other half cell, which is used to gauge the potential of the working electrode and balance the charge added/removed from the working electrode. Two electrode setup has a number of shortcomings. Significant one being, maintaining of constant potential at counter electrode during redox reactions is extremely difficult. This problem can be solved by providing individual electrodes for the supply of

electrons and a reference potential. The reference electrode is a half cell with a known reduction potential, it acts as a reference in measuring and controlling the potential of working electrode. These three electrodes, working electrode, counter electrode and reference electrode together make the modern three-electrode system. A schematic of three electrode system is given in Figure 2.13.

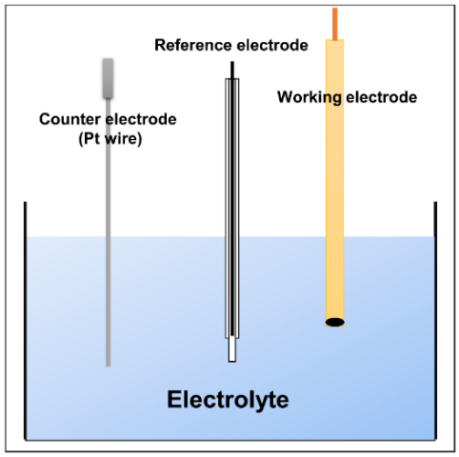

Figure 2.13 Schematic diagram of three electrode system.

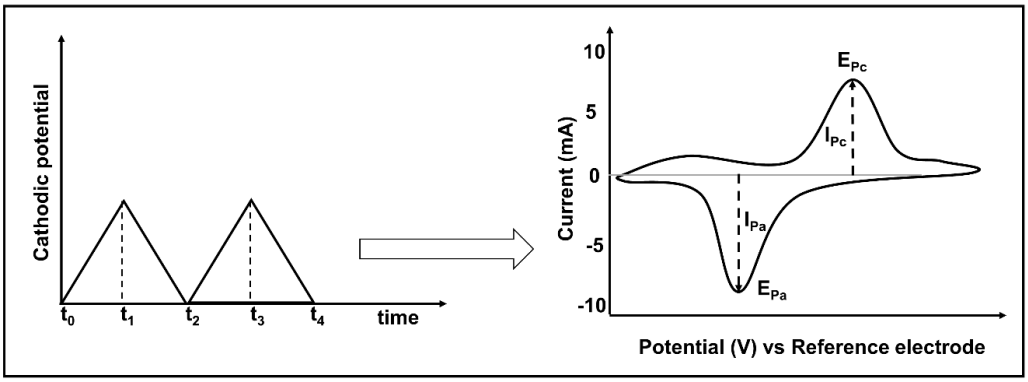

Figure 2.14 Input waveform and cyclic of cyclic voltammetry technique.

In an electrochemical system, the reaction of interest occurs at the working electrode. Depending on the redox reaction taking place at the working electrode, it is called as cathodic or anodic electrode. It is often used in conjunction with a counter and a reference electrode in a three electrode system. Using this configuration, one can measure the potential of the working electrode against a known reference without compromising the stability of the reference electrode by passing current through it.

In cyclic voltammetry, the potential of working electrode ramps linearly in cyclical phases against time as shown in figure. The potential between working electrode and reference electrode and the current between working electrode and counter electrode are measured. The rate of change of voltage with time during each phases is known as scan rate (ν). The curve of current versus potential is known as cyclic voltammogram (shown in figure 2.14). Cyclic voltammetry provides information about the kinetics of the reaction and the redox potential of the electro active species in the system. The important parameters of a CV are peak currents i.e., anodic peak current (I_{pa}) and cathodic peak current (I_{pc}) and peak potentials i.e. anodic peak potential (E_{pa}) and cathodic peak potential (E_{pc}). If the reaction is reversible, then the peak current follows the Randles-Selvik equation,

$$i_p = (2.69 \times 10^5) n^{3/2} A C D^{1/2} \vartheta^{1/2} \dots\dots\dots\dots (23)$$

where, i_p is the peak current , n is the number of electrons transferred in the reaction, A is the area of the electrodes, D is the diffusion coefficient of the analyte, C is the concentration of the analyte solution, ν is the scan rate.

For an irreversible and quasi-reversible system, the peak current can be written as,

$$i_p = (2.99 \times 10^5) n (\alpha n_a)^{1/2} A C D^{1/2} \vartheta^{1/2} \dots\dots\dots\dots (24)$$

2.2.4.2 Galvanostatic Charge-discharge (GCD)

Galvanostatic charge-discharge is an electrochemical technique used to study the mechanism and kinetics of an electrochemical reaction, along with the estimation of electrochemical capacitance of a material under the controlled current conditions. This can also be used to study the stability of the electrochemical energy storage device. In GCD, a constant current is applied to the system to charge device, and when the device reaches the cutoff potential, it will be discharged with negative current. The potential versus time curves obtained with this technique can be used to estimate the capacity of the energy storage device. Multiple charge-discharge cycles can be studied to understand the stability and coulombic efficiency of the device. A model GCD curve is shown in Figure 2.15.

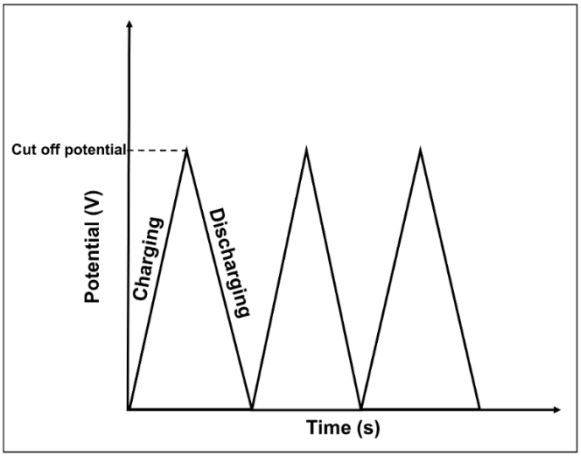

Figure 2.15 A model GCD curve of a supercapacitor/battery.

2.2.4.3 Chronoamperometry (CA)

Chronoamperometry is an analytical technique of electrochemistry used to study the current across the working electrode as a function of time, at a constant potential. This can be used to study electrochemical sensors and stability of anticorrosive coatings. This is performed by applying an initial voltage, at which no faradaic reaction is taking place. Then stepping the potential of interest, where the redox reaction takes place to give a resulting current. The current measured through the experiment can be expressed by Cotrell expression,

$$i(t) = \frac{nFAD_o^{1/2}C_o^*}{\pi^{1/2}t^{1/2}} \quad \ldots\ldots\ldots\ldots \quad (25)$$

where, *n* is the number of electrons involved in the reaction, *F* is the Faraday's constant, *A* is the area of the electrode, D_o is the diffusion coefficient of the analyte, C_o is the concentration of analyte in the solution and *i(t)* is the current at the working electrode at the time of *t*.

2.2.4.4 Chronopotentiometry

In constant current chronopotentiometry, a constant current is applied to the working electrode, which causes the electroactive species present in the electrolyte to reduce or oxidize. The potential across the working electrode will be measured as a

function of time. This technique can be used for electroplating, to study charge-discharge curves of supercapacitors and batteries, pH and electrochemical sensors.

2.3 Electrochemical applications

2.3.1 Supercapacitors

Supercapacitor is an electrochemical energy storage device with very high capacitance of 10 to 100 times more than that of regular electrolytic capacitor. It is also known as, ultra-capacitor or gold cap. Unlike regular capacitor, supercapacitor does not store charges in dielectric medium, but rather they work on the basis of electrostatic double-layer capacitance and electrochemical pseudo-capacitance. Both capacitances contribute to the total capacitance of a supercapacitor.

A supercapacitor consists of a separator, dipped in electrolyte, sandwiched between two electrodes. A schematic diagram of supercapacitor is given in Figure 2.16. When an external electric field is applied to the cell, positive and negative charges accumulate on the surfaces of the electrodes of opposite polarity. Ions in the electrolyte diffuse through the separator and form a double layer of charges at the interface of the electrode and the electrolyte.

If the electrodes are identical then the supercapacitor is called as symmetric supercapacitor. While an asymmetric supercapacitors consists of different electrodes. Supercapacitors are categorized into electrical double layer capacitors (EDLC), pseudo-capacitors and hybrid capacitors on the basis of the energy storage mechanisms. In EDLCs, the charge separation at the interface between the electrode and the electrolyte forms a Helmholtz double layer, with a thickness of about 0.3-0.8 nm, which gives a high capacitance. In an electrochemical pseudo-capacitor, Faradaic electric charge-transfer with redox reactions, electrosorption and intercalation of ions contribute to the capacitance.

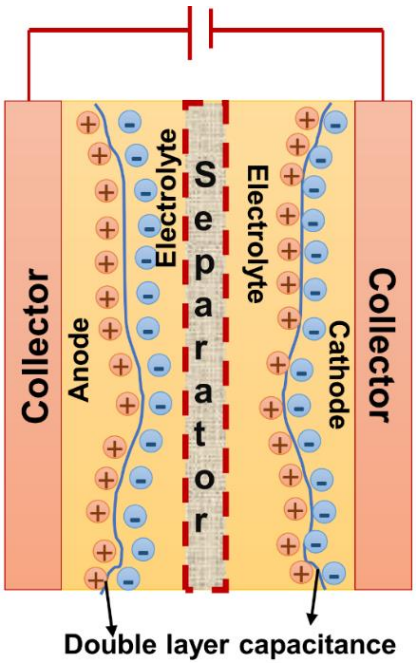

Figure 2.16 Schematic diagram of working of supercapacitor.

Electrodes: The selection of electrode material plays an important role in constructing a supercapacitor. An electrode should have high specific surface area, provide high cyclic stability, high energy density and high power density. The morphology of the electrode material also matters. A material with more specific surface area, porosity, active sites provide high performance supercapacitors. The commercially available supercapacitors use porous graphite material as electrodes. A large number of materials have been investigated as electrode materials for supercapacitor as electrode materials for supercapacitors, which include, carbon nanomaterials (graphene oxide, carbon nanotubes), metal oxides, activated carbon, polymer composites, etc.

Separator: A separator in a supercapacitor acts as an insulator between two electrodes. It should be diffusive to ions and prevent the recombination of opposite charges. The thickness of the separator should be less to achieve a high performance supercapacitor. It should be porous to maintain lower equivalent series resistance (ESR) and capable of diffusing ions, mechanically strong and chemically inert. The non-woven polypropylene (PP) membrane is the most commonly used separator.

Electrolyte: The performance of a supercapacitor is dependent on the electrolyte used. Every parameter of a supercapacitor such as, total resistance of the device, energy density, power density, life time and operating voltage of supercapacitor depend on the electrolyte used.

There are two types of electrolytes namely, aqueous electrolyte and solid (gel) electrolyte. Aqueous electrolytes are made up of inorganic salts dissolved in deionized water. The ionic conductivity of an aqueous electrolyte depends on the concentration, pressure, temperature and pH of the solution. The most common salts used for aqueous electrolytes are metal hydroxides (KOH, NaOH, etc.), sulphuric acid and lithium salts (LiOH, Li_2SO_4 and Li_2PO_4). However, aqueous electrolytes have few limitations such as, maximum operating voltage is limited to 1.23 V because of electrolysis of water, encapsulation should be proper to prevent the evaporation of water, which affects the cyclic ability of the device. Also, the separator should be a filter paper to hold the electrolyte, which increases the total thickness of the supercapacitor.

A gel electrolyte is a solution of inorganic salt in a gel solvent, such as, water soluble polymer. The gel electrolyte can be used to overcome the disadvantages of aqueous electrolytes. They can operate at the maximum voltage of 3 V.

Few advantages of supercapacitor are,

- The specific capacitance of supercapacitor is very large compared to conventional capacitors, it is a few hundred or thousand Fg^{-1}.
- They have longer life than regular energy storage devices.
- They have high charging rate, which requires very less time to charge the device.
- The transient response of supercapacitor is faster.

Besides their advantages over other energy devices, supercapacitors have few disadvantages.

- The self-discharge rate of supercapacitor is high.
- They can only be used as DC power supply

- Energy density of supercapacitor is lesser than that of lithium ion batteries.
- The main disadvantage of supercapacitor is sparking hazard because of high discharge rate and low internal resistance.

Cyclic voltammetry and Galvanostatic charge-discharge methods were used to study the supercapacitor electrodes. The specific capacitance from CV can be estimated using the formula,

$$C_s = \frac{Area\ under\ the\ CV}{potentail\ window \times Scan\ rate \times mass\ of\ the\ active\ material} \quad (Fg^{-1}) \ldots\ldots\ldots\ldots (26)$$

2.3.1.1 Preparation of electrode for supercapacitor testing

The working electrode of the supercapacitor was fabricated using a slurry prepared by thoroughly mixing the active material super P acetylene carbon black and polyvinylidene fluoride (PVDF) in the weight ratio of 7:2:1 with a few drops of N-methyl-2-pyrrolidone (NMP), which was brush coated on a pre-cleaned titanium foil (*Alfa Aesar*, 0.25 mm thickness and dimension 5×1 cm) and dried in a vacuum oven for 15 h at 60 ˚C. The average mass of the active materials coated on the foil was 0.35 mg. A schematic diagram of preparation of working electrode is shown in Figure 2.17.

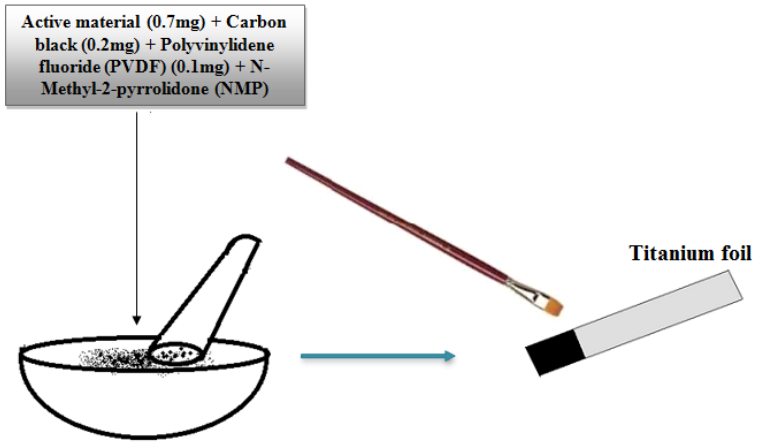

Figure 2.17 Schematic diagram of preparation of electrodes of supercapacitors.

2.3.2 Electrochemical sensors

Sensor is an electrical device that can detect an analyte that comes in contact with it. There are different kinds of chemical sensors based on their working mechanisms such as electrical sensors and electrochemical sensors.

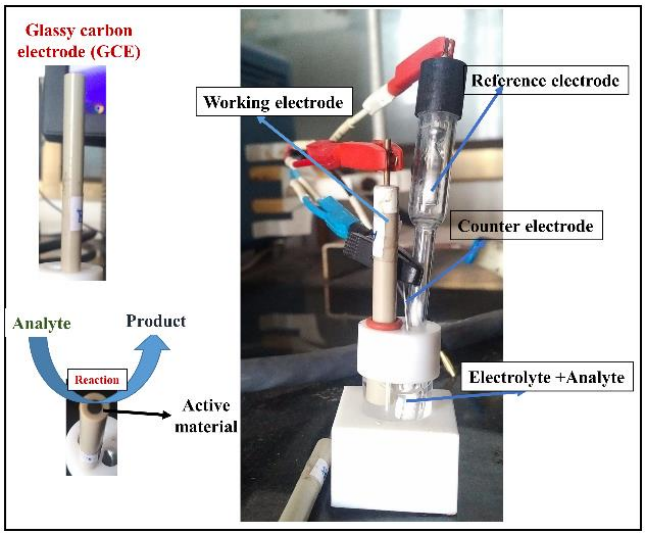

Figure 2.18 Photograph of electrochemical sensor setup and Glassy carbon electrode (GCE).

An electrochemical sensor is an electrochemical cell working on the principles of electrochemistry. It contains two or three electrodes in contact with an electrolyte. When the chemical species to be detected comes in contact with the working electrode, either oxidation or reduction takes place in the electrode material. An electrochemical sensor setup is shown in Figure 2.18. This can be recorded by electrochemical processes like cyclic voltammetry, electrochemical impedance spectroscopy, chronoamperometry or chronopotentiometry. This is the easiest and eco-friendly method of sensing electroactive chemical species. Ferrites can be used as electrochemical sensors because of their reactive properties with the chemical species.

Depending on the electrochemical techniques used to detect the chemical species, electrochemical sensors are categorized into, voltammetric (potentiometric) sensors and amperometric (colorimetric) sensors. The mode of operation of an electrochemical sensor can be selected according to the requirement, to enhance its

sensitivity and selectivity. In an amperometric sensor, the analyte will be studied at a constant applied potential and the current of the working electrode will be measured against time. While, in a potentiometric sensor, analyte will be studied at a constant applied current by measuring the potential of the working electrode against time. Both voltammetry and amperometric sensors can be used analyze the electroactive species qualitatively and quantitatively.

Parameters that can be estimated using electrochemical sensors are, specific sensitivity of the sensor, dynamic linear range and limit of detection (LOD) and limit of quantification (LOQ). The specific sensitivity of the sensors can estimated using the slope of the linear fit of current vs concentration of analyte in chronoamperometry and potential vs concentration of analyte in chronopotentiometry, the specific sensitivity can be written as,

$$Specific\ sensitivity = \frac{Slope\ of\ the\ calibration\ curve\ (AM^{-1})}{mass\ of\ the\ active\ material\ (g)} \ldots\ldots\ldots\ldots (27)$$

To estimate the LOD of a sensor, chronoamperometry/chronopotentiometry is run for 5 min without the addition of analyte. Then the standard deviation of current/potential at a particular time was calculated using the formula,

$$\sigma_{sd} = \sqrt{\frac{\sum(x_i - x_{mean})^2}{n}} \ldots\ldots\ldots\ldots (28)$$

and then, divide the standard deviation from the sensitivity of the sensor. Multiply the resulting value with 3 to get LOD with a signal to noise ratio of 3 (S/N=3) and multiply by 10 to get lowest limit of quantification with S/N=10.

2.3.2.1 Preparation of modified glassy carbon electrode for electrochemical sensors

In a typical procedure, a glassy carbon electrode (GCE) was cleaned by polishing its surface with alumina (0.05 μm) followed by electro-polishing in 0.5 M H_2SO_4 and sonicating in distilled water and ethanol for 5 s each. A homogeneous slurry was prepared by sonicating 1 mg of sample in 1 ml of NMP for 1 h, after which 4 μl of

slurry was drop casted using a micro pipette on the polished GCE surface (3 mm diameter). The modified GCE was dried and used as the working electrode for sensing tests. A schematic diagram of preparation of modified GCE is shown in Figure 2.19.

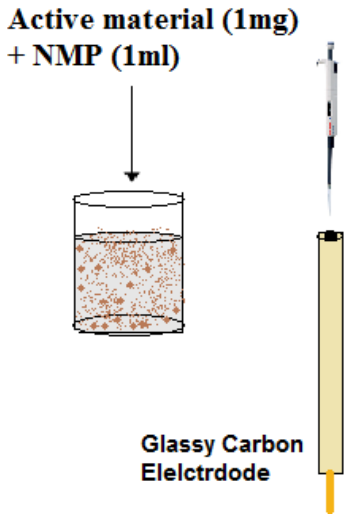

Figure 2.19 Schematic diagram of preparation of modified GCE.

In the present work, ferrite nanoparticle and composites based non-enzymatic hydrogen peroxide and dopamine sensors were studied.

2.3.3 Lithium ion batteries (LIB)

Lithium ion battery (LIB) is a rechargeable energy storage device. It is an electrochemical cell consisting of two electrodes and an electrolyte, which converts chemical energy to electrical energy. There are few advantages of LIB over other electrochemical energy source, LIB are rechargeable, they have long shelf-life, high cyclic stability, high capacity, rapid charge capability, high coulombic and energy efficiency, high energy density, broad range of operation temperature, etc. Although LIB have many advantages, they have few disadvantages too. Its moderate initial cost is its main disadvantage. Then, it can't be used in high temperature applications, capacity loss and thermal runaway on over charging are another disadvantages of LIB.

2.3.3.1 Construction and working of LIB

A schematic of a LIB is shown in the Figure 2.20. The main components of a LIB, are an anode, a cathode, and an electrolyte. On charging, Li-ions from the cathode transfer through the electrolyte and collect on the anode, which is known as Li-intercalation reaction. On discharging, the collected Li-ions on the anode transfer back to the cathode.

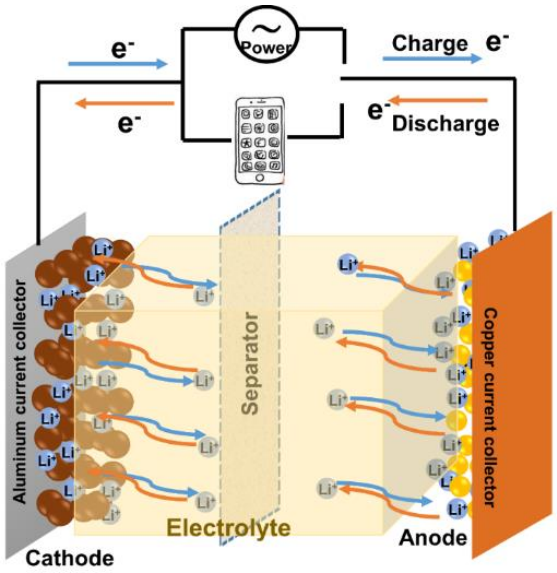

Figure 2.20 Schematic diagram of working of LIB.

Important parameters that evaluate the quality of a LIB are,

- Cell voltage, which is the open circuit voltage when no external current flows and it is defined as,

$$V_{oc} = \frac{\mu_{Li}^{N} - \mu_{Li}^{P}}{F} \ldots\ldots\ldots\ldots (29)$$

  where, μ_{Li}^{N} and μ_{Li}^{P} are chemical potentials of negative and positive electrodes respectively and F is the Faraday constant. A good LIB should have a high cell voltage.
- Electrode material should be conductive to electron and lithium ions to get a better performance. The electrode materials will be mixed with carbon black to improve their conductivity.

- Coulombic efficiency is the ratio of number of charges involve in the reaction during the charging process to that of discharging process. A good electrode should maintain a coulombic efficiency of more than 95%.
- An electrode material should have high specific capacity, which is written as,

$$Specific\ capacity = \frac{F \times \Delta X}{MW}\ Ahg^{-1} \ldots\ldots\ldots\ldots (30)$$

  Where, F is the Faraday constant, ΔX is the amount of reversible lithium and MW is the molecular weight of the active material.
- A good LIB should have high capacity-retention over a large number of cycles.
- It should have high energy and power density. The energy and power density of a LIB is defined as,

$$Energy\ density = Specific\ capacity \times cell\ voltage \ldots\ldots\ldots\ldots (31)$$

  and

$$Power\ denmsity = \frac{Energy\ density}{time} \ldots\ldots\ldots\ldots (32)$$

Components of a LIB should be selected according the above properties to get a high performance battery.

Electrodes: Electrodes play a main role in the overall performance of a LIB. Therefore, the selection of both anode and cathode materials are very important in constructing a high performance LIB. The electrodes are meant to accommodate the lithium ions in the structure while charging and discharging. Commonly, spinel structured lithium compounds are used as cathode material in commercially available batteries, because of their high capacity and cyclic ability. Graphite is used as anode material in commercially available LIB. But, there is requirement of good anode material to increase the performance with following qualities. An anode material should have high theoretical capacity, high structural stability and insolubility in electrolyte, good electrical conductivity and high mechanical stability. On charge-discharge cycles, Li-ions intercalate into the anode and it may cause increase in the volume and structural deformation of the anode. To avoid this, porous and nanomaterial are preferable as anode material of a LIB.

Separator: The separator is an essential component used to prevent physical contact between two electrodes. The electrolyte is absorbed into the separator pores and serves as the transport media for the ions. Even though separator doesn't involve in the reaction directly, it is an essential component, which influences the cell performance like safety and power density. A separator should have mechanical strength, be porous for ionic conductivity, and thermal and chemical stability. The microporous polyolefine membrane is the most used separator in standard Li-ion batteries.

Electrolyte: Lithium salts like, LiF_6PO_4 dissolved in organic solvents (ethylene carbonate and dimethyle carbonate) are generally used as LIB electrolyte. A good electrolyte is stable over the operating potential window, chemically compatible with electrodes, thermally stable and should not allow charge accumulation or polarization.

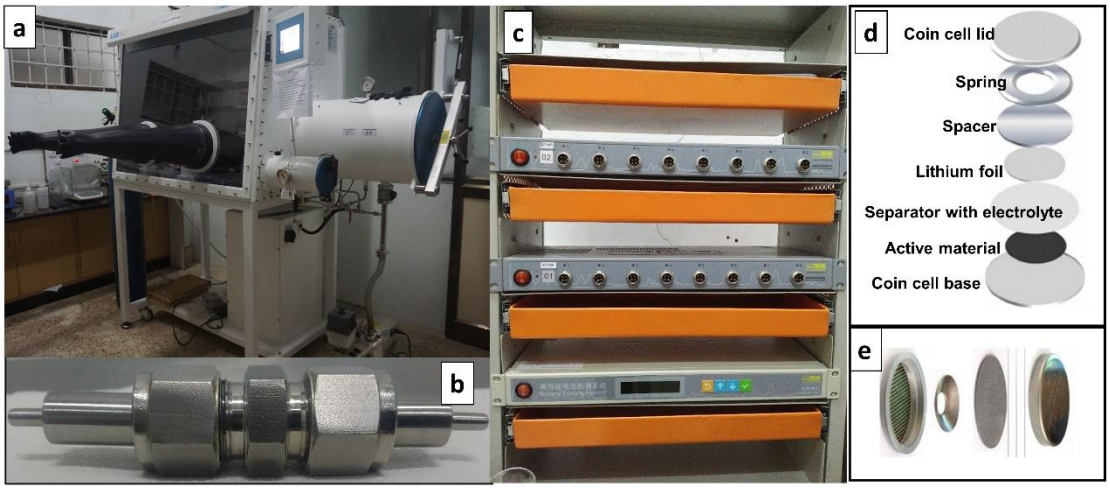

Figure 2.21 Photographs of (a) glovebox, (b) Swagelok cell and (c) Neware battery analyser and (d) half-cell assembly of a coin cell and (e) photo of a coin cell.

The lab setup for the LIB assembly and testing are given in Figure 2.21. A Swagelok half-cell was assembled in MBruan glove box and tested using Neware battery tester. The order of half-cell assembly of a coin cell is shown in Figure 2.21(d).

2.3.3.2 Preparation of anode for LIB

Anode was prepared by coating a mixture of 7:2:1 ratio of active material ($SnFe_2O_4$@rGO-MWCNT), super-p carbon black and PVDF with 50 µl of NMP on an

aluminium foil using doctor blade method. Then the coated foil was dried in a vacuum oven at 60 °C and cut into electrodes of 8 mm dia and pressed using hydraulic press. Then, the half-cell was assembled using a Swagelock cell (Fig 2.21(b)), inside the glove box (Fig 2.21(a)), in argon atmosphere. The prepared electrode and lithium metal were used as anode and cathode respectively. 1 M solution of lithium hexafluro phosphate ($LiPF_6$) in ethylene carbonate and dimethyl carbonate (1: 1) was used as the electrolyte. The battery performance was tested using Neware battery analyser (Fig 2.21(c)).

CHAPTER 3

Dielectric And Magnetic Properties of Nickel and Tin Doped Nano-ferrites Prepared using Microwave Assisted Method

This chapter includes the preparation of nickel doped ferrites ($Ni_xFe_{y-x}O_z$) and tin doped ferrites (α-$Sn_xFe_{2-x}O_3$) using microwave assisted method. The first part of the chapter discusses the effect of doping concentration of nickel and annealing temperature on the dielectric and properties of ferrites. The second part of the chapter discusses the effect of concentration of tin on the dielectric and magnetic properties of ferrites.

3.1 Dielectric and magnetic properties of Ni doped ferrites ($Ni_xFe_{y-x}O_z$-450 and α-$Ni_xFe_{2-x}O_3$-600)

In this section of the chapter, we discuss the preparation, dielectric and magnetic study of Ni-doped ferrites. The flow chart of the preparation and study of $Ni_xFe_{y-x}O_z$ is shown below,

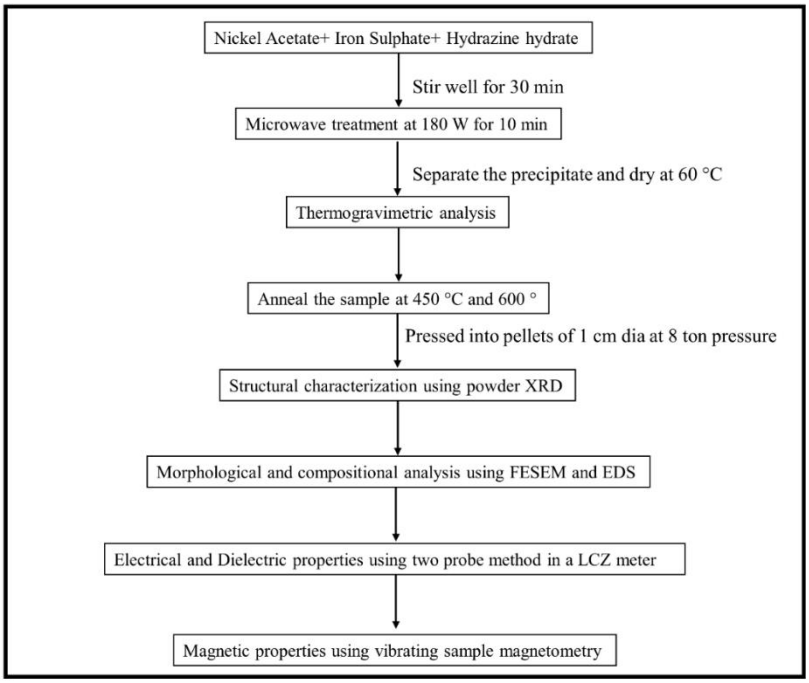

3.1.1 Preparation of Nickel doped Iron oxide nanoparticles using microwave assisted synthesis

Nickel doped iron oxide nanoparticles were prepared using microwave assisted method. Different mol% (0%, 1%, 2%, 3%, 4%, and 5%) of nickel acetate dihydrate solution was added to an aqueous solution of 50 mM iron sulphate heptahydrate. 2 ml of 10 mM hydrazine hydrate was added to the above solution and stirred well for 30 min. The reaction mixture was microwave treated at 180 W for 10 min. The precipitate formed was separated by centrifugation and washed thoroughly with ethanol, water and acetone. Then, the samples were dried at 60 °C in a hot air oven over-night and annealed at 450 and 600 °C for 10 hours.

3.1.2 Thermogravimetric analysis (TGA)

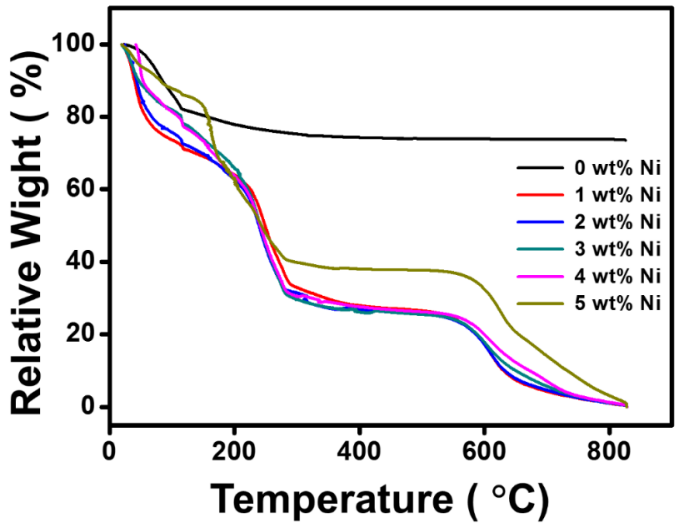

Figure 3.1 Thermogravimetric curves of Ni doped iron oxide nanoparticle.

TGA of the prepared samples is presented in Figure 3.1. The weight loss in samples till 200 °C can be attributed to the loss of absorbed and adsorbed water molecules. The sudden loss of weight above 270 °C in the undoped iron oxide sample indicates the phase transformation from iron hydroxide to hematite. Above 300 °C, there is no significant loss in the weight, indicating the completion of the formation of hematite phase (S. S. Pati et al. 2012, Topal et al. 2016). In the case of Ni doped iron

oxide samples, the weight loss till 200 °C is due to the loss of water molecules. On nickel doping, iron oxide forms inverse spinel phase at around 270 °C and it remains stable till 550 °C (Fig 3.1). The weight loss above 550 °C can be attributed to the transformation of spinel phase to rhombohedral phase (K et al. 2016).This study shows that there exists two phase transformations in iron oxide on nickel doping, namely from β-FeOOH to Fe_3O_4 at around 270 °C and Fe_3O_4 to α-Fe_2O_3 at around 550 °C. In 1%, 2%, 3% Ni doped samples the phase transformation from magnetite to hematite is almost complete at around 630 °C, while in 4 and 5% Ni doped samples the weight loss continues till 800 °C, which indicates the probability of formation of mixed phases or an intermediate phases.

3.1.3 X-ray diffraction (XRD)

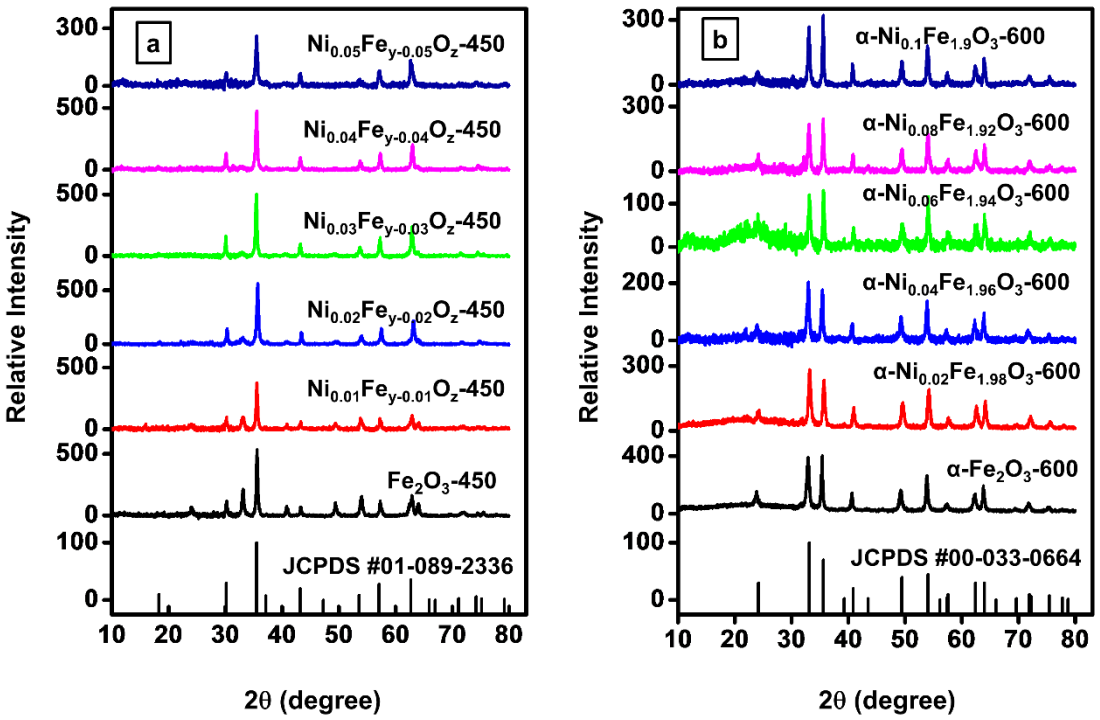

Fig 3.2 XRD patterns of (a) $Ni_xFe_{y-x}O_z$ -450 and (b) α-$Ni_xFe_{2-x}O_3$-600.

The XRD of all samples was done in the 2θ range from 10° to 80° with a scan rate of 2°/min. The XRD patterns of the samples were analysed and indexed available JCPDS data with the XpertHighscore plus software.

XRD patterns of nickel doped samples annealed at 450 °C are shown in Fig 3.2(a). The undoped samples (x=0) has a mixed phases of hematite (α-Fe_2O_3) and magnetite (Fe_3O_4). The peaks of the samples annealed at 450 °C match with JCPDS # 00-033-0664 (hematite) and #01-089-2336 (magnetite). On nickel doping, the peaks corresponding to the hematite phase decreases as shown in the Figure 3.2(a), which indicates the formation of magnetite phase on substitution of nickel ions. The hematite completely disappears in the 4% and 5% nickel doped samples by forming magnetite phase. The XRD patterns of 4 and 5% nickel doped samples of 450 °C annealed samples match to the JCPDS #01-089-2336. The XRD patterns of nickel doped samples annealed at 600 °C are shown in Fig 3.2(b). All samples match to hematite phase (JCPDS #00-033-0664) and on nickel doping the intensity of peaks decreases. A shift in the high intensity peaks near 33° and 35° indicates the substitution of Ni ions into the lattice sites of the Fe ions.

Table3.1 Structure parameters of $Ni_xFe_{y-x}O_z$ -450 from XRD.

Sample	Crystal structure	a (Å)	c (Å)	c/a	Crystallite size (nm)	Dislocation density × 10^{14} (m^{-2})
$Ni_{0.0}Fe_yO_z$-450	Rhombohedral	5.04668	13.7635	2.7272	38.57	6.7
$Ni_{0.01}Fe_{y-0.01}O_z$ -450	Rhombohedral	5.0497	13.7412	2.7212	106	0.88
$Ni_{0.02}Fe_{y-0.02}O_z$ -450	Rhombohedral	5.02828	13.8065	2.7458	30.32	10.87
$Ni_{0.03}Fe_{y-0.03}O_z$ -450	FCC	8.3851	8.3851	-	35.35	8.00
$Ni_{0.04}Fe_{y-0.04}O_z$ -450	FCC	8.3677	8.3677	-	84.86	1.38
$Ni_{0.05}Fe_{y-0.05}O_z$ -450	FCC	8.3895	8.3895	-	35.35	8.00

Table3.2 Structure parameters of $Ni_xFe_{2-x}O_3$ -600 from XRD.

Sample	A (Å)	C (Å)	c/a	Crystallite size (nm)	Dislocation density × 10^{14} (m^{-2})
α-Fe_2O_3-600	5.06554	14.07	2.7776	47.12	4.50
α-$Ni_{0.01}Fe_{1.99}O_3$-600	5.02722	13.7976	2.7446	21.08	22.5
α-$Ni_{0.02}Fe_{1.98}O_3$-600	5.05802	14.018	2.7714	26.34	14.41
α-$Ni_{0.03}Fe_{1.97}O_3$-600	5.03862	13.8876	2.7562	23.57	18.00
α-$Ni_{0.04}Fe_{1.96}O_3$-600	5.04968	13.7169	2.7164	26.52	14.22
α-$Ni_{0.05}Fe_{1.95}O_3$-600	5.05716	13.6898	2.7010	70.7	2.00

3.1.4 Scanning electron microscopy (SEM) and Energy Dispersive X-ray Spectrum (EDS)

SEM images and EDS spectra of $Ni_xFe_{y-x}O_z$ -450 are given in Figure 3.3. The undoped sample shows agglomerated nanorods like morphology. Nickel doped samples have agglomerated irregular shaped nanoparticles. The irregularity in the shape and size of the particles in the microwave assisted method is due to the formation of hot spots in the reaction mixture, unlike in the conventional heating methods where the reaction mixture heats up homogeneously. Typically in microwave assisted synthesis process, the heat production occurs within the sample, owing to which the optimal temperature required for nucleation and growth reaches very quickly (within 30 s) (Milosevic et al. 2011, Mingos 1993). Herein, for Fe_2O_3 formation the Fe^{3+} ions vigorously react with OH^- ions (due to high pH 13) under microwave irradiation – initially they nucleate to iron hydroxide (FeOOH) particles, which grow further through Ostwald ripening through dissolution-recrystallization process to yield iron oxide in the form of nanorods (Zhang et al. 2008). Similarly, the growth of nickel doped ferrite happens through the same mechanism, wherein Fe^{3+} and Ni^{2+} ions react together with OH^- ions under microwave irradiation, which nucleate to their corresponding hydroxides first and later dissolve and recrystallize as their corresponding oxides. EDS mapping of the samples show the uniform distribution of Ni throughout the sample.

SEM images and EDS spectra of α-Ni_x $Fe_{2-x}O_3$ -600 are given in Figure 3.4. From SEM images we can observe that all samples have agglomerated nanoparticles of iron oxides. On nickel doping the particle size has reduced. The EDS confirms the absence of any impurity in the samples. Nickel elemental mapping shows the equal distribution of Ni throughout the samples. Like in the samples annealed at 400 °C, the irregular shape and size of the particles are because of the microwave assisted synthesis (Sidhu et al. 1980). Unindexed peaks in EDS belong to Au and Pd, which are deposited on the sample to reduce the charge accumulation during SEM.

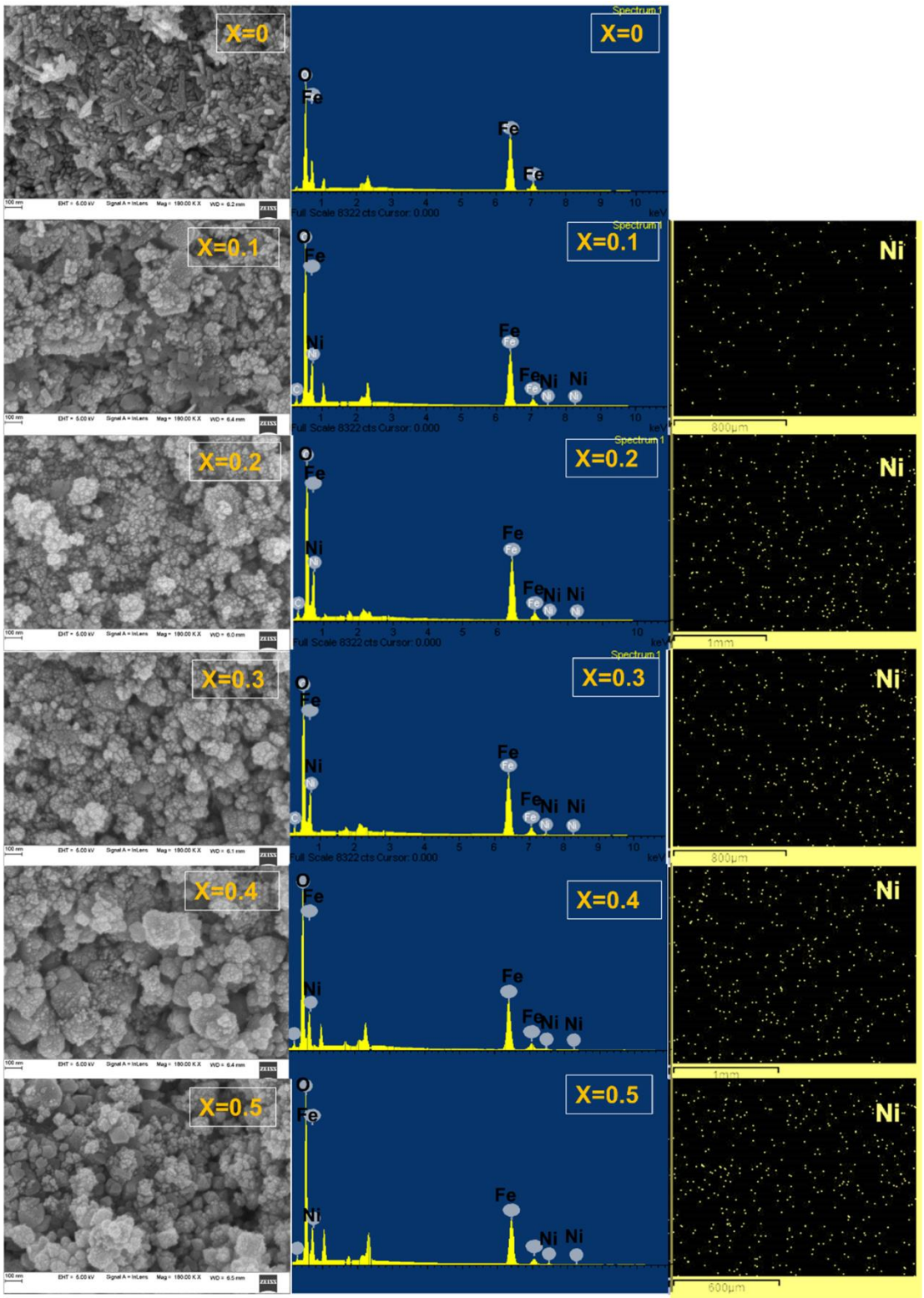

Fig 3.3 SEM images and EDS of $Ni_xFe_{y-x}O_z$-450 samples.

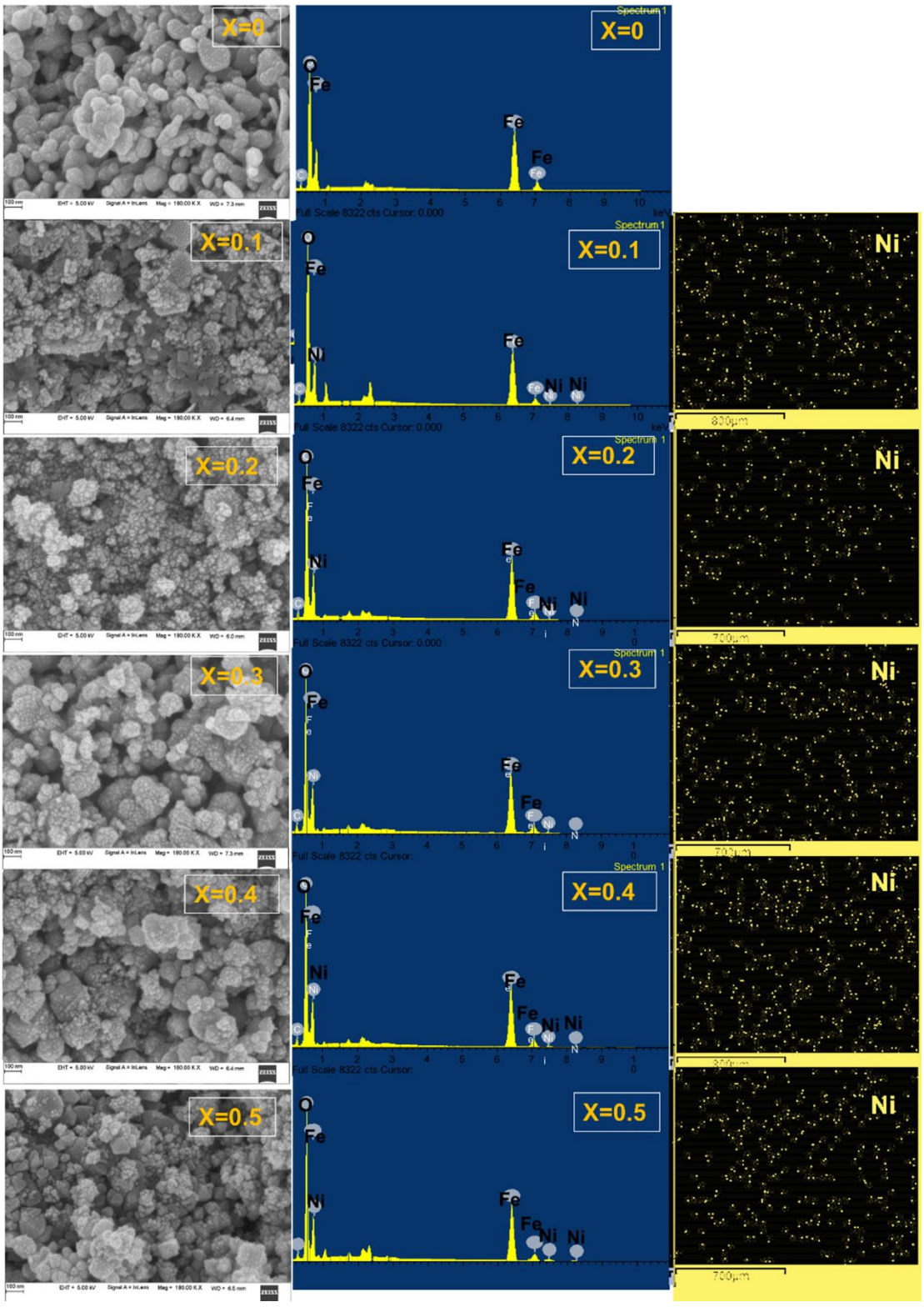

Figure 3.4 SEM images and EDS of α-$Ni_xFe_{2-x}O_3$-600 samples.

3.1.5 AC conductivity

The AC conductivity of $Ni_xFe_{y-x}O_z$ nanoparticles were recorded in the frequency ranges of 4 Hz to 8 MHz. Figure 3.5 shows the variation of AC conductivity of $Ni_xFe_{y-x}O_z$-450, and α-Ni_xFe_2-xO_3-600 with respect to frequency. AC conductivity of the samples increases with increase in frequency. This is a normal behaviour of AC conductivity of iron oxide, which can be explained using Maxwell-Wagner bilayer model with Koop's phenomenological theory (Umapathy et al. 2016, Jotania et al. 2016, Sridhar et al. 2016, Jayant Kolte1 2015, Fawzi et al. 2010, Babu, Kumar, et al. 2018). As explained in the **section 2.2.2.2**, iron oxides are made up of two layers, in which one is highly ordered grains and another is disordered grain boundaries. High conductive grains and resistive grain boundaries contribute to the AC conductivity at different frequency ranges (Mousavi Ghahfarokhi et al. 2016, Pavithradevi et al. 2017, Sonia et al. 2018, Vijatović Petrović et al. 2018, Bindu et al. 2018, Puri et al. 2018). At lower frequencies, conduction is more influenced by grain boundaries, whereas, grains contribute to the conduction at high frequencies. Also, at lower frequencies, the electron hopping between ferric and ferrous ions is slow, as frequencies increase the grains facilitate the hopping, thereby increase in the AC conductivity. Fig 3.6 shows the AC conductivity as a function of angular frequency ($\omega=2\pi f$). The plot of log σ_{ac} of $Ni_xFe_{y-x}O_z$-450, and α-$Ni_xFe_{2-x}O_3$-600 nanoparticles against log (ω^2) are linear. The conduction in iron oxides is due the electron exchange or polaron hopping mechanism between the same cations having different valence states. The doping of iron oxides with different cations affects the conduction depending on its site of occupation.

In the case of $Ni_xFe_{y-x}O_z$-450, AC conductivity decreases with increase in Ni concentration till x=0.02 and then increases with further increase in the nickel concentration. The undoped iron oxide annealed at 450 °C has hematite structure, which is highly resistive material. On nickel doping there is a formation of mixed phase of hematite and magnetite. In hematite structure the inclusion of impurity ions like Ni collect at the surface of the material during phase transformation from magnetite to hematite, while in magnetite structure Ni substitutes to the Fe^{2+} ions at octahedral sites (Sidhu et al. 1978). The formation of mixed phase is the reason for the lower AC

conductivity of samples of composition x=0.01 and 0.02. Above x=0.03, a pure phase of magnetite forms, and AC conductivity increases for x=0.4 and x=0.05 because of pure magnetite phase. In the case of α-Ni_xFe_2-xO_3-600, there is a random variation in the AC conductivity on nickel doping. Nickel doped iron oxides crystallizes to pure hematite phase on annealing at 600 °C, which has lower conductivity than magnetite phase. This leads to the lower values of AC conductivity of α-$Ni_xFe_{2-x}O_3$-600 than that of $Ni_xFe_{y-x}O_z$-450.

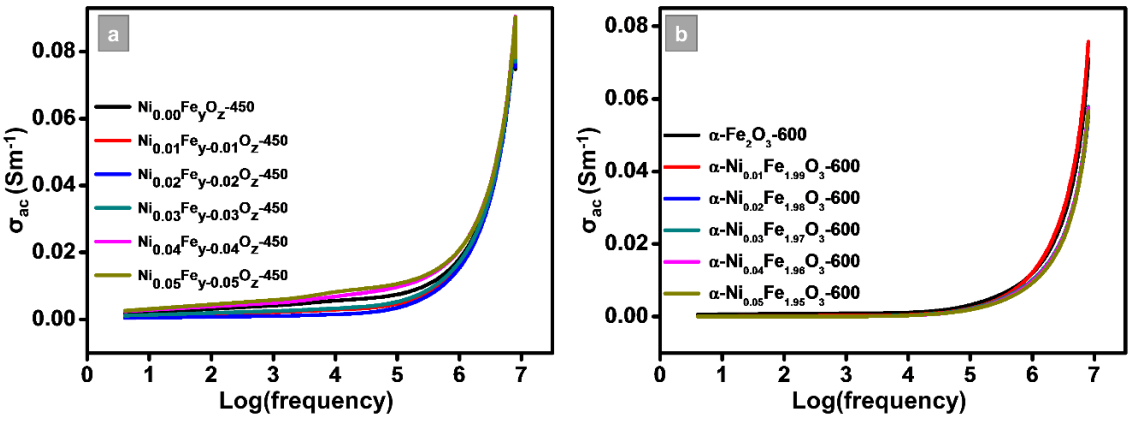

Figure 3.5 AC conductivity (σ_{ac}) of (a) $Ni_xFe_{y-x}O_z$-450 and (b) α-$Ni_xFe_{2-x}O_3$-600 as a function of frequency.

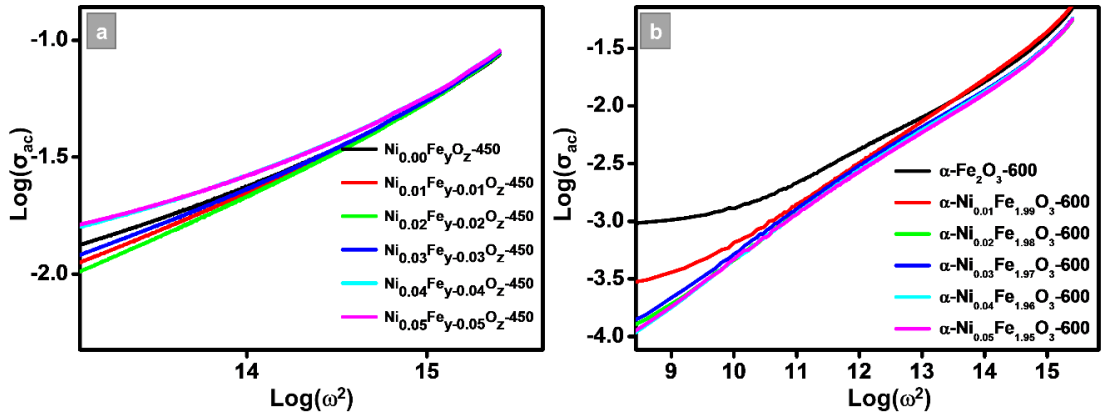

Figure 3.6 AC conductivity (σ_{ac}) of (a) $Ni_xFe_{y-x}O_z$-450 and (b) α$Ni_xFe_{2-x}O_3$-600 as a function of angular frequency (ω).

3.1.6 Dielectric properties

Dielectric properties of metal ferrites depend on dielectric polarization and localized charges. The dielectric constant of $Ni_xFe_{y-x}O_z$ nanoparticles were recorded in the frequency ranges of 4 Hz to 8 MHz.

Fig 3.7 shows the frequency-dependant dielectric constant of (a) $Ni_xFe_{y-x}O_z$-450, and (b) α-$Ni_xFe_{2-x}O_3$-600 nanoparticles. From the Figure 3.7, we can observe that dielectric constant has high values at lower frequencies and decreases with the increase in frequency, and then remains constant after a point. This typical behaviour of dielectric constant is due to the dielectric relaxation (Haque et al. 2017). This kind of behaviour can be qualitatively explained by the polarisation mechanism in ferrites, which is similar to that of the conduction process. According to Iwauchi (Kōō 1971), dielectric properties of ferrites and conduction mechanism have a strong correlation. The observed trend of real and imaginary dielectric constant of ferrites is mainly due to Maxwell-Wagner type of interfacial polarisation. This can be explained using Koop's phenomenological theory (Koops 1951). According to Koop's theory, ferrites are composed of two layers, namely, good conducting grains and highly resistive gain boundaries. Thus, the dielectric behaviour of ferrites can be attributed to the interfacial polarisation, which is due to their heterogeneous structure. The dielectric constant decreases with an increase in frequency because of the finite time required by charge carriers to line up in the direction of the applied electric field in the inhomogeneous dielectric structure. Under the influence of an applied electric field, electrons reach grain boundary region through hopping. The grain boundary resistance causes localised accumulation of charges, which in turn causes the interfacial polarisation. This leads to the high dielectric constant at low frequency. As the frequency increases, the polarisation decreases, in turn, the dielectric constant decreases. The dielectric constant at higher frequencies correspond to dipolar polarisation and is insensitive to heterogeneity of the material. However, in ferrites, the electrical polarization is due to the directional electric field produced by the electron exchange between ferrous (Fe^{2+}) and ferric (Fe^{3+}) ions. Beyond a certain frequency, electron hopping cannot follow the applied alternating electric field (Pervaiz et al. 2014, Ghodake et al. 2017, Agami 2018, Atif et al. 2018).

In $Ni_xFe_{y-x}O_z$-450 samples, the dielectric constant decreases with an increase in nickel concentration till the composition $Ni_{0.02}Fe_{y-0.02}O_z$-450 and further increases with nickel concentration. $Ni_xFe_{y-x}O_z$-450 (x=0, 0.01 and 0.02). $Ni_xFe_{y-x}O_z$-450 (x=0.04 and 0.05) samples forms pure magnetite structure, which have higher conductivity than that of samples $Ni_xFe_{y-x}O_z$-450 (x=0, 0.01 and 0.02). The formation of pure magnetite phase leads to the higher dielectric constant of ferrite samples doped with high concentration of nickel. In the case of $Ni_xFe_{2-x}O_3$-600, the dielectric constant decreases with increase in Ni concentration till x=0.05. Dielectric constants of $Ni_xFe_{y-x}O_z$-450 and $Ni_xFe_{y-x}O_z$-600 at 1 kHz are given in the table.2. The dielectric constant of $Ni_xFe_{y-x}O_z$-450 is more than that of $Ni_xFe_{y-x}O_z$-600, which can be attributed to the decrease in the conductivity due to the formation of hematite phase on annealing at 600 °C (Cornell et al. 2003).

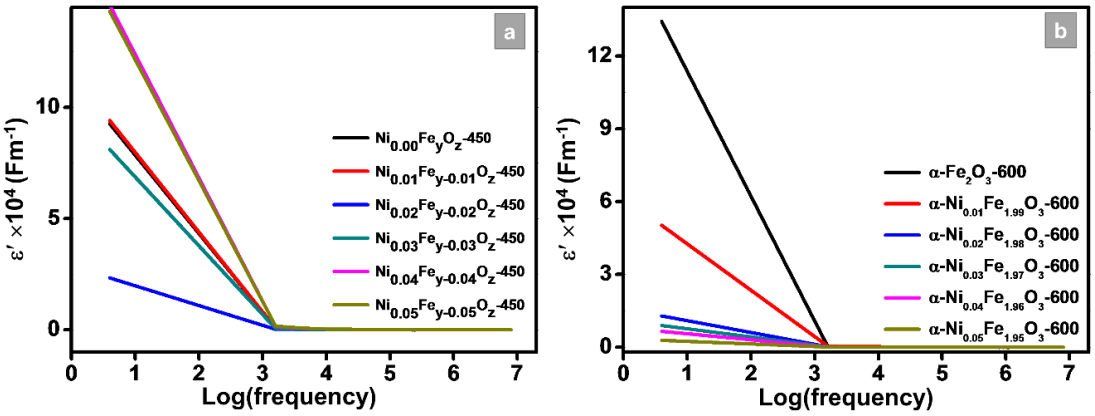

Figure 3.7 Frequency dependence of dielectric constant of (a) $Ni_xFe_{y-x}O_z$-450 and (b) $Ni_xFe_{2-x}O_3$-600.

3.1.7 Complex impedance

A resistance to the flow of AC electric field is known as Impedance (Z). The analysis of impedance spectra provides an information about the contributions of electrode, electrolyte, grain and grain boundaries to the resistance in flow of current through a dielectric medium (Farid et al. 2017). Figure 3.8 and Figure 3.9 show the real and imaginary parts of impedance of (a) $Ni_xFe_{y-x}O_z$-450 and (b) $Ni_xFe_{2-x}O_3$-600 as a function of frequency in logarithmic scale. Both real and imaginary impedance decreases with an increase in frequency in all cases. Which can be explained using Maxwell-Wagner bilayer model of ferrites like that of AC conductivity. While, the

impedance spectra also provides an extra information about the relaxation of the sample.

Relaxation peaks in the Z″(f) indicates the probability of charge hopping from one site to another. The resonance frequency is directly proportional to the hopping probability of Fe^{3+} ions in the octahedral sites. The variation in the hopping probability leads to the shift in the resonance frequency (Rezlescu et al. 1974).

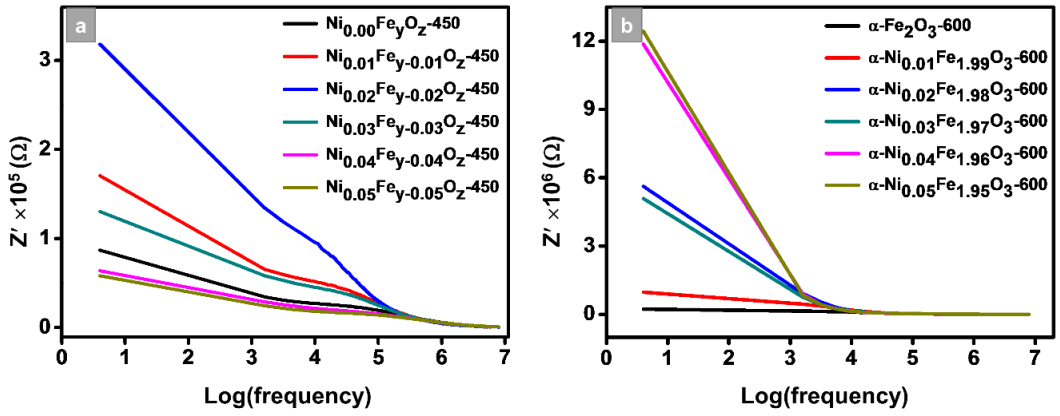

Figure 3.8 Real part of AC impedance (a) $Ni_xFe_{y-x}O_z$-450 and (b) $Ni_xFe_{2-x}O_3$-600 as a function of frequency.

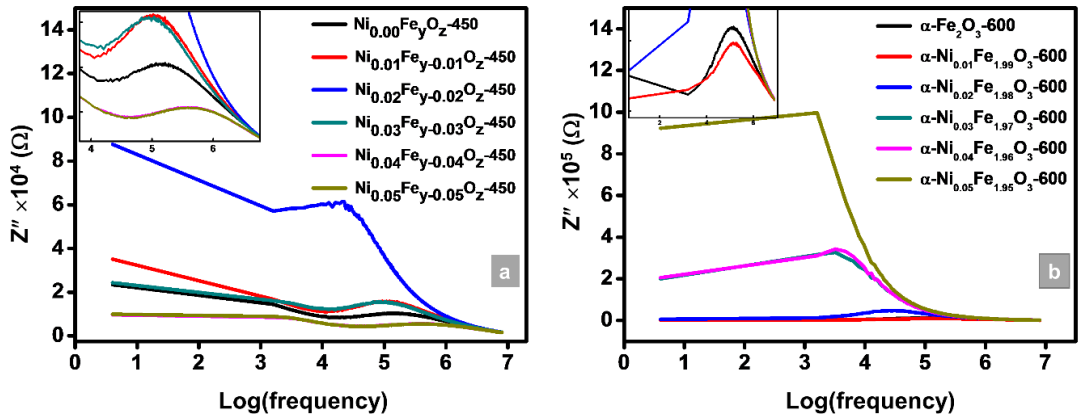

Figure 3.9 Imaginary part of AC impedance (a) $Ni_xFe_{y-x}O_z$-450 and (b) $Ni_xFe_{2-x}O_3$-600 as a function of frequency.

Fig 3.9(a) and Fig 3.9(b) show the variation of imaginary impedance of $Ni_xFe_{y-x}O_z$-450 and α-$Ni_xFe_{2-x}O_3$-600 respectively. The relaxation peaks in $Ni_xFe_{y-x}O_z$-450 shifts towards lower frequency side on increasing nickel doping till $Ni_{0.02}Fe_{y-0.02}O_z$-

450 composition and further shifts to higher frequency region for $Ni_xFe_{y-x}O_z$-450 (x=0.03, 0.04 and 0.05) compositions. This indicates an increase in the hopping probability of charge carriers in the samples with compositions $Ni_xFe_{y-x}O_z$-450 (x=0.03, 0.04, 0.05), which are in magnetite phase. In the case of α-$Ni_xFe_{2-x}O_3$-600, the peak shift towards lower frequency region with an increase in the concentration of Ni substitution. Which implies that the hopping probability of hematite phase reduces with the substation of Ni ions into the structure.

The contributions from grains and grain boundary regions can be separated using impedance study (Farid et al. 2017, Hankare et al. 2010). The low frequency region of the curve gives an information about the grain boundary contribution, and high frequency region tells about the bulk properties of the material arising from the grains. Generally, the impedance plot exhibits a semi-circularly shaped curve, which obeys Debye's expression for an ideal case (Nobre et al. 2003). In non-ideal situations, curve deviates from the Debye's expression and can be represented using Cole-Cole-empirical equation (Nobre et al. 2003, Batoo et al. 2009),

$$Z^* = \frac{R}{1 + (j\omega/\omega_o)^{1-n}} \quad \ldots\ldots\ldots\ldots (33)$$

The resistance R of the equivalent circuit is the diameter of the semicircle, and the capacitance is estimated using the frequency maximum of the semicircle (Hankare et al. 2010).

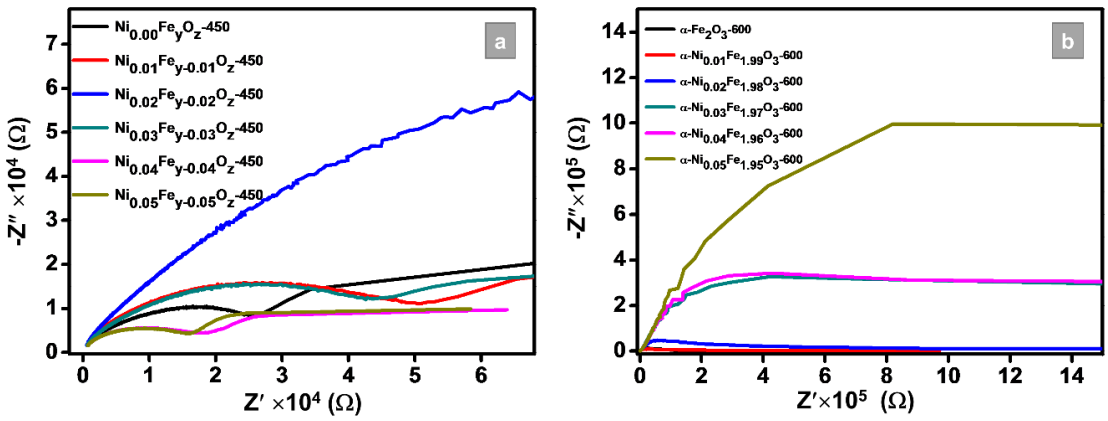

Figure 3.10 Nyquist plots of (a) $Ni_xFe_{y-x}O_z$-450 and (b) α-$Ni_xFe_{2-x}O_3$-600.

The Nyquist plot differentiates the contribution of grains and grain boundaries to the resistance. The non-ideal condition arises, when the contribution of grain boundary region to the impedance is more than that of grains and due to the inhomogeneous structure of the material (Batoo et al. 2009). Fig 3.10 shows Nyquist plots of $Ni_xFe_{y-x}O_z$-450 and α-$Ni_xFe_{2-x}O_3$-600 samples. The impedance spectra of a material can be analysed using idealized circuit model, in which each semicircle of Cole-Cole plot is equivalent to an RC parallel circuit with discrete electrical components. The resistance of grains (R_g) and grain boundaries (R_{gb}) can be estimated using the diameter of the semicircles. While, the capacitance of grains (C_g) and grain boundaries (C_{gb}) can be estimated from the maximum frequency (f_{max}) of the semicircle using the relation $C=1/R\omega$, where ω is the maximum angular frequency of the semicircle.

Table.3.3 Resistance, capacitance and relaxation time of grains and grain boundaries of $Ni_xFe_{y-x}O_z$-450 and α-$Ni_xFe_{2-x}O_3$-600 from Cole-Cole plots.

	R_g (Ω)	C_g (pF)	f_{max} (Hz)	τ (μs)
$Ni_{0.00}Fe_yO_z$-450	10315	60.9	152030	1.046
$Ni_{0.01}Fe_{y-0.01}O_z$-450	15626	56.12	110430	1.441
$Ni_{0.02}Fe_{y-0.02}O_z$-450	61367	99.01	20808	7.648
$Ni_{0.03}Fe_{y-0.03}O_z$-450	15461	64.44	96023	1.657
$Ni_{0.04}Fe_{y-0.04}O_z$-450	5519	41.66	416090	3.826
$Ni_{0.05}Fe_{y-0.05}O_z$-450	5505	41.5	401680	3.962
	R_{gb} (Ω)	**C_{gb} (pF)**	**f_{max} (Hz)**	**τ (μs)**
α-Fe_2O_3-600	11865	56.3	131230	1.21
α-$Ni_{0.01}Fe_{1.99}O_3$-600	9593	55.8	171240	0.93
α-$Ni_{0.02}Fe_{1.98}O_3$-600	47540	89.9	32010	4.97
α-$Ni_{0.03}Fe_{1.97}O_3$-600	327332	117.8	3204	49.6
α-$Ni_{0.04}Fe_{1.96}O_3$-600	342444	116.0	3204	49.6
α-$Ni_{0.05}Fe_{1.95}O_3$-600	742	-	-	-

The $Ni_xFe_{y-x}O_z$-450 set of samples have one complete semi-circular arc, and a shoulder, which is the initiation of the second semicircle at the lower frequency range (fig 3.10a). The semicircle arc at the high frequency region is due to the contribution of grains to the impedance, and the contribution from grain boundaries is out of the applied frequency range for $Ni_xFe_{y-x}O_z$-450. Both grain resistance (R_g) and capacitance (C_g) (tabulated in the table 3.3) of $Ni_xFe_{y-x}O_z$-450 increase with increase in nickel doping till x=0.02, and it further decreases with an increase in the doping concentration, which can be attributed to the formation of magnetite phase above $Ni_{0.02}Fe_{y-0.02}O_z$-450. $Ni_{0.05}Fe_{y-0.05}O_z$-450 has the lowest values of R_g and C_g, which indicates the greater polarizability of the sample on Ni doping.

α-$Ni_xFe_{2-x}O_3$-600 samples have a single distorted semi-circular arc, which suggests that, the contribution of grain boundary region is predominant in these samples. Hence, the contribution from the grains cannot be resolved in the studied frequency range (Dar et al. 2010). The grain boundary resistance (R_{gb}) and capacitance (C_{gb}) (tabulated in table3.3) of α-$Ni_xFe_{2-x}O_3$-600 decreases with increase in nickel doping till α-$Ni_{0.01}Fe_{1.99}O_3$-600 and then increases with increase in the nickel concentration. Grain boundary effect is more in α-$Ni_xFe_{2-x}O_3$-600 than $Ni_xFe_{y-x}O_z$-450, which can be attributed to the reduced crystallite size and increased dislocation density on annealing at 600 °C.

3.1.8 Electrical modulus

Figure 3.11 shows the frequency-dependant real electric modulus (M′) of (a) $Ni_xFe_{y-x}O_z$-450, and (b) α-$Ni_xFe_{2-x}O_3$-600 nanoparticles. Real part of electric modulus for all of the samples increases with an increase in the frequency and have relaxation peaks. The relaxation peaks of electric modulus show the transition of hopping length of the charge carriers. The frequency region below the f_{max} of M′ is the conduction process due to hopping of charge carriers, which travel over long distances. The frequency region above f_{max} of M′ represents the charge carriers confined to a potential well and mobile over short distances (Assar et al. 2014). Figure 3.12 shows the imaginary electric modulus of (a) $Ni_xFe_{y-x}O_z$-450, and (b) α-$Ni_xFe_{2-x}O_3$-600 nanoparticles. From Figure 3.12 we can observe that, imaginary part of modulus also

increases with an increase in the frequency and has relaxation peaks. These are resonance peaks, where the frequency of the applied field matches the frequency of the oscillating dipoles (Farid et al. 2017, Koops 1951).

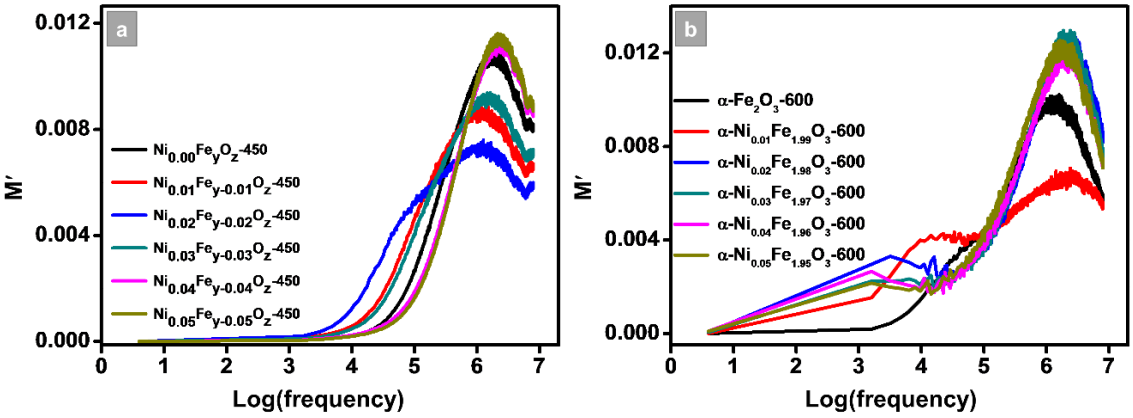

Figure 3.11 Frequency dependence of real part of the electrical modulus of (a) $Ni_xFe_{y-x}O_z$-450 and (b) α-$Ni_xFe_{2-x}O_3$-600.

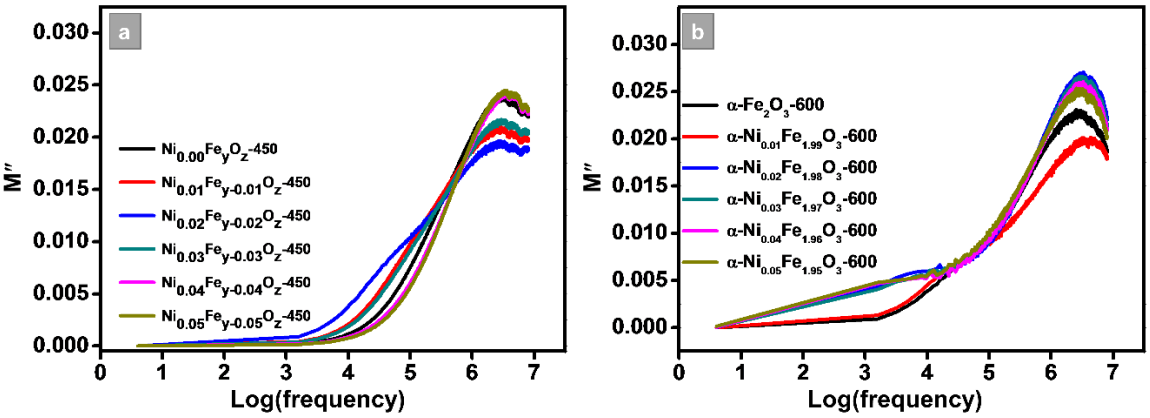

Figure 3.12 Frequency dependence of imaginary part of the electrical modulus of (a) $Ni_xFe_{y-x}O_z$-450 and (b) α-$Ni_xFe_{2-x}O_3$-600.

3.1.8 Dielectric loss factor (Dissipation factor)

Dissipation factor represents the loss of energy from the applied field in polarisation of the material and it depends on the stoichiometry, Fe^{2+} content in the iron oxide, and homogeneity of the structure. (Ghodake et al. 2017). The variation of dissipation factor of (a) $Ni_xFe_{y-x}O_z$-450, (b) α-$Ni_xFe_{2-x}O_3$-600 nanoparticles with frequency is shown in the Figure 3.13. Dissipation factor of all materials decreases with

increase in frequency and have relaxation peaks. The sudden decrease of loss factor at low-frequency ranges can be ascribed to the organized growth of domains and effect the diamagnetic dopant. The insignificant decrease of tan δ at high frequencies may be due to the probable mismatch of domain size with the frequency of the applied field (Sridhar et al. 2016). In iron oxides, the loss is controlled by many factors like Fe^{2+} and Fe^{3+} content, the stoichiometry of the samples, non-uniform and heterogeneous domain wall geometry and frustrated domain walls, domain defect, structural homogeneity and flux gradient, which sequentially depends on the composition, preparation method and the sintering temperature of the samples. According to Rezlesque model (N. et al. 1974), peaks corresponds to the resonance between the hopping frequency of Fe^{2+}/Fe^{3+} and the applied frequency.

For $Ni_xFe_{y-x}O_z$-450, the f_{max} shifts towards lower frequency side till $Ni_{0.02}Fe_{y-0.02}O_z$-450 composition and then it shifts towards the higher frequency region. This indicates that, the hopping probability of carriers in octahedral sites decreases till $Ni_{0.02}Fe_{y-0.02}O_z$-450 and increases further with an increase in the concentration of Ni. In the case of $Ni_xFe_{2-x}O_3$-600 samples, α-Fe_2O_3-600 do not have any relaxation peak. Whereas, α-$Ni_{0.01}Fe_{1.99}O_3$-600 to α-$Ni_{0.05}Fe_{1.95}O_3$-600 have relaxation peak at around 100 kHz, which indicates the high hopping probability of charge carriers in α-$Ni_xFe_{2-x}O_3$-600.

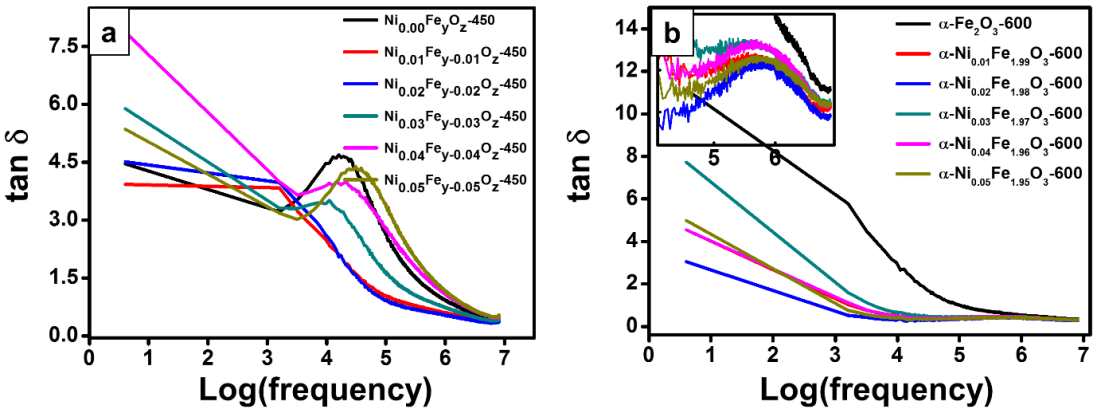

Figure 3.13. The dissipation factor of (a) $Ni_xFe_{y-x}O_z$-450, (b) α-$Ni_xFe_{2-x}O_3$-600 versus frequency.

Table.3.4 AC conductivity, loss factor and dielectric constant of $Ni_xFe_{y-x}O_z$-450 and $Ni_xFe_{2-x}O_3$-600 at 1 kHz.

Samples	AC conductivity (Sm^{-1})	Loss factor	Dielectric constant (Fm^{-1})
$Ni_xFe_{y-x}O_z$-450			
0	0.0749	2.62568	41.29678
0.01	0.00471	1.03002	39.65095
0.02	0.00352	0.90884	38.20486
0.03	0.00533	1.65945	41.15701
0.04	0.00974	2.75034	46.89175
0.05	0.01064	3.35064	46.99715
$Ni_xFe_{2-x}O_3$-600			
0	0.0032	0.99565	0.99565
0.02	0.0023	0.40065	0.40065
0.04	0.002	0.3408	0.3408
0.06	0.0216	0.4433	0.4433
0.08	0.00199	0.41605	0.41605
0.1	0.00191	0.38089	0.38089

3.1.10 VSM of $Ni_xFe_{y-x}O_z$-450 and $Ni_xFe_{2-x}O_3$-600

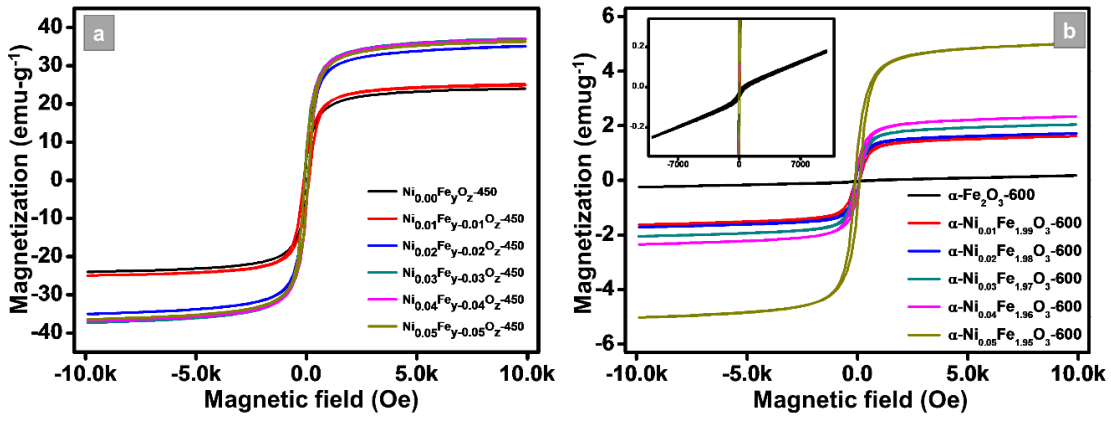

Figure 3.14 VSM M-H curves of (a) $Ni_xFe_{y-x}O_z$-450 and (b) α-$Ni_xFe_{2-x}O_3$-600.

Magnetization studies of $Ni_xFe_{y-x}O_z$-450 and α$Ni_xFe_{2-x}O_3$-600 were done in the applied magnetic field of range 0 to 10 kOe. Figure 3.14 shows the M-H curves of

$Ni_xFe_{y-x}O_z$-450 and α-$Ni_xFe_{2-x}O_3$-600 nanoparticles. $Ni_xFe_{y-x}O_z$-450 show ferrimagnetic behaviour. The saturation magnetization (M_s) increases with an increase in the nickel concentration till x=0.03 composition, and further decreases with increase in doping concentration. α-$Ni_xFe_{2-x}O_3$-600 samples show ferrimagnetic behaviour except x=0 composition. On nickel doping, samples annealed at 600 °C transform from antiferromagnetic to ferrimagnetic, which is because of the positive net magnetic moment in the basal planes of the hematite structure on nickel substitution. The saturation magnetization of α-$Ni_xFe_{2-x}O_3$-600 samples increases with an increase in nickel doping. M_s values of $Ni_xFe_{y-x}O_z$-450 samples is in the range of 23-37 $emug^{-1}$, which decreases to 1-5 $emug^{-1}$ in α-$Ni_xFe_{2-x}O_3$-600 samples. This is because of the magnetic phase transformation of samples from inverse spinel structured magnetite phase to rhombohedral structured hematite phase at high temperature (Lee et al. 2014).

The loop squareness ratio (M_r/M_s) is the measure of how square the hysteresis loop of a magnetic material is and also the magnetic anisotropy of the material (Ali et al. 2017, Joshi et al. 2017). Both $Ni_xFe_{y-x}O_z$-450 and α-$Ni_xFe_{2-x}O_3$-600 have loop-squareness value less than 0.2, which indicates the multi domain formation in the particles. Lower loop-squareness values of the samples can be attributed to the larger agglomerated particles and the formation of domain walls (Praveena et al. 2015). Coercivity is an extrinsic and microstructural property of a magnetic material. It depends on dislocations, defects, strain, porosity and magneto-crystalline anisotropy in the material. The preparation method has a strong impact on the coercivity of a material (Joshi et al. 2017). The Magneto-crystalline anisotropy constant (K) of $Ni_xFe_{y-x}O_z$-450 and α-$Ni_xFe_{2-x}O_3$-600 were calculated using the relation **(22)** (Moradmard et al. 2015).

We can observe a random variation in the coercivity of iron oxide nanoparticles on nickel doping, which is because of the random variation in the crystallite size, irregular shape and sizes of the prepared samples. The magneto-crystalline anisotropy of both $Ni_xFe_{y-x}O_z$-450 and α-$Ni_xFe_{2-x}O_3$-600 increases with the increase in Ni content. K of $Ni_xFe_{y-x}O_z$-450 is greater than that of α-$Ni_xFe_{2-x}O_3$-600, which can be attributed to the formation of pure hematite phase on annealing samples at 600 °C (Besser et al. 1967). The magnetic parameters of $Ni_xFe_{y-x}O_z$-450 and α-$Ni_xFe_{2-x}O_3$-600 are tabulated in table.3.5.

Table. 3.5. Magnetic parameters of $Ni_xFe_{y-x}O_z$-450 and α-$Ni_xFe_{2-x}O_3$-600 (x=0.00 to 0.05) at room temperature.

x	M_s (emu-g^{-1})	H_c (Oe)	M_r (emu-g^{-1})	M_r/M_s	K (ergs-cm^{-3})
$Ni_xFe_{y-x}O_z$-450					
0.00	23.73	64.97	5.82	0.245	1606
0.01	24.89	115.51	5.94	0.238	2995
0.02	34.90	84.16	7.34	0.210	3060
0.03	36.90	84.10	7.78	0.211	3233
0.04	36.90	85.37	7.31	0.198	3281
0.05	36.25	79.93	7.12	0.196	3018
α-$Ni_xFe_{2-x}O_3$-600					
0.00	-	131	0.03	-	-
0.01	1.63	105.89	0.34	0.209	180
0.02	1.72	83.33	0.36	0.209	149
0.03	2.04	99.03	0.46	0.226	210
0.04	2.34	92.16	0.51	0.217	225
0.05	5.01	99.03	1.09	0.217	517

3.2 Dielectric and magnetic properties of Sn doped ferrites (α-$Sn_xFe_{2-x}O_3$)

In this part of the chapter we have discussed the preparation, dielectric and magnetic study of Sn-doped ferrites. The flow chart of the preparation and study of α-$Sn_xFe_{2-x}O_3$ is shown below**,**

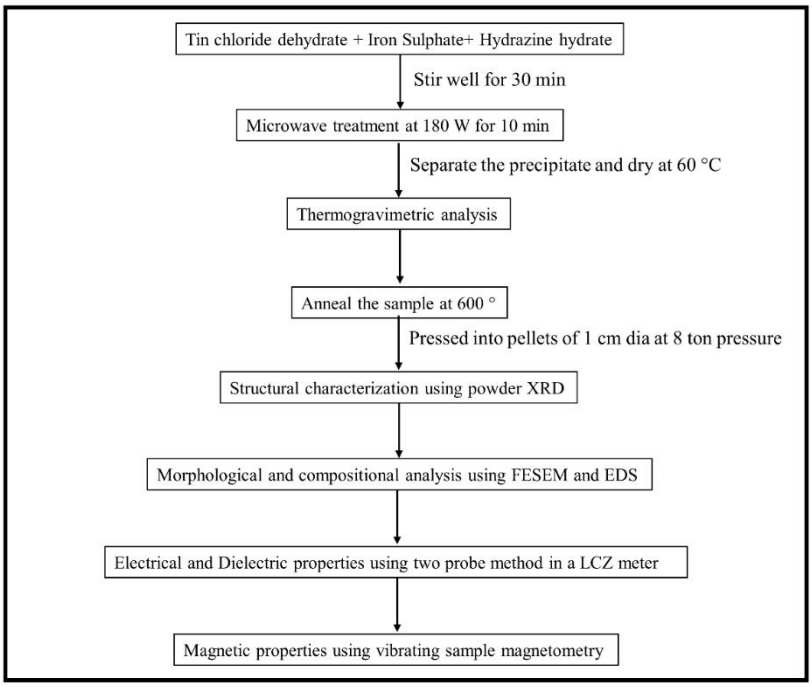

3.2.1 Preparation of Tin doped α-Fe_2O_3 (α-$Sn_xFe_{2-x}O_3$)

α-$Sn_xFe_{2-x}O_3$ nanoparticles were prepared by two step micro wave assisted synthesis. In a typical synthesis, a total 50mM aqueous solution of Iron sulphate hepta hydrate ($FeSO_4$ $7H_2O$) and different mol% (0%, 1%, 2%, 3%, 4%, 5% and 10%) of tin chloride dihydrate ($SnCl_2$ $2H_2O$) was taken. 50 mM of sodium hydroxide (NaOH) solution was added and stirred well for 15 min. Then, the homogeneous mixture was microwave treated for 10 min at 180 W. The precipitate formed in the treated mixture was separated by centrifugation and washed thoroughly with water and acetone. The washed samples were dried at 60 °C for 15 hours in a hot air oven and annealed at 600 °C for 10 hours in the air. For the study of electrical properties, the samples were made into pellets of 1 cm diameter and about 1 mm thickness by applying 8 tons pressure using a hydraulic press (Indfurr Chennai, India).

3.2.2 Thermogravimetric analysis (TGA)

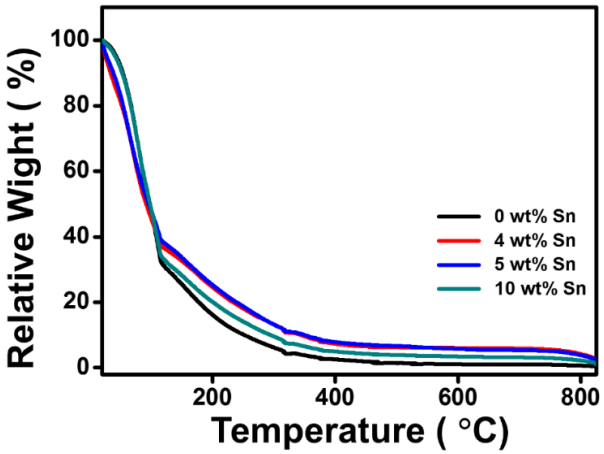

Figure 3.15 TGA curves of Sn doped ferrites.

Figure 3.15 shows TGA curves of as prepared α-$Sn_xFe_{2-x}O_4$ (x=0, 0.08, 0.1 and 0.2). TGA was carried out by heating as-prepared samples from room temperature to 800 °C in nitrogen atmosphere. The observed weight loss till 200 °C is due to the loss of adsorbed water molecules. Further decrease in the weight indicates the phase transformation from Fe(OOH) to α-Fe_2O_3 (hematite) in all samples (K et al. 2016). The weight loss is completed at about 370 °C, which indicates the completion of transformation(Wang et al. 2012).

3.2.3 X-ray diffraction (XRD)

Figure 3.16 shows the XRD of the pure hematite and Sn doped hematite with different concentrations. X-ray patterns show a single phase of hematite structure and peaks are indexed with JCPDS data #00-033-0664. α-$Sn_xFe_{2-x}O_3$ (x=0.04, 0.06, 0.08, 0.1) samples have impurity phase of Sn_3O_4. The peaks corresponding to Sn_3O_4 increases with an increase in Sn concentration till x=0.08, further it decreases in α-$Sn_{0.1}Fe_{1.9}O_3$ and α-$Sn_{0.2}Fe_{1.8}O_3$. The variation in the lattice parameter indicates the substitution of the Sn^{4+} ions in the lattice sites of Fe^{3+}.

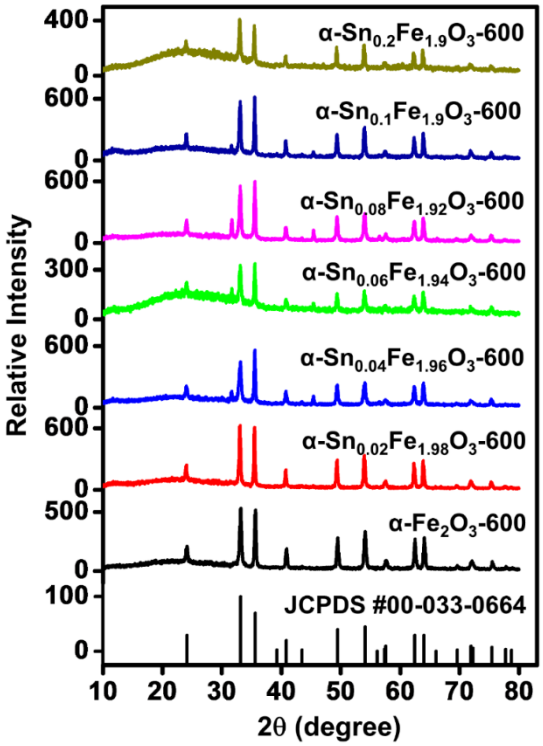

Figure 3.16 XRD patterns of α-$Sn_xFe_{2-x}O_3$ along with JCPDS #00-033-0664.

Table.3.6. Structural parameters of α-$Sn_xFe_{2-x}O_3$ from XRD.

x	a (Å)	c (Å)	c/a	Unit cell volume (nm^3)	Grain size (nm)	Dislocation density ($d \times 10^{14}$ m^{-1})
0	5.0695	13.8344	2.72895	0.3079	63	2.519
0.02	5.06742	13.8364	2.73046	0.3077	38	6.925
0.04	5.05414	13.75474	2.72148	0.3043	28	1.275
0.06	5.05142	13.81593	2.73506	0.3053	32	9.765
0.08	5.04932	13.78289	2.72965	0.3043	33	9.182
0.1	5.05318	13.77324	2.72566	0.3046	43	5.408
0.2	5.06092	13.8089	2.72854	0.3063	36	7.716

3.2.3 Scanning Electron Microscopy (SEM) and Energy Dispersive Diffraction Spectra (EDS) and mapping

FESEM and EDS images of $Sn_xFe_{2-x}O_3$ are shown in Figure 3.17. FESEM images clearly show the nano-plate like structures of $Sn_xFe_{2-x}O_3$. In microwave assisted synthesis, the particles are formed by the dissolution recrystallization process, which is Ostwald ripening growth mechanism. In microwave assisted synthesis, the optimal temperature required for the reaction reaches very fast due to the internal heat produced in samples (K et al. 2016, Milosevic et al. 2011). In a typical reaction, the Fe^{3+} ions react with the OH^- ions and hydrolyzed to form β-FeOOH (Zhang et al. 2008). On annealing the samples at 600° C, β-FeOOH dehydrogenizes to form α-Fe_2O_3 nanoplates like structure. The doping of tin ions is confirmed by EDS. The EDS spectra of all samples show the presence of Fe and Sn only and the absence of any impurity in the samples. The EDS mapping of tin for all the samples.

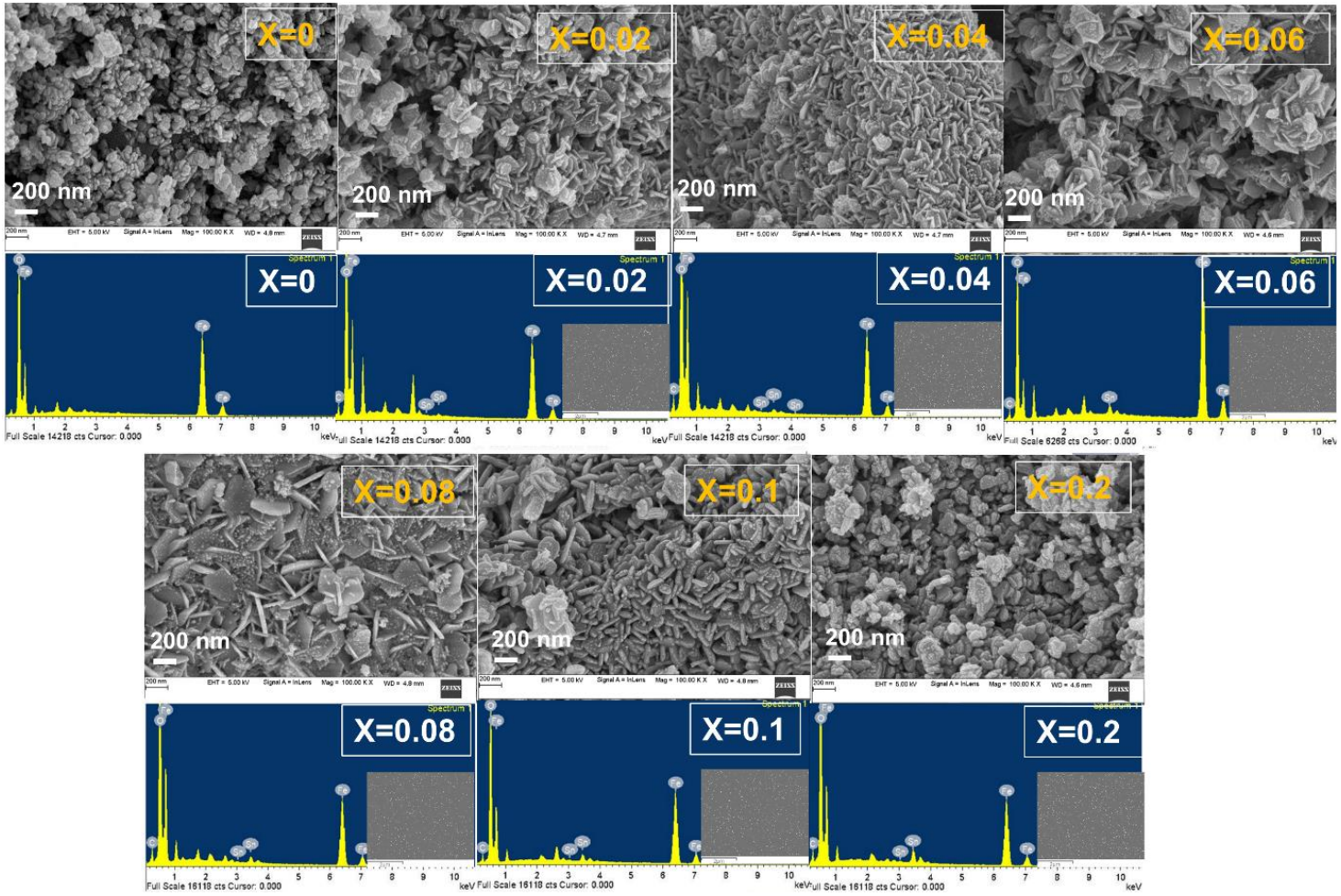

Figure 3.17 FESEM images, EDS spectra and Sn elemental mapping of α-$Sn_xFe_{2-x}O_3$.

3.2.4 DC electrical resistivity

The dc electrical resistivity measurement was done at room temperature, using two-probe method. The DC resistivity of α-$Sn_xFe_{2-x}O_3$ was estimated using the relation (Ali et al. 2013),

$$\rho_{dc} = \frac{A}{Rd} \ldots\ldots\ldots\ldots (33)$$

where d and A are thickness and area of the pellets respectively and R is the resistance of the sample (Figure 3.18). The measured values of DC resistivity are tabulated in Table.3.7. dc resistivity decreased with increase in conenttration till x=0.06. However, it increases with further increase in the concentration of tin doping. The DC resistivity of iron oxides is highly dependent on the hopping of electrons between Fe^{3+} and Fe^{2+} in octahedral sites (Farid et al. 2017). Thus, tin doping above x=0.06 may reduce the number of Fe^{3+} ions in octahedral sites, which reduces hopping probability in hematite. This may leads to the increase in the resistivity above 4% of tin doping in hematite.

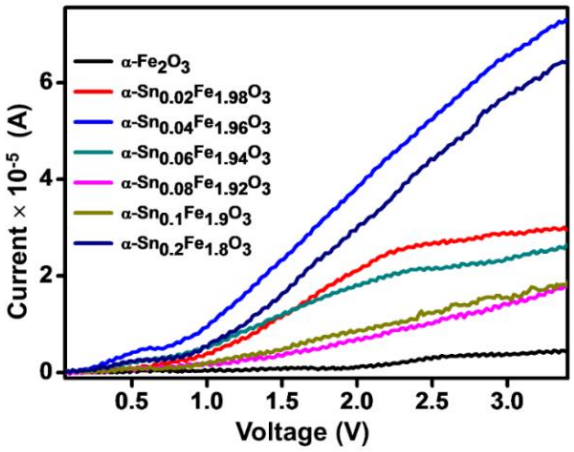

Figure 3.18 I-V curves of α-$Sn_xFe_{2-x}O_3$ with different concentration of tin.

3.2.5 AC conductivity

The frequency dependency of AC conductivity was studied in the frequency ranging from 40 Hz to 1 MHz at room temperature. Fig 3.19(a) shows the variation of AC conductivity with frequency. The AC conductivity of samples, increases with an

increase in frequency. The AC conductivity was plotted as a function of angular frequency ($\omega=2\pi f$) to understand the type of polarons involved in hopping mechanism. Figure 3.19(b) shows the plot of log (AC conductivity) vs log(ω^2), which is almost linear for all the samples, which confirms small polaron hopping in the samples (Ashwini et al. 2017, Kadam et al. 2004, Rosso et al. 2003). At lower frequencies, conduction is highly influenced by grain boundaries, whereas, grains contribute to the conduction at high frequencies. Also at lower frequencies, the electron hopping between ferric and ferrous ions is slow, as frequencies increase the grains facilitate the hopping, thereby increasing the AC conductivity. The observed decrease in conductivity with increase in the concentration of tin can be explained by the microstructure of the sample, the hopping probability and hopping length of the electrons. Contribution from the insulating grain boundaries is more in the case of smaller grains, which result in a low conductivity of the material (Pervaiz et al. 2014).

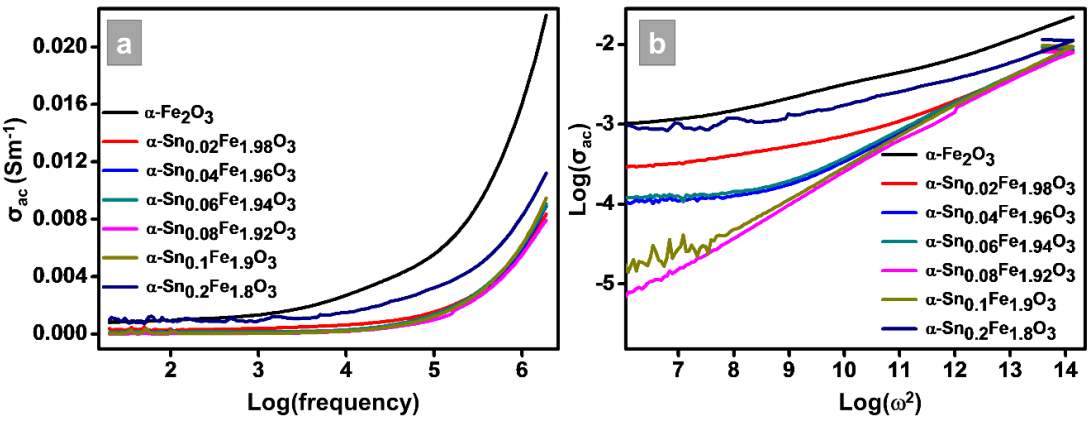

Figure 3.19 AC conductivity of α-$Sn_xFe_{2-x}O_3$ as a function of (a) frequency and (b) angular frequency.

AC conductivity values at 1 KHz applied frequency for different compositions of α-$Sn_xFe_{2-x}O_3$ are given in the Table. 3.7. The conductivity decreases with the increase in the concentration of tin till the composition x=0.08 and then decreases for x= 0.1 and 0.2. This may be due to the reduction of Fe^{3+} ions in octahedral sites and the creation of Fe^{3+} vacancies by the substitution of Sn^{4+} ions.

3.2.6 Impedance spectroscopy

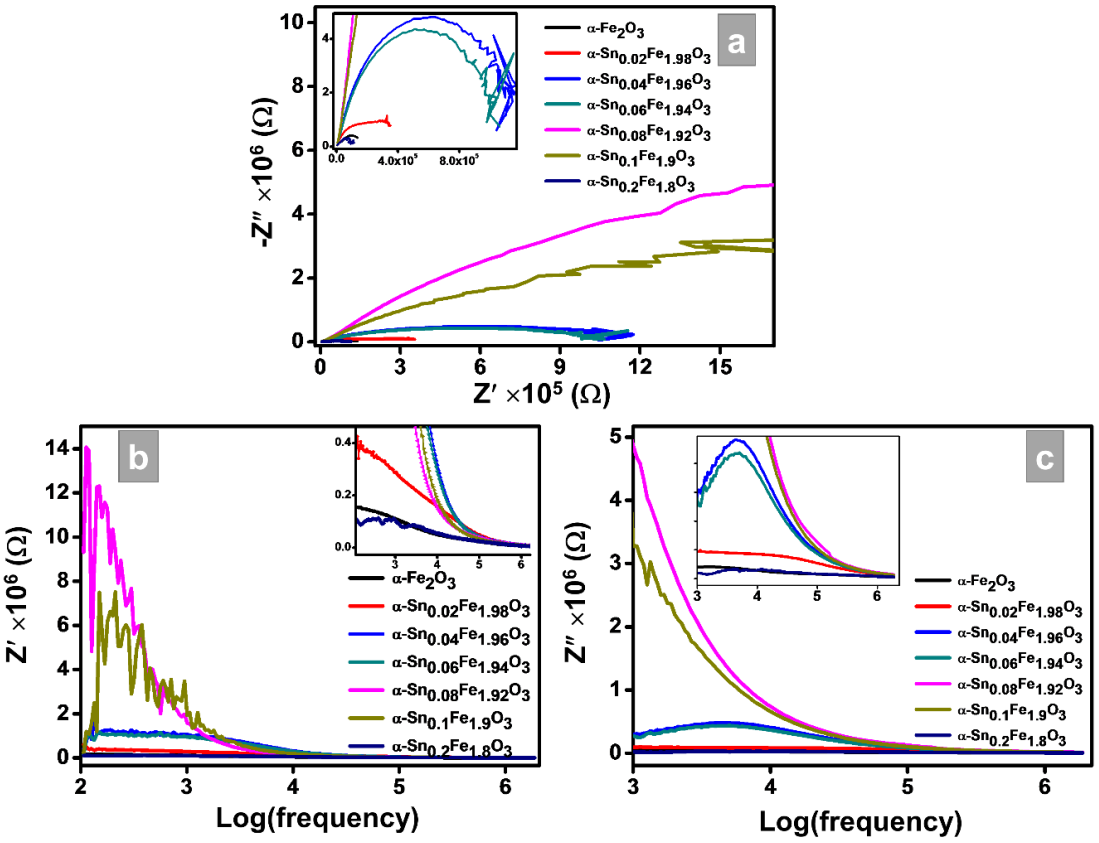

Figure 3.20 (a) Nyquist plot of α-$Sn_xFe_{2-x}O_3$ (b) real and (c) imaginary impedance as a function of frequency.

The impedance study was carried out at room temperature by applying an AC electric field with frequency ranging from 40 Hz to 1 MHz. Figure 3.20(b) shows the dependence of the real part of the impedance (the resistive part) for different composition of tin doped hematite. The figure clearly shows a decrease in Z′ with an increase in the applied frequency, which indicates the increase of AC conductivity with frequency and this is confirmed by the AC conductivity study (see Figure 3.19(a)). Figure 3.20(c) shows the variation of imaginary impedance with applied frequency, which indicates the reactive part of the impedance. From the inset of Figure 3.20(c), it may be noticed that samples $Sn_{0.04}Fe_{1.96}O_3$ and $Sn_{0.06}Fe_{1.94}O_3$ show peak at mid frequency. It appears that the peak shifts to lower frequency ranges in samples $Sn_{0.08}Fe_{1.92}O_3$ and $Sn_{0.1}Fe_{1.9}O_3$, and to mid frequency range for the sample $Sn_{0.2}Fe_{1.8}O_3$.

The resonance frequency is directly proportional to the hopping probability of Fe^{3+} ions in the octahedral sites. As the Sn concentration increases the number of Fe^{3+} ions in octahedral sites decreases and also there will be creation of octahedral vacancies. The variation in the hopping probability leads to the shift in the resonance frequency (Rezlescu et al. 1974).

The complex impedance measurements give information about the electrical properties of the material. Depending on the properties of a material, a Cole-Cole plot gives two semicircles. The semicircle at low-frequency region represents the grain boundary resistance. Whereas, the second one in the high-frequency region is due to the grain resistance or bulk properties. Figure 3.20(a) shows the Cole-Cole plots of α-$Sn_xFe_{2-x}O_3$. A single semi circle for all samples indicates the dominant grain boundary effect in conduction process. We can observe noise for samples α-$Sn_xFe_{2-x}O_3$ (x=0.04, 0.06, 0.08 and 0.1) at lower frequency ranges, which may be attributed to the presence of Sn_3O_4 phase in the samples.

3.2.7 Dielectric properties

Figure 3.21 shows frequency dependence of dielectric constant at room temperature. From the Figure 3.21, we can observe that dielectric constant has high values at low frequencies and decreased with the increase in frequency and then remains constant. This typical behaviour of dielectric constant is due to the dielectric relaxation (Haque et al. 2017). Under the influence of applied electric field at low frequencies, the localized accumulation of charge builds up the space charge polarization, which leads to high dielectric constant. As frequency increases, charge accumulation at the grain boundary reduces, which reduces the polarization, resulting in the reduction of dielectric constant. This behaviour can be explained by Koop's phenomenological theory as in the case of nickel doped ferrites (Koops 1951). The dielectric structure is made up of high conductive grains separated by low conductive grain boundaries. However, in ferrites, the electrical polarization is due to the directional electric field produced by the exchange of electrons between ferrous (Fe^{2+}) and ferric (Fe^{3+}) ions.

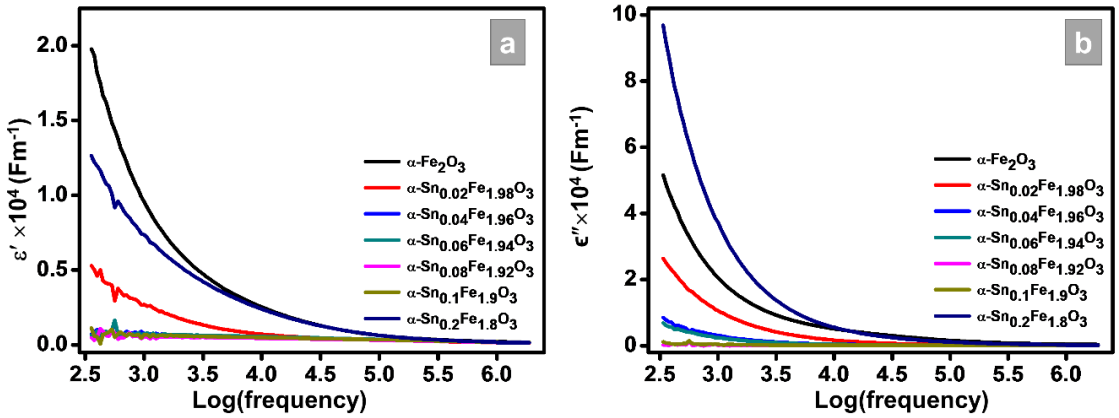

Figure 3.21 Real and imaginary dielectric constants of α-$Sn_xFe_{2-x}O_3$ as a function of frequency.

3.2.8 Modulus properties

The frequency dependence of electric modulus was studied in the frequency range of 100Hz to 1 MHz. The modulus M″ for α-$Sn_{0.1}Fe_{1.9}O_3$ has relaxation peak near 20 kHz as shown in Figure 3.22(b). The inset of Figure 3.22(b) shows the relaxation peaks at lower frequencies for samples with x=0.04, 0.06 and 0.1. However, the peak shifted towards higher frequency for samples α-$Sn_{0.1}Fe_{1.9}O_3$ and α-$Sn_{0.2}Fe_{1.8}O_3$. The relaxation peaks are resonance peaks, where the applied frequency coincides with the frequency of the oscillating dipoles (Assar et al. 2014).

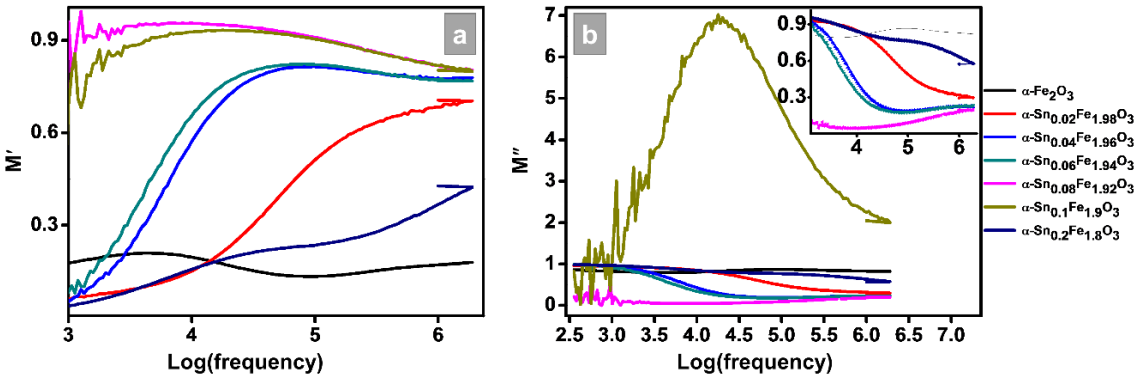

Figure 3.22 Frequency dependency of real and imaginary electric modulus of α-$Sn_xFe_{2-x}O_3$.

3.2.9 Loss factor (Dissipation factor)

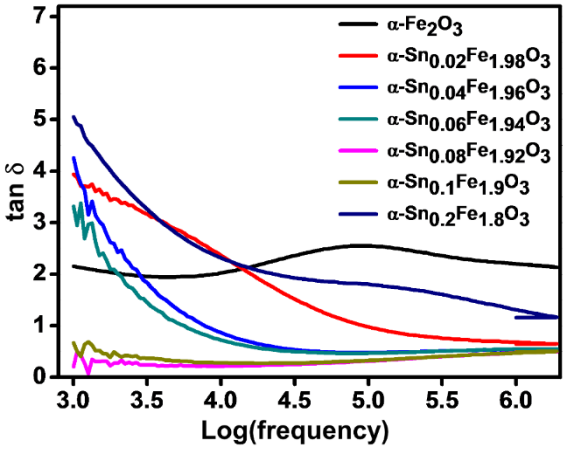

Figure 3.23 Loss factor of α-$Sn_xFe_{2-x}O_3$ as a function of frequency.

A plot of loss factor versus frequency is shown in Figure 3.23. The loss factor decreases with increasing frequencies. Its magnitude with respect to doping concentration at any applied frequency shows a nonlinear variation. The sudden decrease of loss factor at low-frequency ranges can be ascribed to the organized growth of domains and the major impact of the diamagnetic dopant. The insignificant decrease of tan δ at high frequencies may be due to the probable mismatch of domain size with the frequency of the applied field (Sridhar et al. 2016). Loss tangent shows relaxation peak for α- $Sn_xFe_{2-x}O_3$ similar to the various doped iron oxides reported earlier (Dar et al. 2010, Ramesh et al. 2016, Mujasam Batoo 2011). The shift in the peak position to lower frequency and reduction in the peak height indicates the variation of the hopping probability of the electrons with the doping. The hopping probability depends on the number of Fe^{3+} ions in the octahedral sites. However, on doping with tin, the number of Fe^{3+} in the octahedral sites decreases, which reduces the hopping probability.

Table.3.7 DC resistivity, AC conductivity, loss factor, and Dielectric constant of α-$Sn_xFe_{2-x}O_3$ at 100 kHz.

x	DC resistivity ρ_{dc} (Ω-m)	AC conductivity (Sm^{-1})	Loss factor	Dielectric constant (Fm^{-1})
0	43270	0.0055	2.5465	634.25
0.002	11323	0.0015	0.9767	329.17
0.004	5014	0.0013	0.4777	355.06
0.006	3747	0.0014	0.4659	359.38
0.008	10374	0.0009	0.3143	315.90
0.1	14701	0.0012	0.3245	348.21
0.2	9629	0.0032	1.8057	635.31

3.2.10 Vibrating Sample magnetometry (VSM)

The magnetization was measured against the applied magnetic field (H) using vibrating sample magnetometer at room temperature. From the Figure 3.24, we can observe the hysteresis loops with the absence of significant saturation magnetization, which is a common behaviour of hematite(Kopanja et al. 2016). The coercivity, retentivity, and the saturation magnetic field values are given in table 3.7.

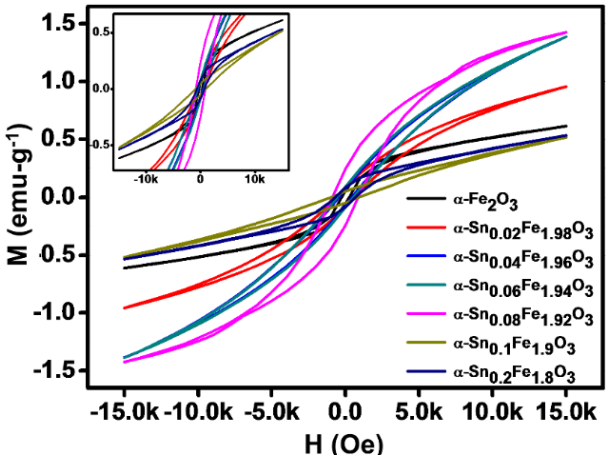

Figure 3.24 M-H curves of α-$Sn_xFe_{2-x}O_3$.

The coercivity increases with increase in the concentration of tin in hematite till x=0.1 (for the sample (α-$Sn_{0.02}Fe_{1.98}O_3$). It is low for the sample α-$Sn_{0.2}Fe_{1.8}O_3$, but the value of coercivity is still higher than that of pure hematite (α-Fe_2O_3). The coercivity of hematite increases with the doping of Sn atom. The Sn doped α-Fe_2O_3 samples have high coercivity values in the range of 446 to 950 G. This can be an intrinsic property of the tin doped hematite nanoparticles because of the vacancies created by Sn^{4+} doping in the hematite structure (Srikrishna Ramya et al. 2014). The saturation magnetization increases with the increase in doping of the tin till α-$Sn_{0.08}Fe_{1.92}O_3$ and decreased for α-$Sn_{0.1}Fe_{1.9}O_3$ and α-$Sn_{0.2}Fe_{1.8}O_3$ samples. The decrease in the saturation magnetization in these samples can be attributed to the surface magnetic anisotropy. There will be a mismatch between the surface spin relaxation and core magnetization direction, which reduces the effective magnetization. Similar kind of reduction in the magnetization for the doped iron oxide nanoparticles were reported by several authors (Chakrabarti et al. 2005, Kamali et al. 2013, Xu et al. 2015, Mitra et al. 2009, Srikrishna Ramya et al. 2014). The nano-plate like morphology of α-$Sn_xFe_{2-x}O_3$ samples is also a reason for the high coercivity of the samples (Tadić et al. 2011).

Table.3.8 Coercivity (H_C), saturation magnetization ((M_S) and retentivity (M_R) of α-$Sn_xFe_{2-x}O_3$.

x	H_C (Oe)	Ms (emu/g)	M_R (emu/g)
0	252.54	0.61392	0.05674
0.02	577	0.95728	0.077
0.04	446.68	1.3866	0.07054
0.06	548.69	1.3877	0.08908
0.08	872.26	1.4263	0.24394
0.1	950.04	0.51794	0.04998
0.2	676.78	0.535	0.08593

3.3 Summary

- Nickel doped ferrite samples were successfully prepared using microwave assisted method
- The annealing temperature influences the structural properties of the samples. The samples annealed at 450 °C have a mixed phase of rhombohedral and spinel structures, whereas samples annealed at 600 °C have a single rhombohedral phase.
- The doping concentration of nickel influences the structural properties of the ferrites. The undoped ferrite annealed at both 450 forms a mixed phase of hematite and magnetite. On adding nickel ions, hematite phase reduces and disappears in $Ni_{0.04}Fe_{y-0.04}O_z$-sample completely.
- SEM images show the agglomerated nanoparticles because of the hot spots formation on microwave treatment. EDS and mapping confirm the absence of impurities and uniform distribution of Ni throughout the samples.
- Both, Nickel concentration and annealing temperature influence the electrical and magnetic properties of ferrites. Nickel doped ferrite samples annealed at 450 °C have higher AC conductivity and dielectric constant than that of the samples annealed at 600 °C.
- Nickel doped ferrite samples annealed at 450 °C have higher saturation magnetization than the samples annealed at 600 °C because of the transformation to hematite on annealing at 600 °C.
- Tin doped hematite nanoplates were prepared using simple microwave assisted method.
- The prepared α-$Sn_xFe_{2-x}O_3$ nanoplates reveal the rhombohedral crystal structure and the doped tin substitutes the Fe^{3+} octahedral sites, as confirmed by the XRD.
- DC resistivity decreases with an increase in tin doping till 3% and increases with further doping.
- AC conductivity reveals the small polarons hopping mechanism involved in the conduction. The dielectric studies confirm the space charge polarization.
- The magnetization study shows the antiferromagnetic behaviour of the samples with high coercivity (446 G to 950 G).

CHAPTER 4

Dielectric Properties of MFe_2O_4 (M: Fe, Zn, Ni and Sn) Nanoparticles Prepared by Hydrothermal Method and Application as Chronoamperometric H_2O_2 Sensor

This chapter deals with the preparation of spinel structured MFe_2O_4 (M: Fe, Zn, Ni and Sn) nanoparticles using single step hydrothermal method. It also includes the study of structural, morphological and dielectric properties of prepared nanoparticles along with their applications in non-enzymatic H_2O_2 sensor. XRD confirms the spinel structure of the samples with substitution of Zn, Ni and Sn in the lattice sites of Fe. FTIR spectra of all samples have characteristic υ_1 and υ_2 bands. SEM and EDS mapping show uniform distribution of cations throughout the samples. $ZnFe_2O_4$ and $SnFe_2O_4$ have higher AC conductivity and dielectric constant than that of Fe_3O_4 and $NiFe_2O_4$, which can be attributed to the different cationic arrangement in the spinel structure. Further, electrochemical studies show that, $ZnFe_2O_4$ and $SnFe_2O_4$ have superior H_2O_2 sensing performance than Fe_3O_4 and $NiFe_2O_4$, which can be attributed to the lower redox potential of Sn^{2+}/Sn^{4+} couple, lower charge-transfer resistance and higher specific surface area. $ZnFe_2O_4$ and $SnFe_2O_4$ have a sensitivity of 4.411 and 3.915 $\mu A/mM/\mu g$, respectively, which is greater than that of Fe_3O_4 (0.434 $\mu A/mM/\mu g$) and $NiFe_2O_4$ (0.644 $\mu A/mM/\mu g$). $SnFe_2O_4$ has the lowest limit of detection (2.6 μM) with good selectivity towards H_2O_2 in presence of other interference agents.

4.1 Preparation of MFe_2O_4 (M: Fe, Zn, Ni, Sn) nanoparticles.

To prepare zinc ferrite/nickel ferrite/tin ferrite, an aqueous solution of 50 mM of zinc/nickel/tin salt was mixed with 100mM of $FeSO_4$ $7H_2O$ solution and 0.1 ml of hydrazine hydrate (N_2H_4 H_2O) was added. The solution mixture was stirred well for 30 min to get a homogeneous solution and transferred to a teflon jar. This mixture was hydrothermally treated at 180 ^oC for 48 hours in a hot air oven. Then, the precipitate was separated by centrifugation, and cleaned with water and acetone. The sample was

dried at 60 ºC for 15 hours in a hot air oven to obtain the desired nano-ferrite sample. A pristine iron ferrite (magnetite) sample was prepared by repeating the above procedure only with the solution of iron salt. Prepared samples were pressed into pellets under a pressure of 8 ton using a hydraulic press, to study their electrical and dielectric properties.

4.2 Structural and morphological properties

4.2.1 X-ray Diffraction

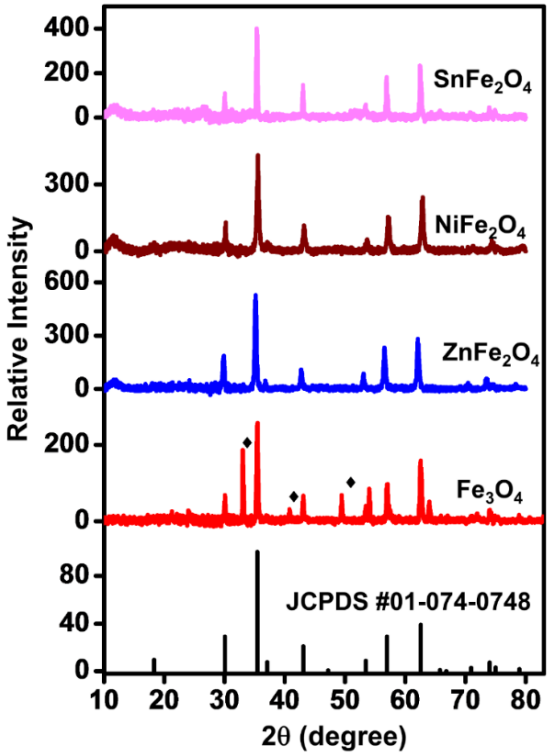

Figure 4.1. XRD patterns of Fe_3O_4, $ZnFe_2O_4$, $NiFe_2O_4$, $SnFe_2O_4$ and JCPDS #01-074-0748. The peaks indexed with ♦ corresponds to Fe_2O_3 phase.

The structural analysis of the prepared ferrites was done using powder XRD in the 2θ range of 10 to 80°. Figure 4.1 shows the XRD patterns of Fe_3O_4, $ZnFe_2O_4$, $NiFe_2O_4$, and $SnFe_2O_4$ nanoparticles. Patterns of prepared samples matches JCPDS data #01-074-0748, which is a face centred cubic structure. We can observe extra peaks in the pattern of magnetite, which matches with the hematite phase of iron oxide. These peaks are absent in the patterns of zinc ferrite, nickel ferrite and tin ferrite, which

indicates the formation of single spinel ferrite phase in these samples. The small shift in the maximum intensity peak of magnetite on addition of other cations indicates the substitution of these cations into the lattice sites of iron ions.

The lattice parameters, unit cell volume, grain size and dislocation density of MFe_2O_4 samples are listed in Table 4.1. The variation in the lattice parameter indicates the substitution of Zn^{2+}, Ni^{2+} and Sn^{4+} in the lattice sites of Fe ions. The grain sizes of MFe2O4 (M: Zn, Ni and Sn) are lesser than that of Fe_3O_4, which can be attributed to the formation of vacancies on substitution of Zn^{2+}, Ni^{2+} and Sn^{4+} ions (Feueerbach 2005) . The smaller grain size leads to higher dislocation density in zinc, nickel and tin ferrite nanoparticles.

Table.4.1. Lattice parameter, unit cell volume, grain size and dislocation density from XRD.

Material	a (Å)	Unit cell volume (nm^3)	Grain size (nm)	Dislocation density ($\delta \times 10^{14}$ m^{-2})
Fe_3O_4	8.389	590.55	66	2.3
$ZnFe_2O_4$	8.460	605.56	37	7.3
$NiFe_2O_4$	8.379	588.39	36	7.7
$SnFe_2O_4$	8.411	595.12	50	4

4.2.2 Fourier Transform Infrared spectroscopy

Figure 4.2 shows the FTIR spectra of Fe_3O_4, $ZnFe_2O_4$, $NiFe_2O_4$, and $SnFe_2O_4$. The ferrite nanoparticles show characteristic bands of ferrites in the wavenumber ranging from 400 to 500 cm^{-1}. Fe_3O_4 has υ_1 band at 454 cm^{-1}, which is the characteristic vibrational stretching mode of M-O in tetrahedral sites and υ_2 at 426 cm^{-1} can be attributed to the vibrational stretching mode of M-O in octahedral sites (Rathod et al. 2017, Zhang et al. 2013, Singh et al. 2011). υ_1 and υ_2 bands for $SnFe_2O_4$ (Figure 4.2d) are at 463 and 426 cm^{-1}, respectively. There is a shift in υ_1 band, which is due to the substitution of Sn ions. Whereas, $ZnFe_2O_4$ and $NiFe_2O_4$ have extra bands in the same

range, which may be due to the presence of different ions at tetrahedral and octahedral sites. FTIR of ferrites confirms the substitution of metal ions in the lattice sites of Fe.

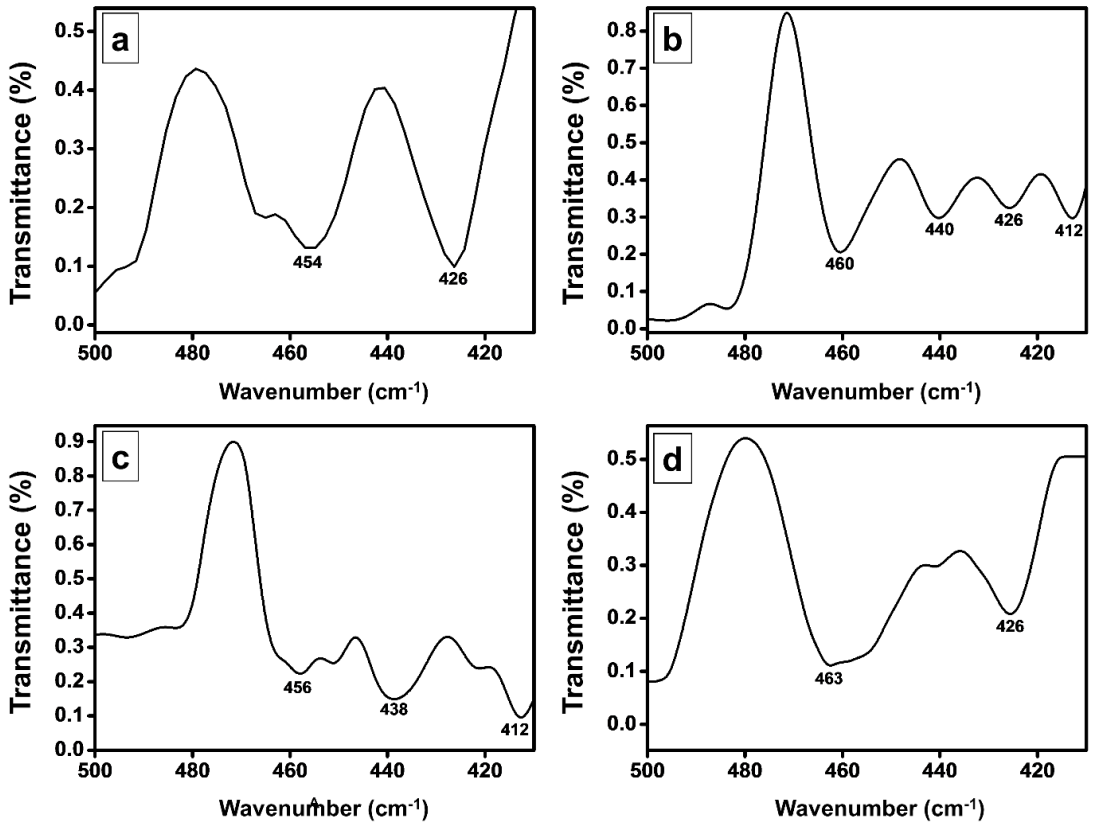

Figure 4.2 FTIR spectra of (a) Fe_3O_4, (b) $ZnFe_2O_4$, (c) $NiFe_2O_4$ and (d) $SnFe_2O_4$.

4.2.3 Scanning Electron Microscopy and Energy Dispersive X-ray Spectroscopy (EDS)

Figure 4.3 shows the SEM images and EDS graphs of Fe_3O_4, $ZnFe_2O_4$, $NiFe_2O_4$ and $SnFe_2O_4$. Fe_3O_4, $ZnFe_2O_4$ and $NiFe_2O_4$ nanoparticles have nano-sphere shaped agglomerated particles, while $SnFe_2O_4$ has nano-rod like structure. From EDS spectra of MFe_2O_4 nanoparticles we can observe that, except carbon from the carbon tape used for the sample preparation, there is no other impurities in any sample. Mapping shows the uniform distribution of cations throughout the samples (Shown in insets of EDS spectra).

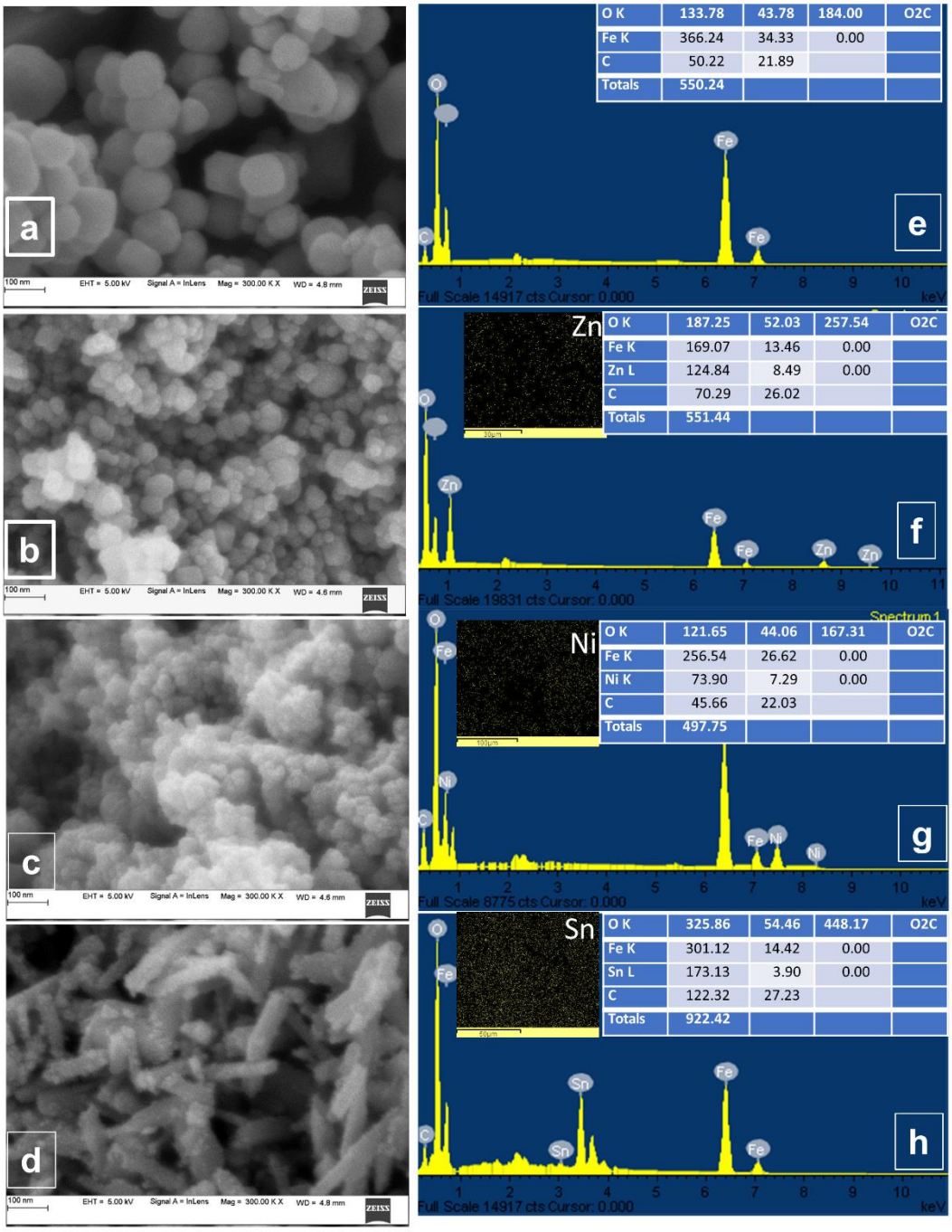

Figure 4.3 SEM images and EDS of (a and e) Fe_3O_4, (b and f) $ZnFe_2O_4$, (c and g) $NiFe_2O_4$ and (d and h) $SnFe_2O_4$ respectively.

4.2.4 BET surface area

Specific surface area, pore volume and pore diameter of Fe_3O_4, $ZnFe_2O_4$, $NiFe_2O_4$ and $SnFe_2O_4$ were estimated using nitrogen adsorption-desorption isotherm

multi point BET analysis. Adsorption isotherms of Fe_3O_4, $ZnFe_2O_4$, $NiFe_2O_4$ and $SnFe_2O_4$ are given in the Figure 4.4. From the slope of the isotherm, specific areas of nano-ferrite samples were estimated and is tabulated in Table.4.2.

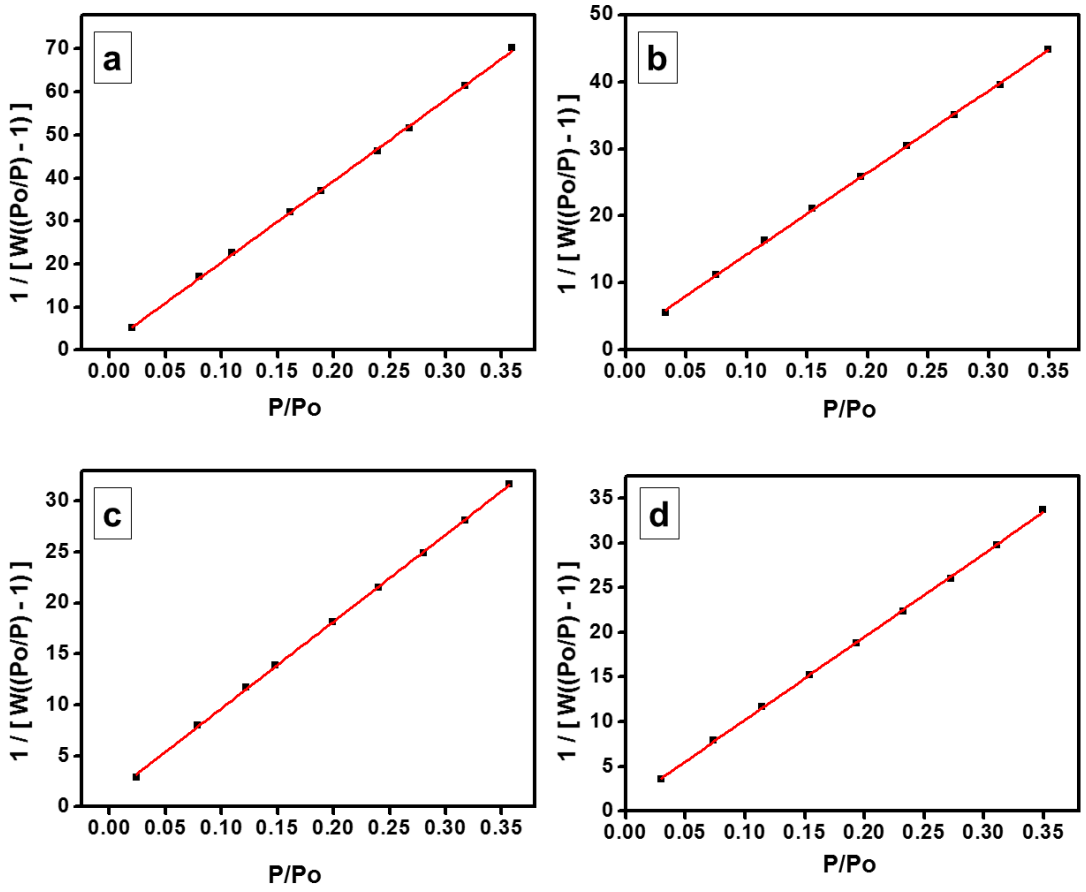

Figure 4.4 Adsorption isotherm of (a) Fe_3O_4, (b) $ZnFe_2O_4$, (c) $NiFe_2O_4$ and (d) $SnFe_2O_4$.

Table.4.2 Specific surface area, pore volume and pore diameter of Fe_3O_4, $ZnFe_2O_4$, $NiFe_2O_4$ and $SnFe_2O_4$ from BET analysis.

	Specific surface area (m^2/g)	Pore volume (cc/g)	Pore diameter (nm)
Fe_3O_4	18.26	0.044	1.659
$ZnFe_2O_4$	40.31	0.087	7.121
$NiFe_2O_4$	28.025	0.094	9.565
$SnFe_2O_4$	37.090	0.057	3.35

4.3 Electrical properties

4.3.1 AC conductivity

The variation of AC conductivity with frequency ranging from 4 Hz to 5 MHz at room temperature. Figure 4.5(a) shows the frequency dependent AC conductivity for Fe_3O_4, $ZnFe_2O_4$, $NiFe_2O_4$ and $SnFe_2O_4$. The AC conductivity of prepared samples increases with the increase in frequency, it is due to the hopping of electrons between Fe^{2+} and Fe^{3+} ions, which can be explained using Maxwell-Wagner bi-layered model (same as nickel and tin doped ferrites). Figure 4.5(b) shows the AC conductivity as a function of angular frequency ($\omega=2\pi f$). The plot of log (σ_{ac}) vs log (ω^2) is linear for all ferrite samples, which indicates the conduction due to small-polaron hopping (Ashwini et al. 2017, Kadam et al. 2004). AC conductivity values for an applied frequency of 100 kHz, for different ferrites, are given in Table. 4.3.

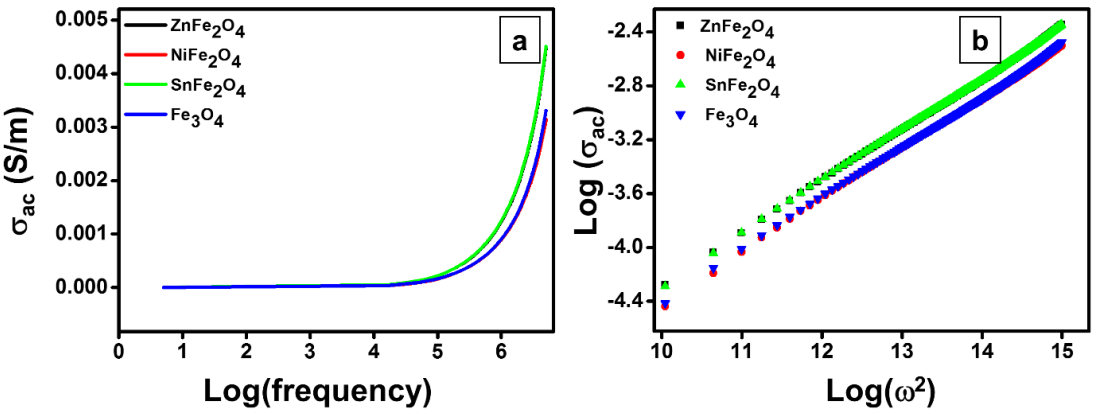

Figure 4.5 AC conductivity (σ_{ac}) as a function of (a) frequency and (b) angular frequency (ω).

The conductivity in ferrites is due to electron exchange mechanism between cations like Fe^{2+}/Fe^{3+}, Ni^{2+}/Ni^{+}, Zn^{2+}/Zn^{+} and Sn^{2+}/Sn^{4+} (Kambale et al. 2009). The AC conductivity of Fe_3O_4 and $NiFe_2O_4$ is lower compared to that of $ZnFe_2O_4$ and $SnFe_2O_4$, which may be due to the cationic arrangement in the samples. Fe_3O_4 and $NiFe_2O_4$ have inverse spinel structure, in which half of the Fe^{3+} ions replace the Fe^{2+} ions in octahedral sites, which reduces the hopping probability of electrons, which leads to lower values of AC conductivity (Auwal et al. 2016). While, in $ZnFe_2O_4$, Zn^{2+} ions occupy only

octahedral sites with no change in the number of Fe^{3+} ions in tetrahedral sites, which helps in the electron hopping, leading to the higher value of AC conductivity. In $SnFe_2O_4$, both Fe^{3+} and Sn^{4+} ions are at tetrahedral sites, which contributes to the high AC conductivity.

4.3.2 Dielectric properties

The dielectric behaviour of prepared ferrites was studied at room temperature in a frequency range of 4 Hz to 5 MHz. Figure 4.6 shows the frequency-dependent of real and imaginary parts of dielectric constant, both of which increases with an increase in the applied frequency. This kind of behaviour can be qualitatively explained by the polarization mechanism in ferrites, which is similar to that of the conduction process. As in the case of Ni and Sn doped ferrites, the frequency dependence of dielectric constant of ferrites can be explained by Koop's phenomenological theory (Kōō 1971, Koops 1951).

The dielectric constants of Fe_3O_4, $ZnFe_2O_4$, $NiFe_2O_4$ and $SnFe_2O_4$ at 100 kHz are given in the table.4.3. The dielectric constants of $SnFe_2O_4$ and $ZnFe_2O_4$ are higher than that of Fe_3O_4 and $NiFe_2O_4$, which is due to the cationic distribution in the spinel structure. The dielectric constant of ferrites depends on the number of Fe^{2+} ions in octahedral sites and Fe^{2+} ions can be easily polarizable than Fe^{3+} ions (Ajmal et al. 2017, A. K et al. 2017). In $NiFe_2O_4$, Ni^{2+} ions occupy octahedral sites and half of the Fe^{3+} ions occupy octahedral sites by replacing Fe^{2+} ions forming inverse spinel structure. This decreases the number of Fe^{3+} ions at the tetrahedral sites, thereby decreasing electron hopping. This results in a decrease of electron accumulation at the grain boundaries, which in turn leads to lower dielectric constant. While in normal spinel structure like $ZnFe_2O_4$, there will be enough Fe^{3+} ion available for electron hopping, which results in a high dielectric constant (Babu, Sailaja, et al. 2018).

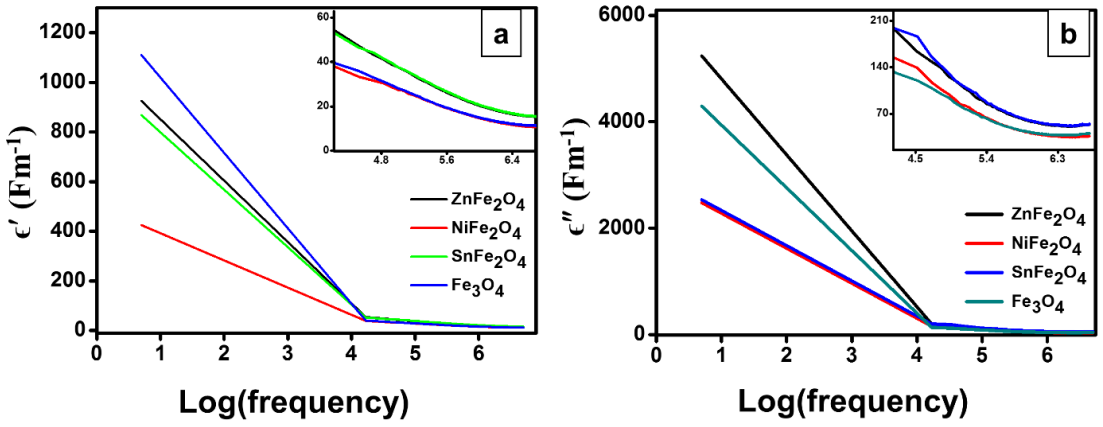

Figure 4.6 Frequency dependence of (a) Real and (b) Imaginary dielectric constant.

4.3.3 Electrical modulus

The electrical response and the homogeneity of polycrystalline samples can be analysed by studying complex electrical modulus. Figure 4.7 shows the dependence of M' and M″ on the frequency of the applied electric field for ferrite samples. We can observe relaxation peaks for all the samples, which are resonance peaks where the frequency of the applied field matches the frequency of the oscillating dipoles. The electric modulus also explains the probability of ion hopping in the material, which is directly proportional to the frequency of the relaxation peak (Farid et al. 2017, Koops 1951).

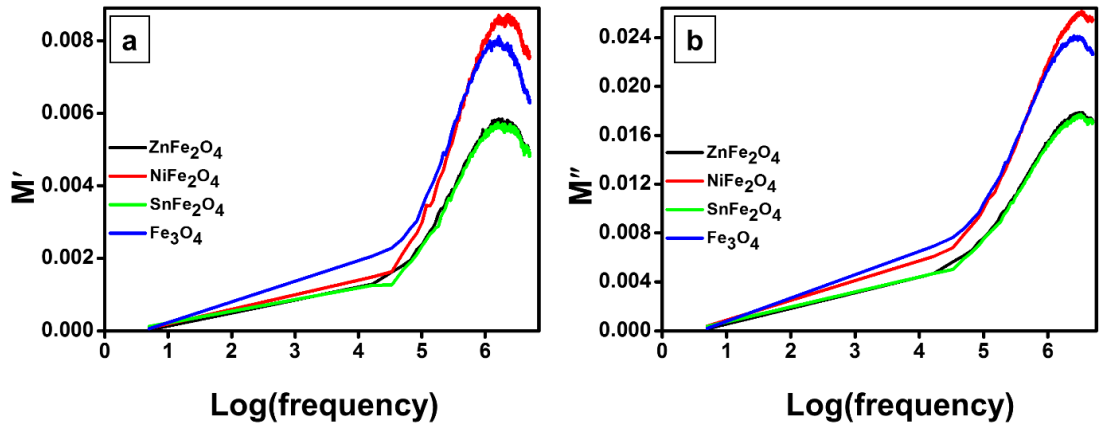

Figure 4.7 Frequency dependence of (a) real part and (b) imaginary part of the electrical modulus of Fe_3O_4, $ZnFe_2O_4$, $NiFe_2O_4$ and $SnFe_2O_4$.

4.3.4 Dielectric loss factor (Dissipation factor)

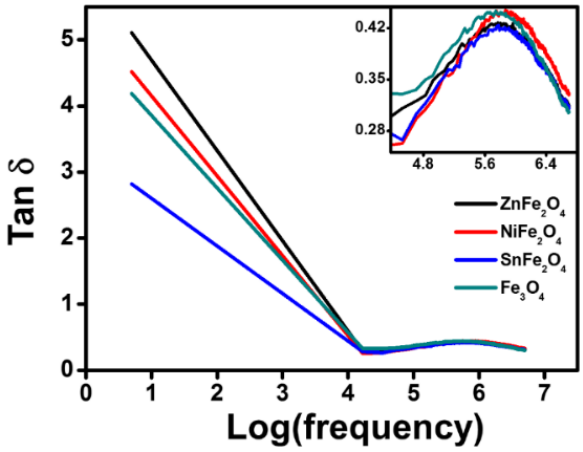

Figure 4.8 The dissipation factor of Fe_3O_4, $ZnFe_2O_4$, $NiFe_2O_4$ and $SnFe_2O_4$ versus frequency.

The energy lost in the material when an electric field is applied can be represented by the dielectric loss. It also estimates the eddy current loss in the alternating field due to domain wall resonance. Figure 4.8 shows the frequency dependence of loss factor of Fe_3O_4, $ZnFe_2O_4$, $NiFe_2O_4$ and $SnFe_2O_4$. The loss factor is high at low frequencies and decreases with an increase in the frequency. There is a relaxation peak at the higher frequency region for all the samples. According to Rezlesque model (Rezlescu et al. 1974), a peak appears when the frequency of the applied electric field matches the hopping frequency of the carriers (A.K et al. 2017). Resonance frequency (f_{max}) and relaxation time of Fe_3O_4, $ZnFe_2O_4$, $NiFe_2O_4$ and $SnFe_2O_4$ are tabulated in table.4.3. Fe_3O_4 (0.42481) and $NiFe_2O_4$ (0.43646) have comparatively high loss factor than $ZnFe_2O_4$ (0.41904) and $SnFe_2O_4$ (0.41504).

4.3.5 Complex impedance

Figure 4.9(b) shows Nyquist plots of Fe_3O_4, $ZnFe_2O_4$, $NiFe_2O_4$ and $SnFe_2O_4$. The Nyquist plots of all samples are single semi-circular arcs. Incomplete semi-circular arc shows that the resistance is out of measurement scale (Dar et al. 2010). The presence of the single semi-circular arc at higher frequency ranges is due to the electrical conduction by bulk grains (Kambale et al. 2009, Ye et al. 2003). The radii of arcs of nano ferrites are in the order Fe_3O_4< $NiFe_2O_4$ < $ZnFe_2O_4$ < $SnFe_2O_4$. Figure 4.9(a)

shows impedance spectra for Fe_3O_4, $ZnFe_2O_4$, $NiFe_2O_4$ and $SnFe_2O_4$ nano ferrites. The complex impedance decreases with an increase in frequency. The enhanced probability of hopping at high frequencies leads to the low values of impedance. This behaviour is reciprocal to the AC conductivity. The real impedance values of Fe_3O_4 and $NiFe_2O_4$ at 100kHz is 6.243 and 6.390 kΩ, which are higher than that of $SnFe_2O_4$ (4.395 kΩ) and $ZnFe_2O_4$ (4.492 kΩ).

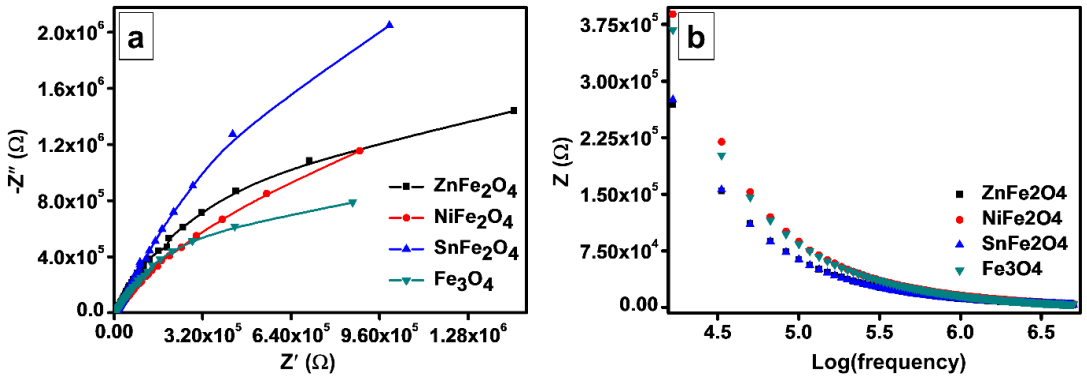

Figure 4.9 (a) Nyquist plot and (b) Frequency dependent complex impedance of Fe_3O_4, $ZnFe_2O_4$, $NiFe_2O_4$ and $SnFe_2O_4$.

Table.4.3 AC conductivity and Dielectric parameters of ferrite nanoparticles at 100 kHz.

Material	AC conductivity $\sigma_{AC} \cdot 10^{-5}$ (Sm^{-1})	Real dielectric constant / ϵ'	Real part of impedance / Z' (kΩ)	Real Part of electric modulus / $M' 10^{-5}$	Loss factor (tan δ)	Pre-exponential factor 'n'	Relaxation time from loss factor / τ (ns)
Fe_3O_4	0.897	1.50185	6.243	767	0.42481	0.686	97
$ZnFe_2O_4$	1.22	2.04962	4.492	551	0.41904	0.687	86
$NiFe_2O_4$	0.884	1.47763	6.390	797	0.43646	0.707	70
$SnFe_2O_4$	1.236	2.07926	4.395	544	0.41504	0.709	100

4.4 Electrochemical hydrogen peroxide sensor

4.4.1 Electrochemical Impedance Spectroscopy

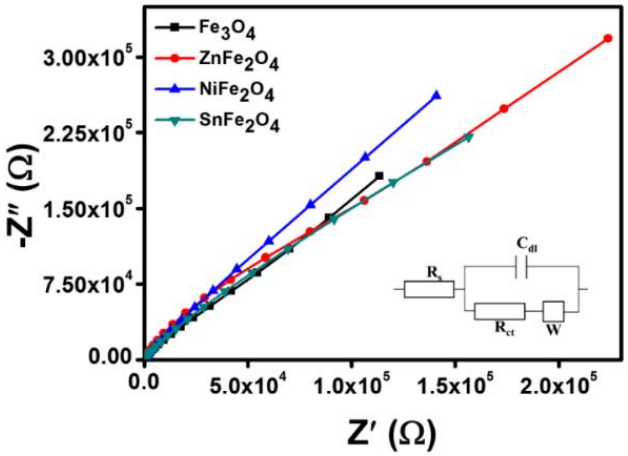

Figure 4.10 Electrochemical impedance spectra of Fe_3O_4, $ZnFe_2O_4$, $NiFe_2O_2$ and $SnFe_2O_4$. Inset is the equivalent circuit.

Electrochemical Impedance spectroscopy of Fe_3O_4, $ZnFe_2O_4$, $NiFe_2O_4$ and $SnFe_2O_4$ nanoparticles modified GCEs were performed in the frequency range of 1 MHz to 1 Hz to investigate the electrochemical properties at the interface of electrode and the electrolyte (0.1 M PBS) is given in the Figure 4.10. The EIS data was fitted to the equivalent circuit model (inset of Figure 4.10) using EC-lab software. The solution resistance (R_s) charge transfer resistance (R_{ct}), double layer capacitance (C_{dl}) and Warburg coefficient (s) are tabulated in table.4.4. From the table.4.4. it is noticed that the charge transfer resistance of $ZnFe_2O_4$ and $SnFe_2O_4$ is about two orders of magnitude lower than that of Fe_3O_4 and $NiFe_2O_4$, which indicates the higher electrochemical activity of $ZnFe_2O_4$ and $SnFe_2O_4$(Ma et al. 2014, Shanmugavani et al. 2014). This also correlates well with the specific surface area of $SnFe_2O_4$ (37.09 m^2g^{-1}) and $ZnFe_2O_4$ (40.3 m^2g^{-1}), which are higher than that of the Fe_3O_4 (18.26 m^2g^{-1}) and $NiFe_2O_4$ (28.025 m^2g^{-1}) nanoparticles. Larger surface area provides for a higher electrochemical interaction between the electrode and electrolyte, thereby reducing the charge transfer resistance.

Table 4.4. Parameters obtained by fitting the EIS data to the equivalent circuit and specific surface area from BET.

Samples	R_s (Ω)	C_{dl} (μF)	R_{ct} (Ω)	s (Ω-$s^{1/2}$)
Fe_3O_4	129	1.072	3636	122068
$NiFe_2O_4$	103	0.6918	3543	188428
$ZnFe_2O_4$	108	0.6465	159	270258
$SnFe_2O_4$	167	0.7043	77	196520

4.4.2 MFe_2O_4 based chronoamperometric H_2O_2 sensors

Cyclic voltammetry and chronoamperometry using three-electrode system in 0.1 M PBS solution (pH 7) with modified GCEs have been used to study the electrochemical H_2O_2 sensing performance of ferrite nanoparticles. Figure 4.11 represents the cyclic voltammograms of Fe_3O_4/GCE, $ZnFe_2O_4$/GCE, $NiFe_2O_4$/GCE and $SnFe_2O_4$/GCE with different concentrations of H_2O_2 at a scan rate of 50mVs^{-1}. The oxidation current increases with the increase in H_2O_2 concentration, which indicates the electrocatalytic activity of modified GCEs towards H_2O_2 sensing.

The mechanism of sensing of H_2O_2 by Fe_3O_4/GCE, $ZnFe_2O_4$/GCE, $NiFe_2O_4$/GCE and $SnFe_2O_4$/GCE can be explained by Haber-Weiss electrocatalysis mechanism (K et al. 2016). According to this, when an electron is transferred from the catalyst surface to the H_2O_2 molecule, it will yield a ⊕OH radical, and an electron will be transferred from H_2O_2 to the oxidised site of catalyst surface producing a ⊕HO_2 radical, which is a cyclic electron transfer process. The electrochemical reaction at the surface of MFe_2O_4 with M^{2+}/M^{3+} redox couples in the presence of H_2O_2 can be expressed as follows (Ding et al. 2015, Li et al. 2015),

$$M^{2+} + H_2O_2 \rightarrow M^{3+} + OH + OH^- \ldots\ldots\ldots\ldots (34)$$

$$H_2O_2 + OH \rightarrow H_2O + OOH \ldots\ldots\ldots\ldots (35)$$

$$M^{3+} + OOH \rightarrow M^{2+} + H^+ + O_2 \ldots\ldots\ldots\ldots (36)$$

While, Sn^{2+}/Sn^{4+} redox couple in $SnFe_2O_4$ provides two electrons compared to Fe^{2+}/Fe^{3+}, Zn^{2+}/Zn^{3+} and Ni^{2+}/Ni^{3+} (K et al. 2016).

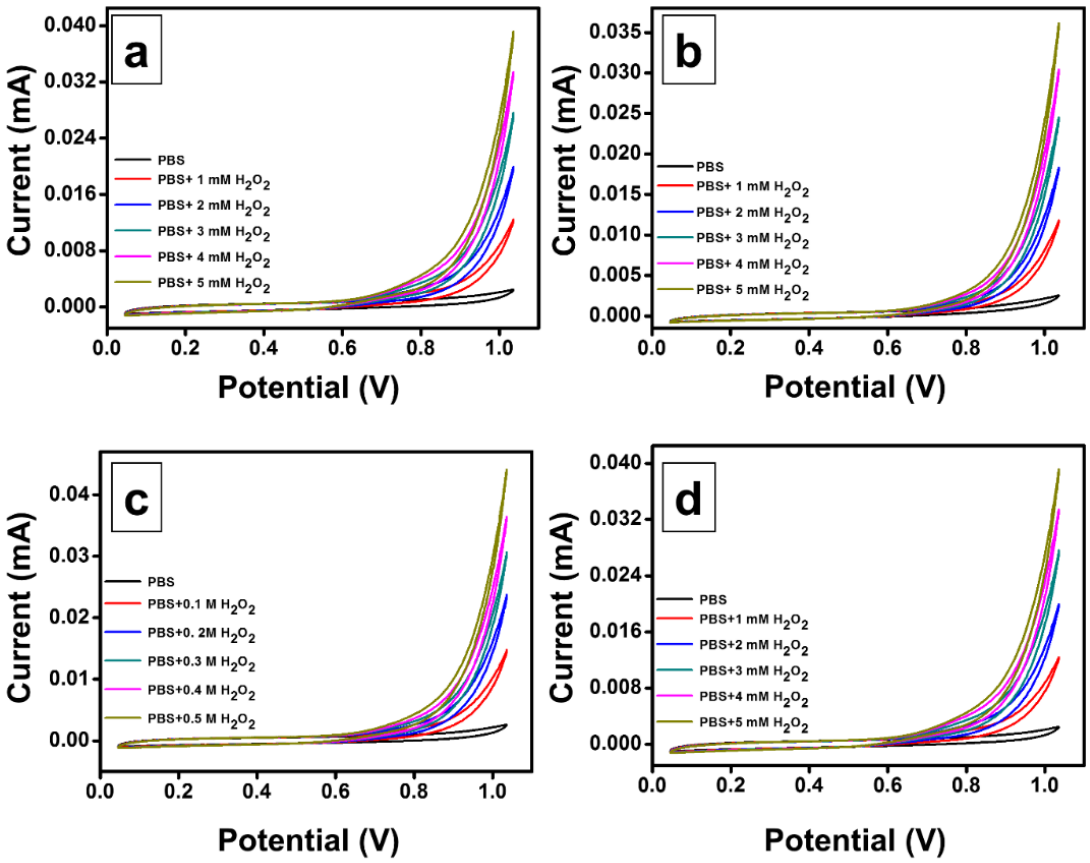

Figure 4.11 Cyclic voltammograms of (a) Fe_3O_4, (b) $ZnFe_2O_4$, (c) $NiFe_2O_4$ and (d) $SnFe_2O_4$ in the presence of different concentration of H_2O_2 in 0.1 M PBS solution of pH7 at a scan rate of 50 mVs^{-1}.

The chronoamperometric curves of Fe_3O_4/GCE, $ZnFe_2O_4$/GCE, $NiFe_2O_4$/GCE and $SnFe_2O_4$/GCE recorded at 0.9 V for successive addition of 0.1 M H_2O_2 are shown in Figure 4.12. On each addition of H_2O_2, current increases immediately, this fast response of sensors indicate the efficient reduction of H_2O_2. All modified GCEs show a good electrochemical response to a wide range (0 to 3 mM) of H_2O_2 concentrations. The sensitivity of MFe_2O_4 ferrites may be understood using the differences in the redox potential. It is to be noticed that the $ZnFe_2O_4$ and $SnFe_2O_4$ modified GCEs show better performance towards the sensing of H_2O_2. The redox potential for Fe^{2+} to Fe^{3+} is 0.77 V, while, the reduction potential of Ni^{2+} is above 0.25V, so they cannot initiate the

radical reaction. Therefore, Ni^{2+} ions do not contribute to the catalytic reduction process of hydrogen peroxide. However, we expect $SnFe_2O_4$ to show better performance compared to Fe_3O_4 since redox potential of Sn^{2+}/Sn^{4+} is 0.15 V, which is very much less than the redox potential of Fe^{3+}/Fe^{2+} (Jaime-González et al. 2016, Wolfenstine et al. 2005). In addition, high specific surface area and lower charge-transfer resistances of $SnFe_2O_4$ and $ZnFe_2O_4$ also contribute for their high sensing performance towards H_2O_2.

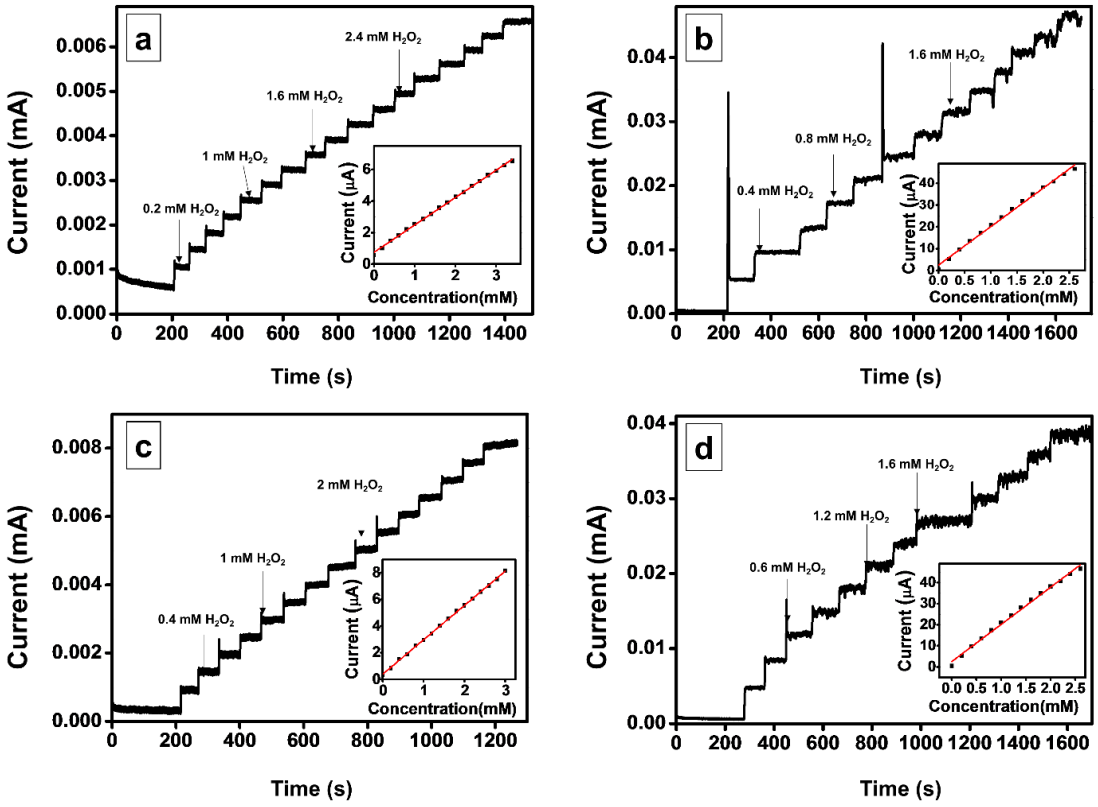

Figure 4.12 Chronoamperometric curves of (a) Fe_3O_4, (b) $ZnFe_2O_4$, (c) $NiFe_2O_4$ and (d) $SnFe_2O_4$ with the addition of H_2O_2 solution at different time intervals. Insets are the calibration curves of concentration of H_2O_2 and current.

The calibration curves given in the insets of Figure 4.12 show the linear increase of amperometric current with the increase in H_2O_2 concentration. $ZnFe_2O_4$/GCE and $SnFe_2O_4$/GCE have higher specific sensitivity of 4.41105 μA/mM/μg and 3.915 μA/mM/μg respectively than that of Fe_3O_4/GCE (0.4340 μA/mM/μg) and $NiFe_2O_4$/GCE (0.6442 μA/mM/μg). $SnFe_2O_4$ has the lowest limit of detection (LOD)

2.6 μM with signal to noise ratio of 3. However, it may be noted that the values reported here are best the values for pristine ferrite structure and it is comparable to that of the nanocomposites with carbon materials (CNT/graphene) (Yardımcı et al. 2012, Lu et al. 2013, Miao et al. 2013, Liu et al. 2015, Zhang, Li, et al. 2016, Ning et al. 2018). The morphology of the nanostructure also plays a significant role in the electrocatalytic activity.

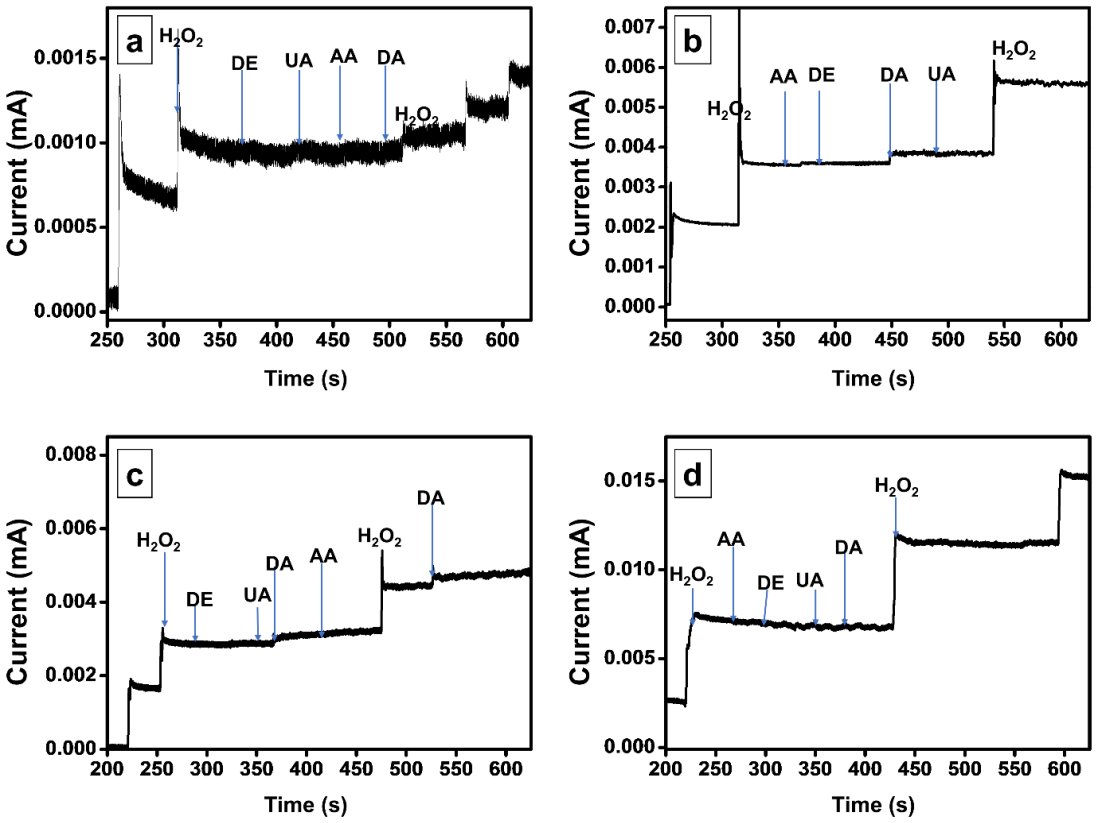

Figure 4.13. Chronoamperometric curves of (a) Fe_3O_4, (b) $ZnFe_2O_4$, (c) $NiFe_2O_4$ and (d) $SnFe_2O_4$ with the addition of H_2O_2, dextrose (DE), uric acid (UA), dopamine (DA) and ascorbic acid (AA).

The selectivity of Fe_3O_4, $ZnFe_2O_4$, $NiFe_2O_4$ and $SnFe_2O_4$ towards H_2O_2 was studied using chronoamperometry. Chronoamperometric curves were recorded at 0.9 V by adding 0.1 mM each of electroactive interference namely, ascorbic acid (AA), uric acid (UA), and dextrose (DE) and dopamine (DA) along with H_2O_2. From the CA curves given in Figure 4.13, we can observe that all the prepared nano ferrites are insensitive towards AA, UA and DE at the applied voltage. As observed in Figure 4.13

(b) and (c), there is a slight increase in current on the addition of dopamine, which indicates that $ZnFe_2O_4$ and $NiFe_2O_4$ are not completely selective for H_2O_2 in the presence of dopamine. While, $SnFe_2O_4$ is sensitive only to H_2O_2 in the presence of all added additives. The higher electrochemical sensing performance of $SnFe_2O_4$ can be attributed to the larger specific surface area, lowest charge transfer resistance and nano-rod like morphology.

4.5 Summary

- Magnetite (Fe_3O_4), zinc ferrite ($ZnFe_2O_4$), nickel ferrite ($NiFe_2O_4$) and tin ferrite ($SnFe_2O_4$) nanoparticles were prepared using hydrothermal method and they have spinel structure.
- The substitution of Zn^{2+}, Ni^{2+} and Sn^{4+} ions into the lattice sites of Fe^{2+}/Fe^{3+} ions confirmed from the change in the lattice parameters and shift in the characteristic vibrational band of FTIR spectra.
- The absence of impurities and equal distribution of cations is confirmed from the EDS mapping of the samples. Among all ferrites prepared, $ZnFe_2O_4$ and $SnFe_2O_4$ have higher AC conductivity and dielectric constant compared to Fe_3O_4 and $NiFe_2O_4$. In addition, $SnFe_2O_4$ and $ZnFe_2O_4$ have lower loss factor, which indicates the improvement of conduction on substitution of zinc and tin ions, which is useful for devices like sensors, supercapacitors.
- Among all, $ZnFe_2O_4$ and $SnFe_2O_4$ have a good performance towards the sensing of H_2O_2 with a specific sensitivity of 4.411 $\mu AmM^{-1}\mu g^{-1}$ and 3.915 $\mu AmM^{-1}\mu g^{-1}$, respectively. In addition, $SnFe_2O_4$ has the lowest limit of detection, long dynamical range and good selectivity, along with good specific sensitivity.
- The excellent electrochemical sensing performance of $SnFe_2O_4$ are attributed to its large specific surface area, lowest charge transfer resistance, lowest redox potential and nanorod like morphology.

CHAPTER 5

Preparation and electrochemical applications of Fe_2O_3 nanorods, $SnFe_2O_4$ microcubes and $SnFe_2O_4$@rGO/MWCNT nanocomposite

This chapter includes preparation of Fe_2O_3 nanorods and $SnFe_2O_4$ microcubes using microwave assisted method, and $SnFe_2O_4$@rGO/MWCNT nanocomposite using hydrothermal method. In the first part of the chapter, $SnFe_2O_4$ microcubes and Fe_2O_3 nanorods based supercapacitors and non-enzymatic hydrogen peroxide (H_2O_2) sensor are discussed. $SnFe_2O_4$ microcubes exhibit an enhanced specific capacitance of 172 Fg^{-1} at a scan rate of 5 mVs^{-1} in comparison to Fe_2O_3 nanorods (70 Fg^{-1}). The H_2O_2 sensing performance of the fabricated $SnFe_2O_4$ electrodes through chronopotentiometry studies in 0.1 M PBS solution (at pH 7) with a wide linear range reveals a good sensitivity of 2.7 $mV\mu M^{-1}\mu g^{-1}$, with a lowest detection limit of 41 nM at a signal-to-noise ratio of 3. In the second part of the chapter we discuss $SnFe_2O_4$@rGO/MWCNT nanocomposite based dopamine sensor and anode material for lithium ion battery (LIB). The specific sensitivity of $SnFe_2O_4$@rGO/MWCNT modified GCE is 0.01443 $\mu A\mu M^{-1}\mu g^{-1}$. The discharging and charging specific capacity of $SnFe_2O_4$@rGO/MWCNT as LIB anode material, are 1882 and 1998 $mAhg^{-1}$ respectively, with a coulombic efficiency of 91.1%.

5.1 $SnFe_2O_4$ microcubes and Fe_2O_3 nanorods based supercapacitor and Hydrogen peroxide sensor

5.1.1 Preparation of $SnFe_2O_4$ microcubes and Fe_2O_3 nanorods using microwave assisted method

In a typical synthesis, 100 mM $FeCl_3$•$6H_2O$ dissolved in 100 ml of doubly distilled water was mixed with 100 ml solution of 50 mM $SnCl_2$•$2H_2O$ at room temperature and stirred continuously for 30 min. Thereafter, NaOH flakes were directly added to increase the pH of the solution to 13 and it was stirred for 30 min. The final

reaction mixture was placed inside a microwave oven at 180 W of power for 5 min. After microwave treatment, the solution was allowed to cool down to room temperature, then it was centrifuged to collect the precipitate, and washed with excess of distilled water, and acetone. The washed precipitates were dried at 60 ˚C for 12 h and were annealed at 600 ˚C for 10 h in a muffle furnace. The final $SnFe_2O_4$ sample obtained after annealing were brownish black coloured powders.

Fe_2O_3 nanorod samples were prepared by following the same procedure as mentioned above in the absence of $SnCl_2 \bullet 2H_2O$. The precipitates of Fe_2O_3 obtained after annealing at 600˚C for 10 h were orange red.

5.1.2 Thermogravimetric analysis

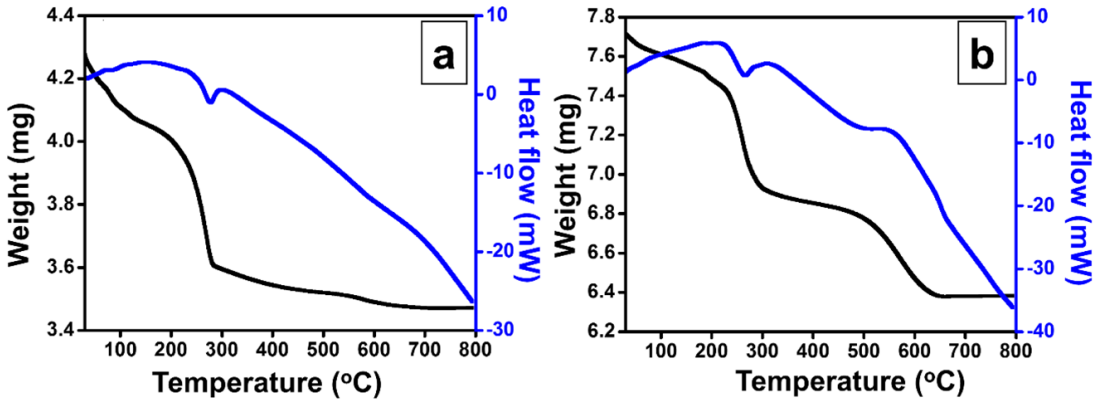

Fig 5.1 Thermogravimetric curves of α-Fe_2O_3 nanorods and $SnFe_2O_4$ microcubes.

The TGA and DSC data obtained by heating the samples in the temperature ranging from 40 to 800 °C for Fe_2O_3 and $SnFe_2O_4$ are presented in Figure 5.1. The weight loss till 200 ˚C observed in the TGA data for Fe_2O_3 can be attributed to the loss of water molecules, while the sudden drop in weight at around 270 ˚C indicates the phase transformation from magnetite to hematite (Pati et al. 2012, Topal et al. 2016). In case of $SnFe_2O_4$, the weight loss observed in the TGA data upto 250 °C can be attributed to the loss of water molecules, while the weight loss at around 290 °C could be because of the intermediate phase transformation due to the inclusion of Sn (cubic spinel structure), which is also confirmed from the endothermic peak in DSC appearing at around 285 °C. The final weight loss occurring at around 500 °C can be attributed to

the phase transformation from inverse spinel $SnFe_2O_4$ phase to rhombohedral $SnFeO_3$ phase. The weight loss of the sample continues till 800 °C, which indicates that transformation is not complete even at 800 °C.

5.1.3 X ray diffraction

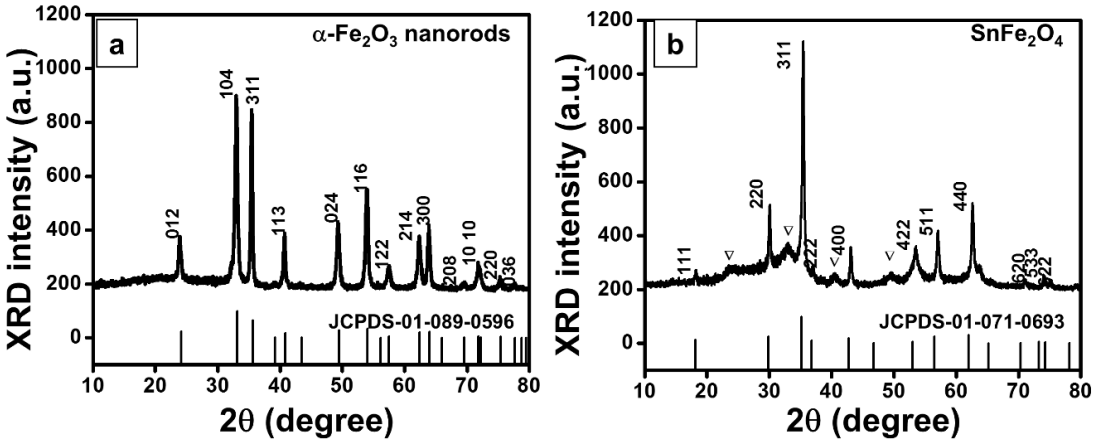

Fig 5.2 XRD patterns of (a) α-Fe_2O_3 nanorods and (b) $SnFe_2O_4$ microcubes.

XRD patterns of α-Fe_2O_3 and $SnFe_2O_4$ are shown in Fig 5.2(a) and 5.2(b). XRD peaks of Fe_2O_3 can be indexed to the rhombohedral structure of hematite (JCPDS card no. 01-089-0596) while the XRD pattern of $SnFe_2O_4$ matches well with pure monophasic inverse spinel structure (JCPDS card no. 01-071-0693) with a lattice constant of 8.4 Å (Spencer et al. 2015). However, the XRD patterns of as-synthesized precipitates of Fe_2O_3 as well as $SnFe_2O_4$ before annealing at 600 ^oC exhibit discrete phases. This indicates that Sn (in the form of Sn^{4+}) ions enter the octahedral sites by replacing Fe^{3+} ions, only when subjected to annealing for the formation of an inverse-spinel structured $SnFe_2O_4$. During sintering the excess Sn^{2+} ions get oxidized to form SnO phase (indexed with ∇ symbol in Figure 5.2(b), JCPDS card no. 01-085-0712). However, it can be observed from Figure 5.2(b) that the intensity of SnO peaks, as well as the percentage of SnO phase are much lower in comparison to $SnFe_2O_4$, indicating its negligible presence.

5.1.4 SEM and EDS

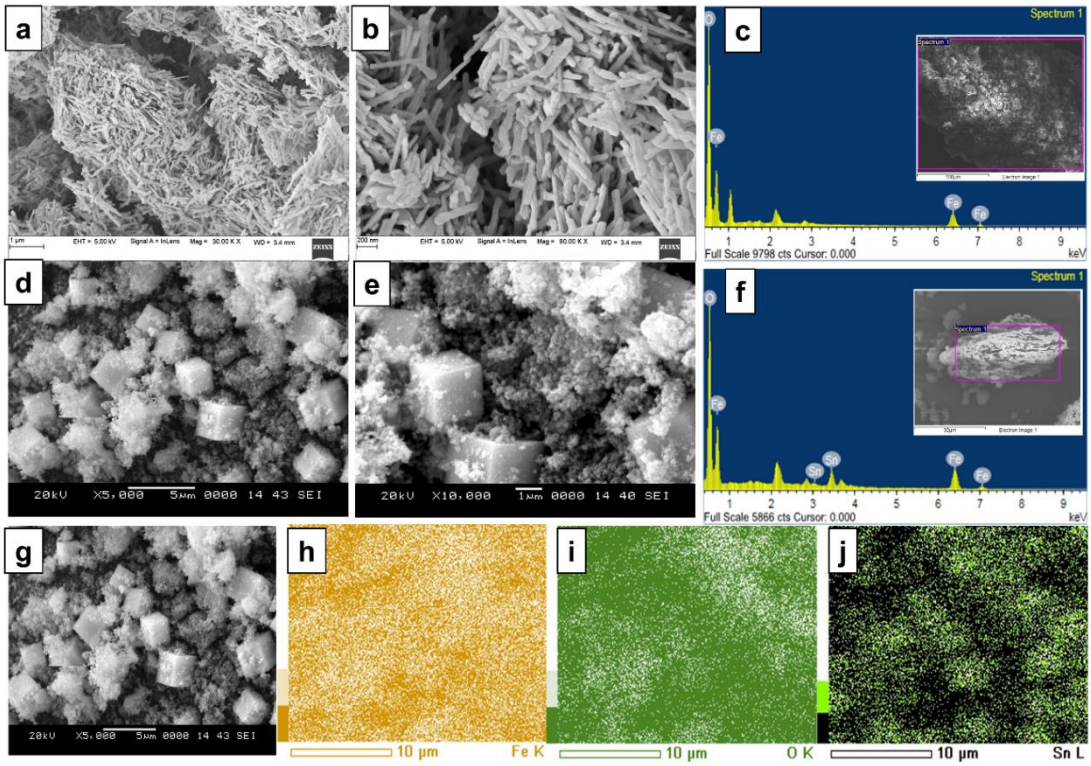

Figure 5.3 FESEM images, EDS spectra and Sn elemental mapping of α-Fe_2O_3 nanorods and $SnFe_2O_4$ microcubes.

The FESEM images clearly indicate the presence of Fe_2O_3 in the form of nanorods (see Figure 5.3(a), 5.3(b)), while $SnFe_2O_4$ exhibits micro-sized cube like structures (see Figure 5.3d, e) covered with some nanoparticle aggregates. Like in the case of nickel doped ferrites (**see section 3.1.4**), α-Fe_2O_3 nanorods and $SnFe_2O_4$ microcubes formed because of Owswald ripening mechanism on microwave treatment (Voepel et al. 2016). The XRD pattern of the obtained precipitates shows the presence of peaks corresponding to metallic Sn, Fe_3O_4 and SnO_2, while the corresponding SEM images indicates the presence of partially formed microcube like structures, covered with nanoparticle aggregates, which transformed into perfect $SnFe_2O_4$ microcubes (see Figure 5.1(b), Figure 5.3(d), and 5.3(e)) after being sintered at 600 ^oC for 10 h. As reported by Zheng et al. the formation of microcube like morphology can be attributed to the adsorption of Cl^- ions on the [110] planes of Fe_2O_3 with a relatively high density of iron, which restricts the faster growth during the recrystallization process (Zheng et

al. 2006). The high intensity [110] peak in the XRD pattern confirms the faceted growth of $SnFe_2O_4$, and the weight loss observed in the TGA data indicates the phase transformation. Furthermore, the inclusion of Sn^{2+} ions is also a key factor contributing to the faceted growth of perfect $SnFe_2O_4$ microcubes (Wang, Dou, et al. 2013, Sridharan and Park 2013, Sridharan, Jang, et al. 2013).

The presence of elemental peaks other than those of the synthesized compounds from the EDS spectra of Fe_2O_3 nanorods (Figure 5.3(c)) and $SnFe_2O_4$ microcubes (Figure 5.3(f)) obtained from the area marked in the FESEM image shown in their insets clearly reveals their purity. The unindexed peaks in the EDS correspond to the gold (Au) and palladium (Pd), which were coated on the sample before FESEM analysis to avoid the charging effects. The elemental maps corresponding to oxygen (O), iron (Fe) and tin (Sn) obtained by scanning the area shown in the FESEM image in Figure 5.3(g), clearly indicates the uniform distribution of all elements.

5.1.5 BET surface area analysis

The adsorption isotherms of Fe_2O_3 nanorods and $SnFe_2O_4$ microcubes are shown in Figure 5.4. The specific surface area, pore volume and pore area of Fe_2O_3 nanorods and $SnFe_2O_4$ microcubes are estimated using multipoint BET and given in table.5.1. $SnFe_2O_4$ has a specific surface area of 59.446 m^2g^{-1}, which is double the specific surface area of Fe_2O_3 (21.502 m^2g^{-1}).

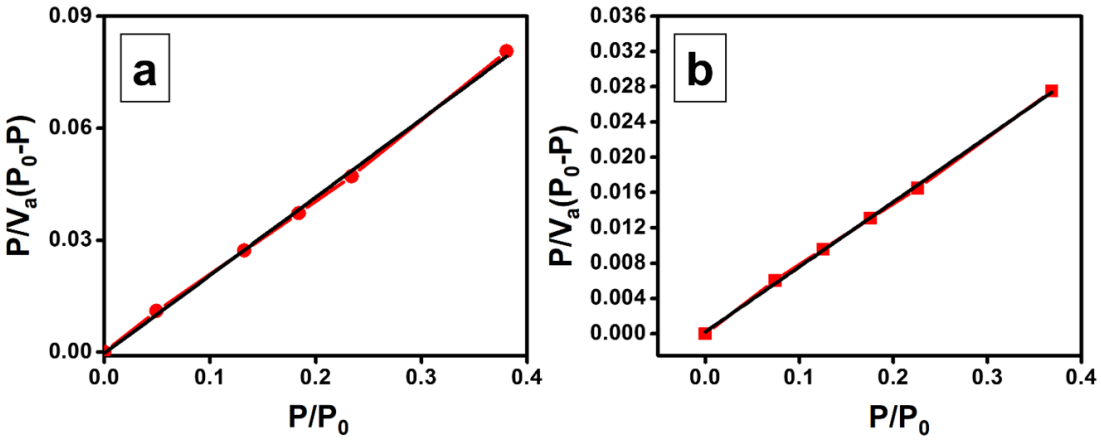

Figure 5.4. Multipoint BET plot of (a) Fe_2O_3 nanorods and (b) $SnFe_2O_4$ microcubes.

Table.5.1 Textural properties of the electrode materials evaluated using the Brunauer-Emmett-Teller (BET) method.

Sample	Mean pore Diameter (nm)	Total pore volume (cm^3g^{-1})	Specific surface area (m^2g^{-1})
Fe_2O_3	2.1829	0.01178	21.502
$SnFe_2O_4$	2.2103	0.032845	59.446

5.1.6 α-Fe_2O_3 nanorods and $SnFe_2O_4$ microcubes based supercapacitor electrodes

5.1.6.1 Cyclic voltammetry

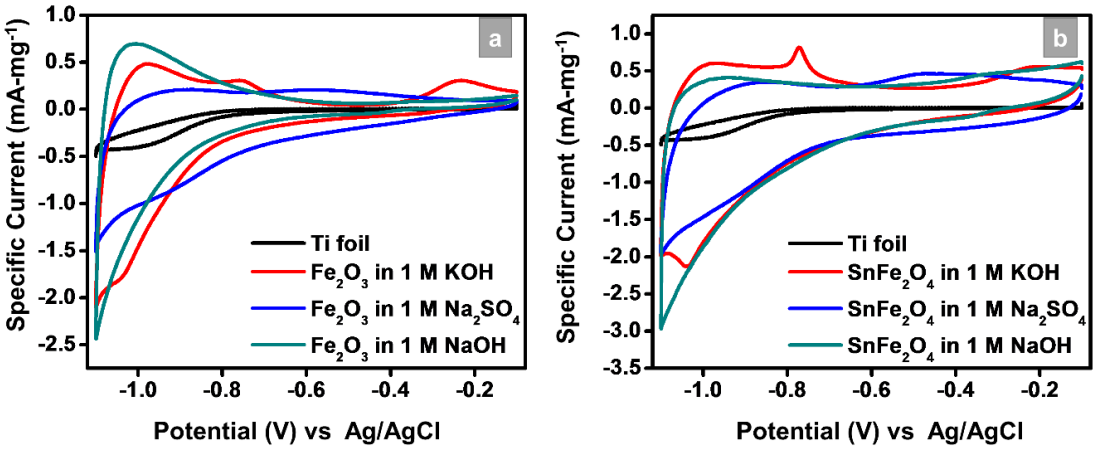

Figure 5.5 Cyclic voltammograms of (a) Fe_2O_3 and (b) $SnFe_2O_4$ recorded in different aqueous electrolytes at a scan rate of 10 mVs^{-1}.

The cyclic voltammograms (CV) of Fe_2O_3 and $SnFe_2O_4$ in various electrolytes at a scan rate of 10 mVs^{-1} is presented in Figure 5.5. Since, electrolysis of water takes place at 1.26 V, the potential window is optimized to 1 V between -1.1 and -0.1 V (Wang, Li, Cheng, et al. 2014). The distorted rectangular shape of the CV curves in Figure 5.5 represents the pseudo-capacitive behaviour and couple of redox peaks are present in 1 M KOH electrolyte, indicate the occurrence of faradaic redox reactions in both Fe_2O_3 and $SnFe_2O_4$. The redox reactions at the interface of the Fe_2O_3/$SnFe_2O_4$ electrode and electrolyte according to Pourbaix diagram can be written as (Shimizu et al. 2016, Hao et al. 2015),

$$Fe_2O_3 + H_2O \leftrightarrow 2Fe(OH)_2 + 2e^- \ldots\ldots\ldots\ldots (37)$$

$$SnFe_2O_4 + H_2O + OH^- \leftrightarrow Sn(OH)_2 + 2FeOOH + 2e^- \ldots\ldots\ldots\ldots (38)$$

The specific capacitance of the electrodes from CV curves are calculated using the **equation(25)**, (Wang, Hao, et al. 2014). The specific capacitances of Fe_2O_3 and $SnFe_2O_4$ in different electrolytes at a scan rate of 10 mVs^{-1} are tabulated in Table 5.2. At a scan rate of 5 mVs^{-1} in 1 M KOH, the specific capacitance of Fe_2O_3 and $SnFe_2O_4$ were 70 and 172 Fg^{-1}, respectively. The specific capacitances of Fe_2O_3 at 5 mVs^{-1} in 1 M NaOH and Na_2SO_4 are 60 and 55 Fg^{-1}, respectively, while for $SnFe_2O_4$ it was 112 and 115 Fg^{-1} in 1 M NaOH and Na_2SO_4 respectively. The observed variation in the specific capacitances using different electrolytes can be related to the difference in the size of the hydration sphere associated with the alkali ions (K^+, Na^+) in aqueous media. The smaller hydration sphere radius of K^+ ions (3.31 Å) compare to Na^+ (3.58 Å) enables higher mobility of charges during intercalation/deintercalation and reduction/oxidation reaction, which contributes to the high charge storage (Sankar et al. 2012, Lee et al. 1999).

Table 5.2. Specific capacitance (Fg^{-1}) of the prepared samples at a scan rate of 10 mVs^{-1} in different aqueous electrolytes.

Electrolytes	Specific capacitance (Fg^{-1})	
	Fe_2O_3	$SnFe_2O_4$
1 M KOH	56	106
1 M NaOH	52	98
1 M Na_2SO_4	58	84

Furthermore, $SnFe_2O_4$ exhibited good stability and was found to retain a specific capacitance of 97 Fg^{-1} even at a scan rate of 100 mVs^{-1}. The CV curves in Figure 5.6 represents the effects of scan rates on electrochemical performance of Fe_2O_3 and $SnFe_2O_4$ electrodes in 1 M KOH, Na_2SO_4 and NaOH. Since voltammetric current is directly proportional to scan rate, sweeping at higher scan rates increases the current of the CV resulting in reduced capacitance. Furthermore, compared to higher scan rates, the ions from the electrolyte at lower scan rates will have sufficient time to diffuse into

all available sites on the active electrode, leading to higher capacitance (Sreejesh et al. 2015).

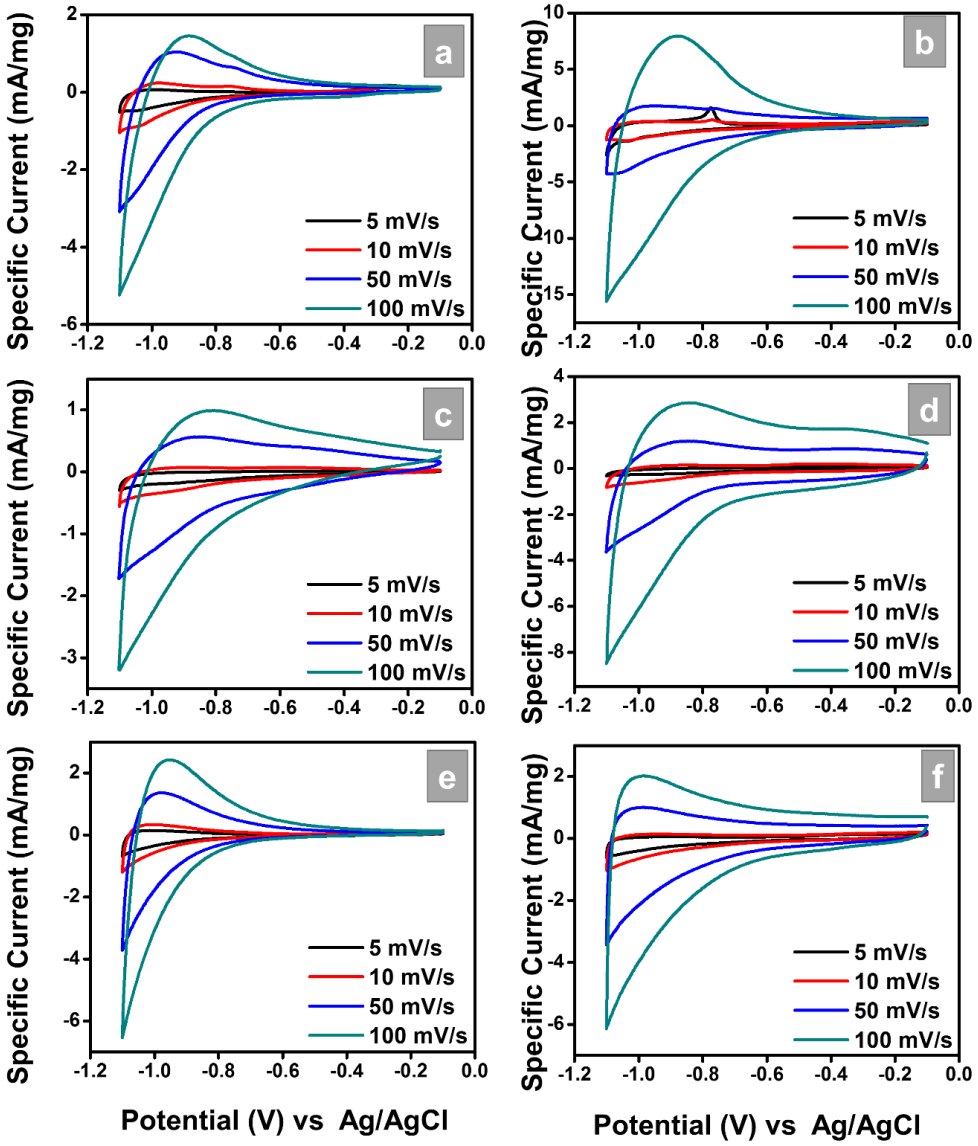

Figure 5.6 Cyclic voltammograms of Fe_2O_3 nanorods and $SnFe_2O_4$ microcubes as electrodes, recorded at different scan rates using (a, b) 1 M KOH, (c, d) 1 M Na_2SO_4 and (e, f) 1 M NaOH as aqueous electrolytes.

5.1.6.2 Galvanostatic Charge-Discharge

Electrochemical performance of the electrodes were also analysed through galvanostatic charge-discharge (GCD) method at different current densities, between

the potential-window of -1.1 and -0.1 V. The GCD curves of Fe_2O_3 and $SnFe_2O_4$ in 1 M Na_2SO_4, KOH and NaOH at a current density of 5 Ag^{-1} are presented in Figure 5.7. For Fe_2O_3 electrode, the GCD curves exhibit a typical saw-tooth shape, while there is a deviation from the symmetry in case of $SnFe_2O_4$, which indicates the pseudo-capacitance behaviour.

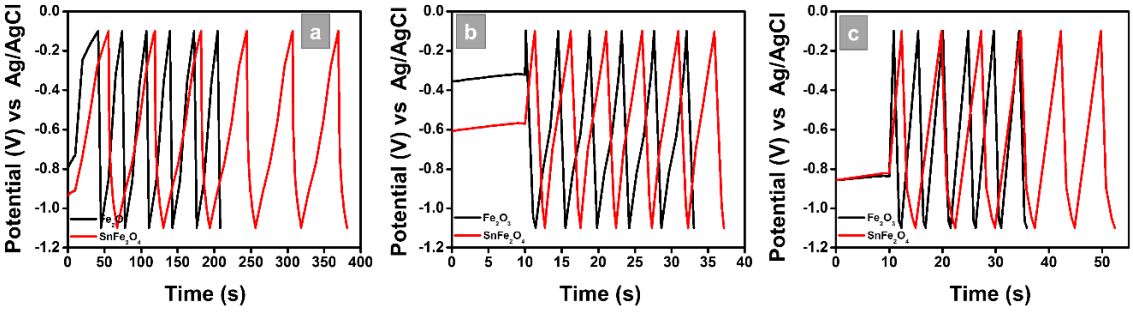

Figure 5.7 Galvanostatic charge-discharge curves of electrodes fabricated using Fe_2O_3 nanorods and $SnFe_2O_4$ microcubes in (a) 1 M Na_2SO_4, (b) 1 M KOH and (c) 1 M NaOH aqueous electrolytes at a constant current density of 5 Ag^{-1}.

5.1.6.3 Electrochemical Impedance Spectroscopy (EIS)

Electrochemical impedance spectroscopy (EIS) in the frequency range of 1 MHz to 1 Hz on Fe_2O_3 and $SnFe_2O_4$ electrodes were performed to quantitatively investigate the electrochemical characteristics of the electrodes/electrolyte interface. Figure 5.8(a) and 5.8(b) represent the Nyquist plots of Fe_2O_3 and $SnFe_2O_4$ electrodes in 1 M KOH aqueous solution, while their insets show the expanded view of high frequency region of the same plot. Supercapacitors are well known to exhibit a resistive behaviour (blocking) at higher frequencies and capacitive behaviour at lower frequencies (Ganesh et al. 2006). The obtained EIS data are consistent with the literature and as observed from the plots the EIS data points depicts very small kinetic arc in the high frequency region indicating the resistive behaviour of the electrodes, while the strain line at low frequency region represents their capacitive behaviour (Ganesh et al. 2006, Wang, Ji, et al. 2013).

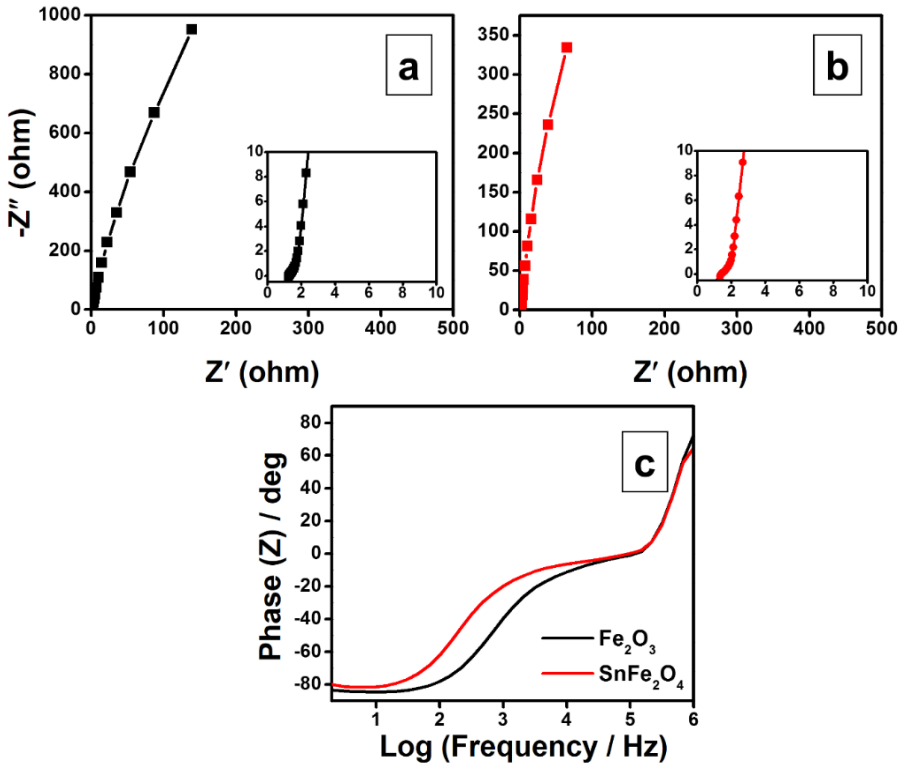

Figure 5.8 Nyquist plots of electrodes fabricated using (a) Fe_2O_3 nanorods and (b) $SnFe_2O_4$ microcubes in the presence of 1 M KOH aqueous solution (insets: expanded area of the same plot showing the high frequency region). (c) Bode plots of the fabricated supercapacitor electrodes indicating their pseudo-capacitive behaviour.

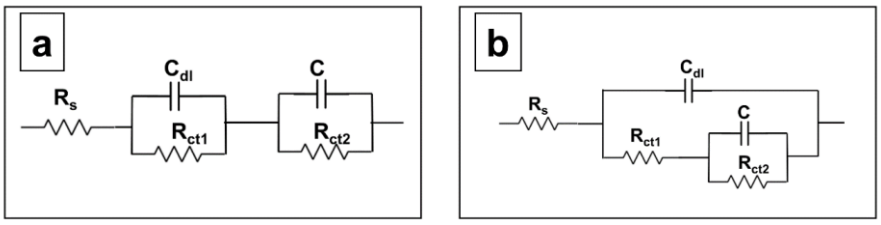

Figure 5.9 Equivalent circuits corresponding to (a) Fe_2O_3 and (b) $SnFe_2O_4$ electrodes obtained by fitting the EIS data with EC-lab software. In the figure, components are R_s-solution resistance, C_{dl}-double layer capacitance, and R_{ct}- charge transfer resistance.

EC-lab software was used to fit the EIS data to the equivalent circuit model (Figure 5.9) and the obtained parameters namely, R_s (electrode resistance), R_{ct1} (charge-transfer resistance), R_{ct2} (Faradaic charge-transfer resistance), C_{dl} (electrochemical double-layer capacitance) and C (Faradaic pseudo-capacitance) are shown in Table 5.3.

As seen from Table 5.3, the electrical conductivity of $SnFe_2O_4$ is higher than that of Fe_2O_3 owing to its lower value of R_s (Ma et al. 2014). The inclination of the lines at an angle greater than 45^o in the Nyquist plots (Figure 5.8(a), and 5.8(b)) is indication of the pseudo-capacitive behaviour of the electrodes (Shanmugavani et al. 2014). According to BET studies, the surface area (S_{BET} = 59.44 m^2g^{-1}) and pore volume (0.0328 cm^3g^{-1}) of $SnFe_2O_4$ is almost three times higher than that of Fe_2O_3. Owing to this reason, the electrolyte penetration and ion diffusion in $SnFe_2O_4$ is higher than that of Fe_2O_3, which can be directly correlated to the superior performance of $SnFe_2O_4$ as a supercapacitor electrode (Shanmugavani et al. 2014). Figure 5.8(c) shows the Bode plots of both Fe_2O_3 and $SnFe_2O_4$ supercapacitor electrodes. An electrochemical double layer capacitor is well known to have a phase angle equal to 90^o, while, in a pseudo-capacitor the angle varies. The phase angles for Fe_2O_3 and $SnFe_2O_4$ are almost identical (~ 80^o) indicating their suitability in the fabrication of low leakage supercapacitors.

Table 5.3. Parameters obtained by fitting the EIS data to the equivalent circuit.

Sample	**R_s /Ω**	**R_{ct1}/Ω**	**C_{dl} /μF**	**R_{ct2}/Ω**	**C /mF**
Fe_2O_3	8.62	1.456	0.1148	4.88	0.14
$SnFe_2O_4$	2.29	1.616	0.1047	1.39	0.397

The cycle-life of the Fe_2O_3 and $SnFe_2O_4$ electrodes were studied by measuring CV in 1 M KOH electrolyte at a scan rate of 20 and 50 mVs^{-1} for 1000 cycles as shown in Figure 5.10. As seen from Figure 5.10(a) after 1000 cycles the specific capacitances of both Fe_2O_3 and $SnFe_2O_4$ got reduced to 27 and 44 %, respectively while the scan rate was 50 mVs^{-1}. On the other hand, when the scan rate was reduced to 20 mVs^{-1} the Fe_2O_3 and $SnFe_2O_4$ electrodes were found to show good cyclic stability by retaining 70 and 86%, respectively of its initial capacitance value. The rapid decrease in the specific capacitance of the electrodes at higher scan rates (as seen in Fig 5.10(a)) could be attributed to a disproportionate reaction at the electrode surface. During initial cycles the specific capacitance is higher owing to the availability of more number of Sn/Fe atoms for the dissolution reaction with the electrolyte, which during subsequent cycles reduces resulting in the decline in the specific capacitance. On the other hand, at lower scan rates the ions from the electrolyte will have sufficient time to diffuse into all

available sites on the electrode surface leading to their better cycle life (Chen et al. 2013).

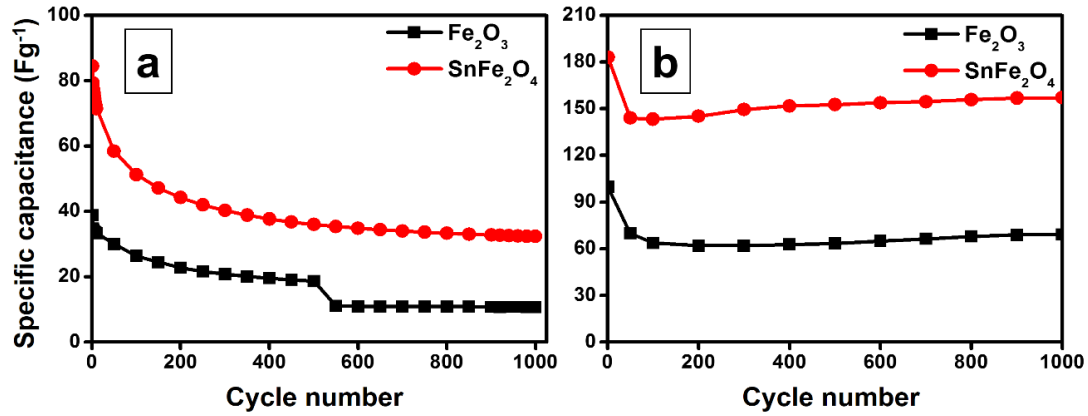

Fig. 5.10. Cycle life of electrodes prepared using Fe_2O_3 nanorods and $SnFe_2O_4$ microcubes at scan rates of (a) 50 mVs^{-1} and (b) 20 mVs^{-1} for 1000 cycles.

5.1.7 α-Fe_2O_3 nanorods and $SnFe_2O_4$ microcubes based chronopotentiometric hydrogen peroxide sensor

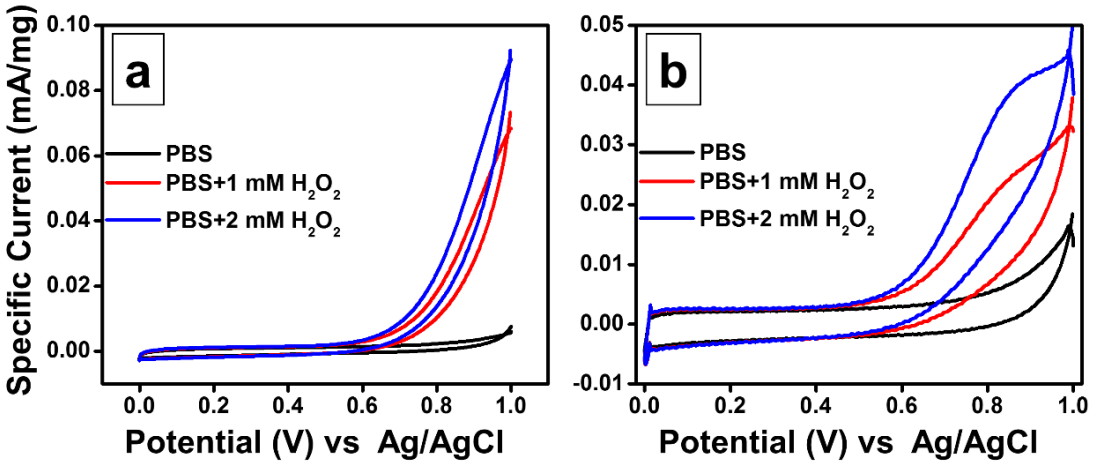

Figure 5.11 Cyclic voltammograms of (a) Fe_2O_3/GCE and (b) $SnFe_2O_4$/GCE at different concentrations of H_2O_2 in 0.1 M PBS (pH=7) recorded at a scan rate of 50 mVs^{-1}.

The electrochemical H_2O_2 sensing performances of Fe_2O_3 and $SnFe_2O_4$ were studied through cyclic voltammetry and chronopotentiometry using a three-electrode system with modified GCE in a 0.1 M PBS (pH=7) electrolyte. Figure 5.11 shows the CV of Fe_2O_3/GCE and $SnFe_2O_4$/GCE at different concentrations of H_2O_2 in 0.1 M PBS

at a scan rate of 50mVs^{-1}. The increase in the oxidation current with an increase in concentration of H_2O_2 in the PBS can be noted from Figure 5.11. This indicates that, the modified GCE shows good performance towards H_2O_2 sensing. Herein, the sensing mechanism of Fe_2O_3/GCE can be explained on the basis of electro-catalysis reaction (Ding et al. 2015, Li et al. 2015). The slow generation of $OH^{\bullet}$ (hydroxyl radicals) from H_2O_2 catalyzed by iron is according to the Haber-Weiss mechanism, while the oxidation of Fe^{2+} to Fe^{3+} involves the Fenton reaction as shown below,

$$Fe^{2+} + H_2O_2 \rightarrow Fe^{3+} + OH^- + OH^{\cdot} \ldots\ldots\ldots\ldots (39)$$

$$H_2O_2 + {}^{\cdot}OH \rightarrow H_2O + {}^{\cdot}OOH \ldots\ldots\ldots\ldots (40)$$

$$Fe^{3+} + {}^{\cdot}OOH \rightarrow Fe^{2+} + H^+ + O_2 \ldots\ldots\ldots\ldots (41)$$

On the other hand, in case of stannous ferrite the reduction of H_2O_2 using Sn^{2+} ions results in Sn^{4+} ion formation. The equations for the catalytic reduction of H_2O_2 using $SnFe_2O_4$ can written as follows,

$$Sn^{2+} + 2H_2O_2 \rightarrow Sn^{4+} + 2OH^- + 2OH^{\cdot} \ldots\ldots\ldots\ldots (42)$$

$$H_2O_2 + {}^{\cdot}OH \rightarrow H_2O + {}^{\cdot}OOH \ldots\ldots\ldots\ldots (43)$$

$$Sn^{4+} + 2({}^{\cdot}OOH) \rightarrow Sn^{2+} + 2H^+ + 2O_2 \ldots\ldots\ldots\ldots (44)$$

It should be noted that the reduction/oxidation potential required for Fe^{3+}/Fe^{2+} is 0.77 V while it is just 0.15 V for Sn^{4+}/Sn^{2+}, indicating that the oxidation of Sn^{2+} to Sn^{4+} is much more favorable than that of Fe^{2+} to Fe^{3+} (Jaime-González et al. 2016, Wiberg et al.). Therefore, the catalytic reduction of H_2O_2 occurs more favorably using $SnFe_2O_4$ than in Fe_2O_3. On the other hand, the crystal phase and morphology can also influence the sensing ability of the material (Babu et al. 2014). Herein, the micro-cube like morphology of the $SnFe_2O_4$ can also be expected to increase its sensing performance.

The chronopotentiometric curves of Fe_2O_3/GCE and $SnFe_2O_4$/GCE recorded at 4 μA for successive additions of 0.1 M H_2O_2 at regular intervals in 0.1 M PBS is shown

in Figure 5.12. Each addition of H_2O_2 resulted in a decrease in the potential and reaches a steady state. The fast response of the sensor implies that Fe_2O_3 and $SnFe_2O_4$ efficiently promote the reduction of H_2O_2. Both Fe_2O_3/GCE and $SnFe_2O_4$/GCE show a good electrochemical response to a wide range of H_2O_2 concentration and the plots corresponding to higher concentrations are presented in the insets of Figure 5.12(a) and 5.12(c). The sensitivity of Fe_2O_3/GCE and $SnFe_2O_4$/GCE at higher concentration range of 0.1-2.5 mM H_2O_2 is found to be 72.25 and 95.42 mV/decade, respectively.

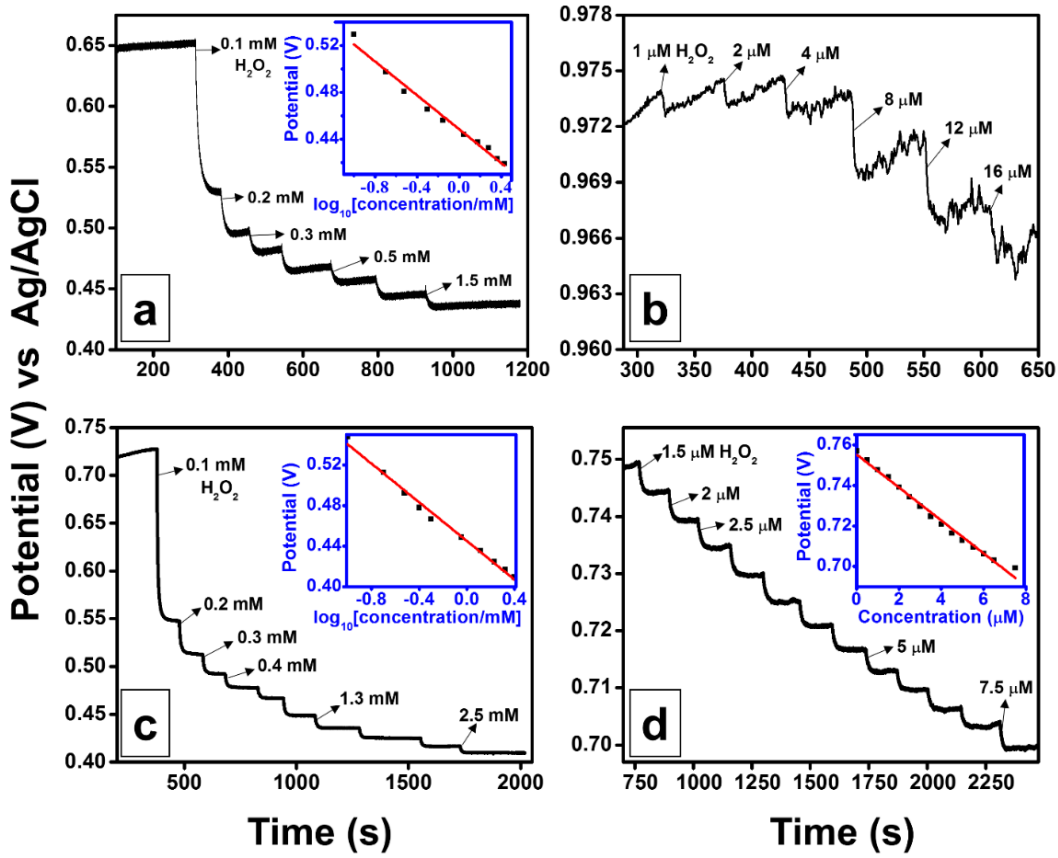

Figure 5.12 Chronopotentiometric curves representing the H_2O_2 sensing performances of Fe_2O_3/GCE (a, b) and $SnFe_2O_4$/GCE (c, d). The calibration curves are shown in the insets.

The chronopotentiometric curves of Fe_2O_3/GCE and $SnFe_2O_4$/GCE sensors for H_2O_2 in micro-molar concentration range are shown in Figure 5.12(b) and 5.12(d). The plots clearly indicate that $SnFe_2O_4$ based sensor has better signal-to-noise ratio (S/N) in comparison to Fe_2O_3. Owing to the good S/N in $SnFe_2O_4$, the sensitivity at lower concentration range of H_2O_2 is calculated to be 2.7 $mV\mu M^{-1}\mu g^{-1}$. However, the poor

S/N ratio in Fe_2O_3 hinders the calculation of the sensitivity at lower concentration range of H_2O_2. The lower limit of detection of Fe_2O_3/GCE sensor is calculated to be 0.34 μM and surprisingly a significant lower value of 41 nM (0.041 μM) with S/N=3 was obtained for $SnFe_2O_4$/GCE. The high performance and less noise in $SnFe_2O_4$/GCE can be attributed to its unique morphology, large surface area, higher pore volume and the reduction in the material resistance compared to Fe_2O_3/GCE. The linear concentration range (dynamic linear range) and lower detection limit of different oxide materials used for non-enzymatic detection of H_2O_2 with an S/N of 3 are shown in Table 5.4. As observed from Table 5.4, it is worthy to note that the values obtained for the modified GCE in the present work are better than those reported in literature. Furthermore, it is important to note that the lowest limit of H_2O_2 detection (41 nM) observed herein was obtained using indigenous electrodes fabricated with pristine $SnFe_2O4$ microcubes, without combining it with graphene or its analogues. This indicates that pristine $SnFe_2O_4$ microcubes are excellent electrode materials for electrochemical applications.

Table 5.4. Linear rage and detection limit of hydrogen peroxide sensors based on different materials found in literature.

Working electrode	Method of detection*	Linear range	Limit of detection	References
$CoFe_2O_4$–chitosan nanocomposite	CA	3×10^{-2} to 8 mM	2×10^{-3} mM	(Yardımcı et al. 2012)
Pt–SnO_2@C nanospheres	CA	1–170 μM	0.1 μM	(Lu et al. 2013)
Ag/SnO_2 nanotubes	CA	0.01 to 35.0 mM	5.0 μM	(Miao et al. 2013)
Vertical NiO nanosheets	CA	up to 4.0 mM	0.4l μM	(Liu et al. 2015)
Fe_3O_4/PPy/Ag nanocomposites	CA	5 l M to 11.5 mM	1.7 μM	(Qi et al. 2015)
Pt–MnO_x	CA	2 mM to 4.0 mM	0.7 mM	(Kivrak et al. 2015)
MnO_2-Ag@C	CA	0.5 μM to5.7 mM	0.17 μM	(Zhang and Zheng 2016)
CuO@Cu_2O–NWs/PVA	CA	1–3000 & 3000–10,000 μM	0.35 μM	(Zhang and Zheng 2016)
SnO_2-rGO composite	CA	0.5 to 800 μM	0.478 μM	(Zhang, Li, et al. 2016)
Fe_2O_3 nanorods **	CP	0.1 to 2.7 mM	0.34 μM	Present work
$SnFe_2O_4$ microcubes**	CP	0.005 to 2 mM	0.041 μM	-
Fe_3O_4 ***	CA	0 to 3.2 mM	94 μM	-

$NiFe_2O_4$***	CA	0 to 3 mM	23 μM	-
$ZnFe_2O_4$***	CA	0 to 2.5 mM	3 μM	-
$SnFe_2O_4$***	CA	0 to 2.5 mM	2.6 μM	-

*CA-Chronoamperometry, CP-Chronopotentiometry, ** microwave assisted synthesis, *** hydrothermally prepared

5.2 $SnFe_2O_4$@rGO/MWCNT nanocomposite based dopamine sensor and anode material of LIB

5.2.1 Preparation of GO

To prepare graphene oxide solution, 1:1 ratio of graphite flakes and $NaNO_3$ were added into 46 mL of concentrated H_2SO_4 in an ice bath for about half an hour. Then, 9 g of potassium permanganate was added slowly into the above mixture. The reaction mixture was stirred continuously at room temperature till it becomes a thick paste. 46 ml of water was added slowly to the mixture and stirred well for 30 min, and 150 ml of H_2O_2 solution was added into it. The thick GO solution was separated from the water using separating funnel, and washed thoroughly with 3% HCl and distilled water repeatedly, until the pH of the solution to be neutral. The concentration of the final GO solution estimated to be 1.627 mg-ml^{-1}.

5.2.2 Preparation of $SnFe_2O_4$@rGO/MWCNT nanocomposite

1:1 ratio of GO and MWCNT were dispersed in 40 ml of water, 0.06789 g of $SnCl_2$ and 0.1 ml of N_2H_4 H_2O was added to the GO solution and stirred for 30 min. The reaction mixture was transferred to a Teflon jar and hydrothermally treated for 24 hrs at 180 °C. The precipitate was separated from the solution by centrifugation and washed repeatedly with ethanol, water and acetone. The washed precipitate was dried at 60 °C overnight in a vacuum oven.

5.2.3 X-ray diffraction

Figure 5.13 shows XRD pattern of $SnFe_2O_4$@rGO/MWCNT nanocomposite. XRD peaks of $SnFe_2O_4$@rGO/MWCNT nanocomposite matches well with the inverse spinel structured stannous ferrite (JCPDS # 01-071-0693). A broad peak at around 20 to 30° in the composites can be attributed to the reduction of graphene oxides on hydrothermal treatment. A peak at around 27° in $SnFe_2O_4$@rGO/MWCNT pattern belongs to the MWCNT.

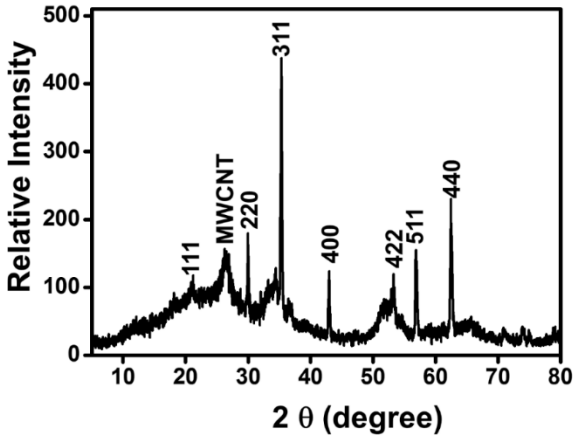

Figure 5.13 XRD patterns of $SnFe_2O_4$@rGO/MWCNT nanocomposite.

5.2.4 Transmission electron microscopy

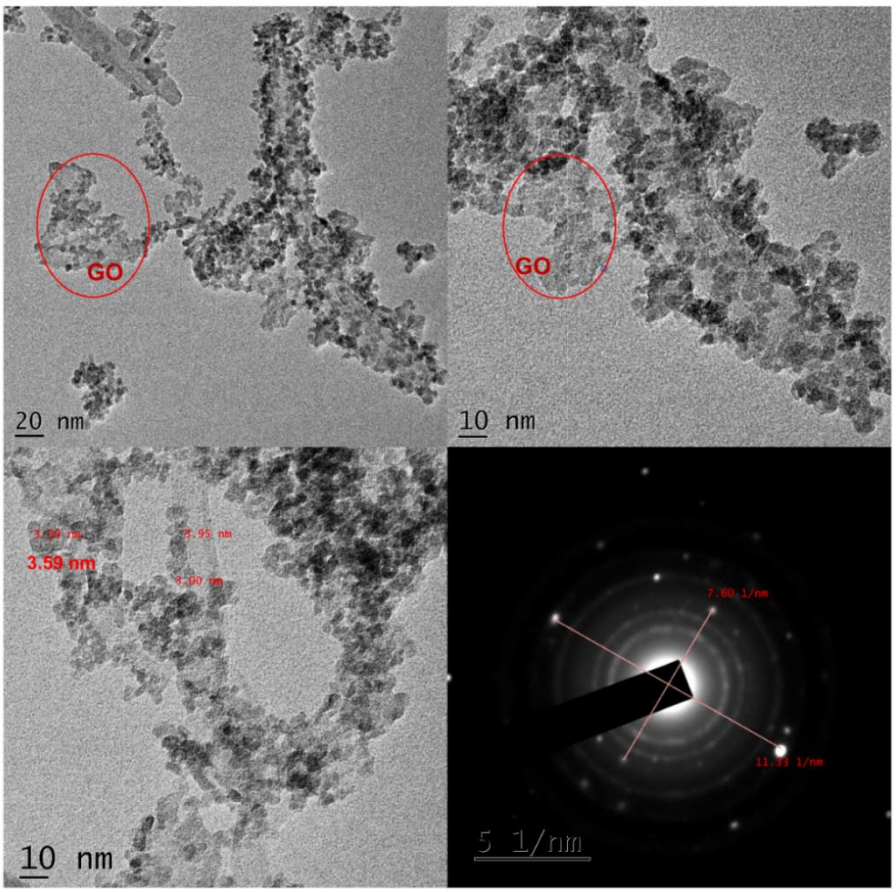

Figure 5.14 (a,b)TEM, (c) HRTEM and (d) SAED pattern of $SnFe_2O_4$@rGO/MWCNT nanocomposite.

Figure 5.14 shows TEM images of $SnFe_2O_4$@rGO/MWCNT nanocomposite, in which $SnFe_2O_4$ nanoparticles of 3.5 nm size, are decorated on the GO nano sheets and MWCNT. SEAD pattern of $SnFe_2O_4$@rGO/MWCNT nanocomposite aligned in [620] direction with diffused rings, which is because of the small sized nanoparticles and short range order.

5.2.5 Amperometric dopamine sensors

5.2.5.1 $SnFe_2O_4$@rGO/MWCNT nanocomposite based chronoamperometric dopamine sensor

$SnFe_2O_4$@rGO/MWCNT modified GCE was tested as dopamine sensor using three-electrode system in 0.1 M PBS solution against Ag/AgCl as reference electrode. Figure 5.15 shows the cyclic voltammograms of $SnFe_2O_4$@rGO/MWCNT modified GCE in the presence of different concentration of dopamine. We can observe an oxidation peak at 0.2 V and it increases with the increase in dopamine concentration.

When the potential is applied to the modified electrode, dopamine quinone is formed by the oxidation of dopamine molecules with exchange of two electron and protons (Lv et al. 2015). The oxidation and reduction of dopamine takes place at a potential of 0.2 V and 0.1 V respectively. The mechanism can be represented as,

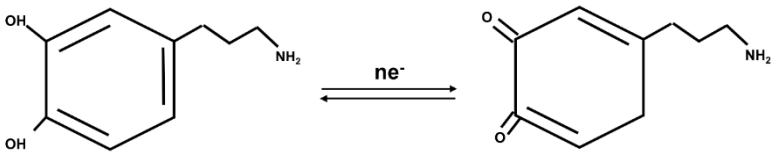

Cyclic-voltammograms of $SnFe_2O_4$@rGO/MWCNT in the presence of 100 μM of dopamine at different scan rates are shown in Figure 5.15(b). Anodic and cathodic currents increase with an increase in the scan rate, which indicates the mass transport mechanism in the system. The peak current versus scan rate have a linear relation, which indicates that the electrochemical behaviour of dopamine on the composite is an adsorption controlled reaction. The shift in the peak current with an increase in the scan rate indicates the quasi-reversible nature of the reaction (Cui et al. 2017).

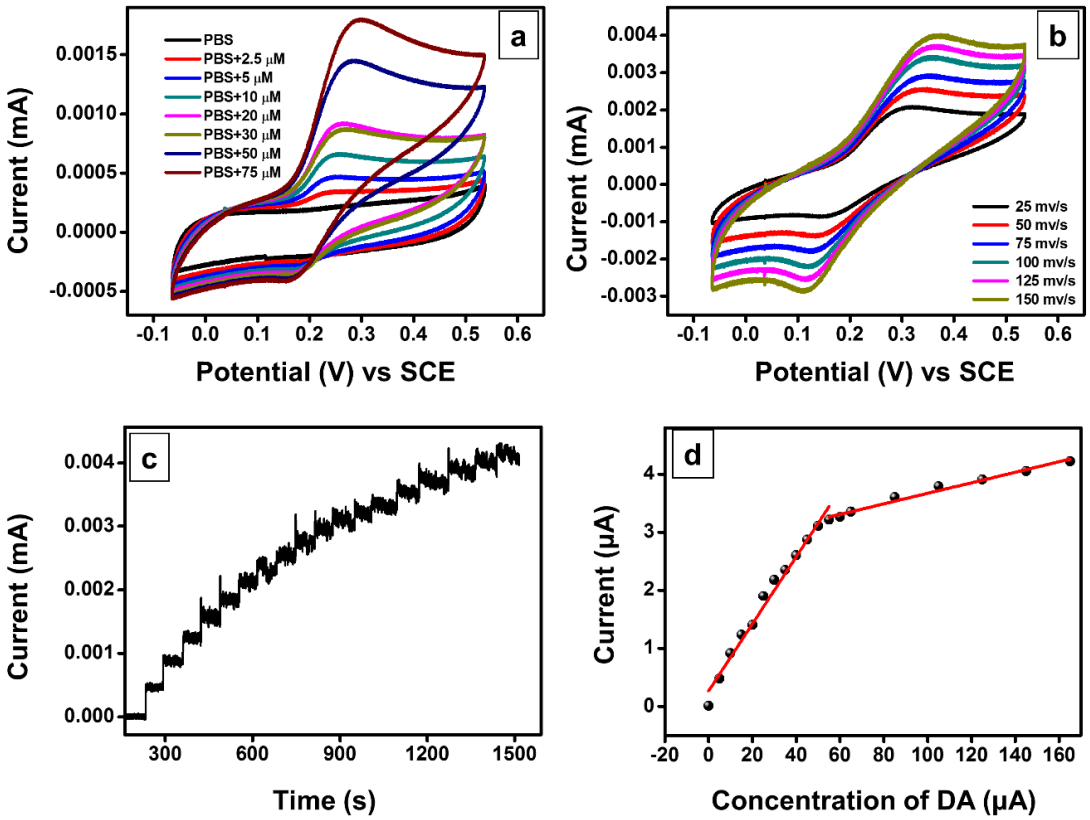

Figure 5.15 (a) CV curves of $SnFe_2O_4$@rGO/MWCNT with different concentration of Dopamine, (b) CV curves of $SnFe_2O_4$ in the presence of 100 μM dopamine at different scan rates, (c) Chronoamperometric curve of $SnFe_2O_4$@rGO/MWCNT with addition of dopamine and (d) Current and concentration of dopamine calibration curve of $SnFe_2O_4$@rGO/MWCNT for the chronoamperometric curve.

The chronoamperometric curve of $SnFe_2O_4$@rGO/MWCNT recorded by applying 0.2 V of constant potential, with successive addition of 10 mM of dopamine at different time intervals is shown in Figure 5.15(c). On each addition of dopamine, current increases immediately, this fast response of the sensor indicates the efficient oxidation of dopamine. From the chronoamperometric curves, we can observe that the composite shows very good performance towards the sensing of dopamine (Jaime-González et al. 2016, Wolfenstine et al. 2005). Current and concentration of dopamine calibration curve is given in Figure 5.15(d). Oxidation current of $SnFe_2O_4$@rGO/MWCNT has linear relationship with concentration of dopamine at two region i.e., 0 to 55μM and 55 to 165 μM. The specific sensitivity of

$SnFe_2O_4$@rGO/MWCNT in the concentration range of 0-55 μM and 55-165 μM are 0.129 $\mu A \mu M^{-1} \mu g^{-1}$ and 0.01443 $\mu A \mu M^{-1} \mu g^{-1}$ respectively. The lowest limit of detection is 12 nM with signal to noise ratio of 3.

In $SnFe_2O_4$@rGO/MW, redox couple of $SnFe_2O_4$ is involved in the redox reaction. Also, the reduced graphene nano-sheets and MWCNT provide an extra area to accommodate the dopamine molecule to react with $SnFe_2O_4$ nanoparticles, which is involved in the redox reaction. Composites modified GCEs exhibit a faster response towards the dopamine, this is because of the attraction of positive amino chains due to the synergetic effect of interaction between $SnFe_2O_4$ and graphene/ MWCNT. Both graphene and MWCNT provide large effective surface area and help for the easy electron transfer between the electrode and dopamine. The л-л interactions in both graphene sheets and MWCNT also help in the interaction between the electrode and dopamine (Vulcu et al. 2018).

5.2.6 $SnFe_2O_4$@rGO/MWCNT based anode material for LIB

The electrochemical performance of $SnFe_2O_4$@rGO/MWCNT nanocomposite as anode material of a LIB was studied using Galvanostatic charge-discharge at a current density of 50 mAg^{-1}. Figure 5.16(a) represents the GCD profiles of $SnFe_2O_4$@rGO-MWCNT at 1st, 2nd and 10th cycles. From the discharge profile we can observe that the voltage drops 1.5 V from open circuit voltage in the first discharge cycle, during which the insertion of Li^+ ions begins. First discharge curve consists of voltage plateau at around 1.3 V and 0.7 V. After 0.5 V, the voltage drop is gentle. The first discharging and charging capacities of the composite are 1822 and 1998 $mAhg^{-1}$ respectively, resulting in an initial coulombic efficiency of 91.19%. The capacity loss of this initial discharge charge cycle can be attributed to the formation of solid electrolyte interface (SEI) layer on the surface of the electrode and the reaction of lithium ions with the residual oxygen-containing functional group. Due to these processes, the specific discharge charge capacities of the composite greatly reduce in the subsequent discharge -charge cycles, as shown in Fig 5.16(a) and 5.16(b). The coulombic efficiency reduced to 84% for the second cycle. It further increased to 91 % for the 10th cycle and 96% for the 250th cycle, which indicates the improved reversibility

of the electrode reaction. The composite can deliver a discharge capacity of 1997, 1600, 200 and 100 mAh-g^{-1} at current density of 10, 50, 100 and 200 mA/g respectively. It recovers 92% of capacity at 10 mAg^{-1} current density after running at higher current densities as shown in Figure 5.16(c). Compared to the theoretical capacity of $SnFe_2O_4$, and some other ferrites, the reversible capacity of the composite presented in this work is much higher, which suggest the superiority of the composite as anode material for lithium ion batteries.

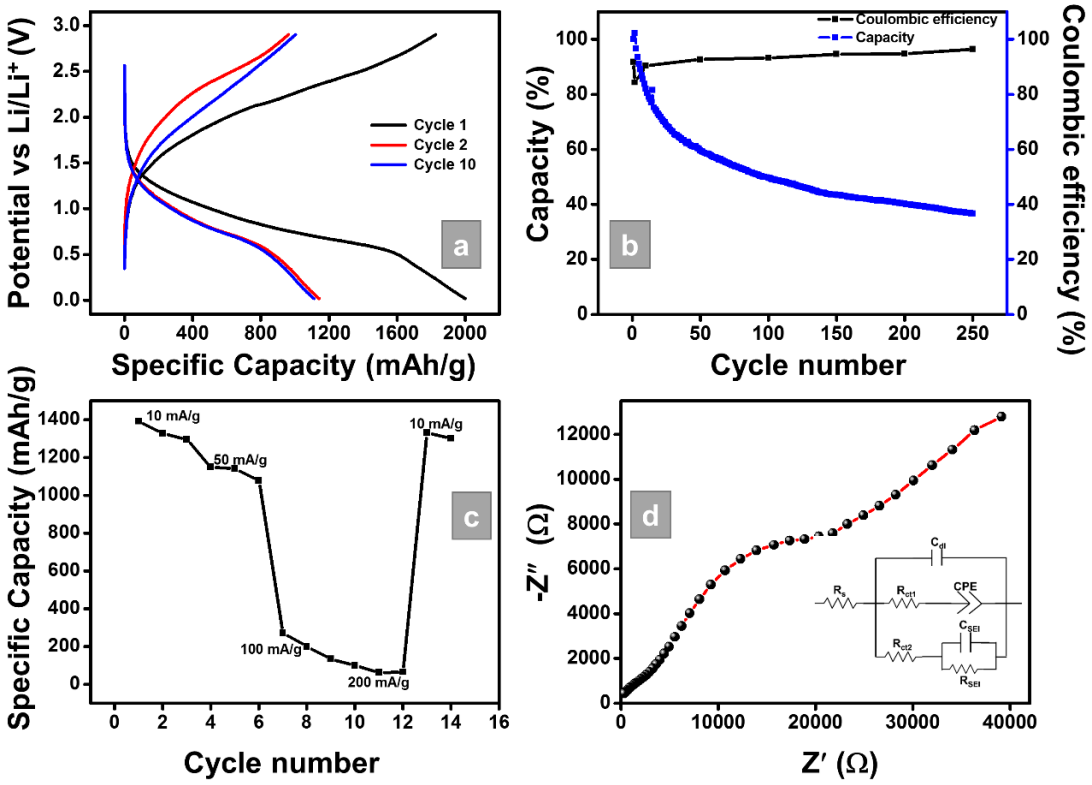

Figure 5.16 (a) The charge/discharge voltage profiles of $SnFe_2O_4$@rGO/MWCNT composite for first, second and tenth cycle at 50 mAg^{-1} current density. (b) Cycling performance of $SnFe_2O_4$@rGO/MWCNT at 100 mAg^{-1} current density for 250 cycles. (c) Rate capabilities of $SnFe_2O_4$@rGO/MWCNT composite at different current densities (10, 50, 100, 200 and 10 mAg^{-1}). (d) Nyquist plot and equivalent circuit of $SnFe_2O_4$@rGO/MWCNT composite.

Figure 5.16(d) shows the electrochemical impedance spectra of the composite. It has a broad depressed semicircle at lower frequency and a straight line at higher frequency region. The charge transfer resistance extracted from the equivalent circuit

is 325Ω. The straight line in the EIS represents the impedance response that is controlled by the mass transfer mechanism, such as diffusion of lithium ion into the electrodes.

5.3 Summary

- In summary, a simple microwave assisted reaction approach was employed for the synthesis of $SnFe_2O_4$ microcubes and Fe_2O_3 nanorods, for applications in electrode materials for supercapacitor and sensor applications.
- Formation of $SnFe_2O_4$ microcubes is the key factor for the enhanced performance of supercapacitor and sensor.
- The specific capacitance of the supercapacitor using $SnFe_2O_4$ electrode (172 Fg^{-1}) was almost three times higher in comparison to Fe_2O_3 (70 Fg^{-1}) in 1 M KOH at a scan rate of 5 mVs^{-1}.
- The sensitivities at higher concentrations (mM) of H_2O_2 using Fe_2O_3/GCE and $SnFe_2O_4$/GCE were 72.25 mV/decade and 95.42 mV/decade, respectively, while at lower concentration range (μM) only $SnFe_2O_4$/GCE exhibited good sensitivity with better signal-to-noise ratio. The calculated LOD of Fe_2O_3/GCE and $SnFe_2O_4$/GCE of H_2O_2 are 0.3 μM and 41 nM respectively, with the S/N ratio of 3.
- The excellent electrochemical performance of $SnFe_2O_4$ microcubes is attributed to factors such as its unique morphology, large surface area and higher pore volume, suggesting its suitability as a promising electrode material for applications, such as supercapacitors, electrochemical sensors, Li-ion batteries and electrocatalysis.
- $SnFe_2O_4$@rGO/MWCNT nanocomposite was successfully prepared by hydrothermal method, in which $SnFe_2O_4$ nanoparticles are decorated on rGO nanosheets and multi walled carbon nanotubes.
- Chronoamperometric dopamine sensor of $SnFe_2O_4$@rGO/MWCNT nanocomposite shows the good performance of with a specific sensitivity of 0.129 $\mu A \mu M^{-1} \mu g^{-1}$ at a linear range of 0-55 μM, with a LOD of 12 nM (S/N=3).

- The electrochemical performance of $SnFe_2O_4$@rGO/MWCNT nanocomposite as anode material of LIB was tested using GCD. It reveals 1822 and 1998 $mAhg^{-1}$ of charge and discharge capacities respectively, with a coulombic efficiency of 96% in the first cycle. It retains 40 % of discharge capacity of its initial cycle and 91% coulombic efficiency at the 250^{th} cycle.

CHAPTER 6

Conclusion and Future Direction

From the studies, we can conclude that,

- Both microwave assisted and hydrothermal methods can be employed for the preparation of ferrite nanoparticles with desired properties. The preparation method influences the structure, composition, and morphology of ferrites.
- Both, nickel doping and annealing temperatures, effect the crystal structure of iron oxides. Nickel doped samples annealed at 450 °C have mixed phase of hematite and magnetite. While samples annealed at 600 °C have pure hematite phase. Nickel doping influences the electrical and magnetic properties of ferrites. The samples annealed at 450 °C have higher AC conductivity and dielectric constant than that of the samples annealed at 600 °C. Nickel doped ferrites show ferromagnetic behaviour and the saturation magnetization increases with increase in the nickel concentration.
- Tin doped hematite samples have nanoplates like morphology. The AC conductivity and dielectric constant of α-$Sn_xFe_{2-x}O_3$ nanoplates decreases with the increase in tin concentration till 4 wt% of Sn and increases with further doping. α-$Sn_xFe_{2-x}O_3$ nanoplates shows antiferromagnetic behaviour with very high coercivity.
- The cations and cationic position in a spinel ferrite defines the electrical properties of the ferrite. The normal spine structured ferrites have higher AC conductivity and dielectric constant than that of inverse spinel structured ferrites.
- Chronoamperometric H_2O_2 sensors based on MFe_2O_4 nanoparticles showed high sensing performance. $ZnFe_2O_4$ and $SnFe_2O_4$ have better performance towards the sensing of H_2O_2 with a specific sensitivity of 4.411 $\mu AmM^{-1}\mu g^{-1}$ and 3.915 $\mu AmM^{-1}\mu g^{-1}$, respectively. In addition, $SnFe_2O_4$ has the lowest limit of detection, long dynamical range and good selectivity, along with good specific sensitivity.

- Tin ferrite ($SnFe_2O_4$) microcubes show a high electrochemical performance than Fe_2O_3 nanorods prepared using microwave assisted method. As a supercapacitor electrode, $SnFe_2O_4$ has a high specific capacitance of 106 Fg^{-1} in 1 M KOH. It revealed a high electrocatalytic activity towards the sensing of H_2O_2 with specific sensitivity 2.7 $mV\mu M^{-1}\mu g^{-1}$ at lower concentration range of H_2O_2 with a lowest limit of detection 41 nM.
- Tin ferrite have a high electrochemical activity because of Sn redox couple. In the last chapter, $SnFe_2O_4$@rGO-MWCNT composite prepared using hydrothermal method shows a specific sensitivity of 0.129 $\mu A\mu M^{-1}\mu g^{-1}$ at a linear range of 0-55 μM of dopamine concentration, with a LOD of 12 nM (S/N=3). Also, it exhibits a high discharge and charge capacity of 1998 and 1822 $mAh\text{-}g^{-1}$ respectively at the first cycle as anode material of LIB. It has 91% of coulombic efficiency and 40% of capacity retention after 250 cycle. Tin ferrite and its composites of carbon nanomaterials can be promising materials in electrochemical applications.

Future direction

The studies show that, doping of tin into the iron oxide structure enhances its electrochemical properties. The lattice positions occupied by the Sn ion in the structure is also important for this high electrocatalytic activity. In the future work, the site occupation tendency of Sn in iron oxide needs to be studied using XPS and Mossbauer spectroscopy.

The electrochemical activity can also be improved by the incorporation of different carbonaceous material like, activated carbon, graphene, carbon nanotubes and conducting polymers. Tin has a high specific capacity as anode material of LIB but the cyclic stability is poor. Doping of tin in different spinel ferrite like $MnFe_2O_4$, $CoFe_2O_4$, etc., which have high cyclic stability can improve the overall performance of a LIB.

References

A. K, Sijo, Dimple P. Dutta, M. Roy, and Sudheesh V.D. 2017. "Magnetic and dielectric properties of NiCrFeO4 prepared by solution self combustion method." *Materials Research Bulletin* 94:154-159. doi: https://doi.org/10.1016/j.materresbull.2017.05.062.

A.K, Sijo, Dimple P. Dutta, and M. Roy. 2017. "Dielectric properties of CoCrFeO4 nano-powder prepared by solution self combustion synthesis." *Ceramics International* 43 (18):16915-16918. doi: https://doi.org/10.1016/j.ceramint.2017.09.093.

Abo, Masahiro, Yasuteru Urano, Kenjiro Hanaoka, Takuya Terai, Toru Komatsu, and Tetsuo Nagano. 2011. "Development of a Highly Sensitive Fluorescence Probe for Hydrogen Peroxide." *Journal of the American Chemical Society* 133 (27):10629-10637. doi: 10.1021/ja203521e.

Agami, W. R. 2018. "Effect of neodymium substitution on the electric and dielectric properties of Mn-Ni-Zn ferrite." *Physica B: Condensed Matter* 534:17-21. doi: https://doi.org/10.1016/j.physb.2018.01.021.

Ajmal, Muhammad, M. U. Islam, Ghulam Abbas Ashraf, Muhammad Aamir Nazir, and M. I. Ghouri. 2017. "The influence of Ga doping on structural magnetic and dielectric properties of NiCr0.2Fe1.8O4 spinel ferrite." *Physica B: Condensed Matter* 526:149-154. doi: https://doi.org/10.1016/j.physb.2017.05.044.

Ali, Irshad, M. U. Islam, Muhammad Naeem Ashiq, M. Asif Iqbal, Hasan M. Khan, and Nazia Karamat. 2013. "Effect of Tb–Mn substitution on DC and AC conductivity of Y-type hexagonal ferrite." *Journal of Alloys and Compounds* 579:576-582. doi: http://dx.doi.org/10.1016/j.jallcom.2013.06.182.

Ali, Rajjab, Muhammad Azhar Khan, Alina Manzoor, Muhammad Shahid, Sajjad Haider, Abdul Sattar Malik, Muhammad Sher, Imran Shakir, and Muhammad Farooq Warsi. 2017. "Investigation of structural and magnetic properties of Zr-Co doped nickel ferrite nanomaterials." *Journal of Magnetism and Magnetic Materials* 429:142-147. doi: https://doi.org/10.1016/j.jmmm.2017.01.007.

Aparna, M. L., A. Nirmala Grace, P. Sathyanarayanan, and Niroj Kumar Sahu. 2018. "A comparative study on the supercapacitive behaviour of solvothermally prepared metal ferrite (MFe2O4, M = Fe, Co, Ni, Mn, Cu, Zn) nanoassemblies." *Journal of Alloys and Compounds* 745:385-395. doi: https://doi.org/10.1016/j.jallcom.2018.02.127.

Ashwini, L. S., R. Sridhar, and S. S. Bellad. 2017. "Dielectric and magnetoelectric properties of Li-Mg ferrite: Barium titanate composites." *Materials Chemistry and Physics* 200:136-145. doi: http://dx.doi.org/10.1016/j.matchemphys.2017.07.048.

Assar, S. T., H. F. Abosheiasha, and M. K. El Nimr. 2014. "Study of the dielectric behavior of Co–Ni–Li nanoferrites." *Journal of Magnetism and Magnetic Materials* 350:12-18. doi: http://dx.doi.org/10.1016/j.jmmm.2013.09.022.

Atif, M., M. W. Asghar, M. Nadeem, W. Khalid, Z. Ali, and S. Badshah. 2018. "Synthesis and investigation of structural, magnetic and dielectric properties

of zinc substituted cobalt ferrites." *Journal of Physics and Chemistry of Solids* 123:36-42. doi: https://doi.org/10.1016/j.jpcs.2018.07.010.

Atif, M., R. Sato Turtelli, R. Grössinger, M. Siddique, and M. Nadeem. 2014. "Effect of Mn substitution on the cation distribution and temperature dependence of magnetic anisotropy constant in Co1−xMnxFe2O4 (0.0≤x≤0.4) ferrites." *Ceramics International* 40 (1, Part A):471-478. doi: https://doi.org/10.1016/j.ceramint.2013.06.026.

Auwal, I. A., H. Erdemi, H. Sözeri, H. Güngüneş, and A. Baykal. 2016. "Magnetic and dielectric properties of Bi3+ substituted SrFe12O19 hexaferrite." *Journal of Magnetism and Magnetic Materials* 412:69-82. doi: https://doi.org/10.1016/j.jmmm.2016.03.066.

Babu, K. Justice, Awan Zahoor, Kee Suk Nahm, R. Ramachandran, M. A. Jothi Rajan, and G. Gnana kumar. 2014. "The influences of shape and structure of MnO2 nanomaterials over the non-enzymatic sensing ability of hydrogen peroxide." *Journal of Nanoparticle Research* 16 (2):1-10. doi: 10.1007/s11051-014-2250-4.

Babu, K. Vijaya, G. V. Santosh Kumar, K. Jalaiah, and Paulos Teddesse Shibeshi. 2018. "Effects of copper substitution on the microstructural, electrical and magnetic properties of Ni0.7Co0.3-xCuxFe2O4 ferrites." *Journal of Physics and Chemistry of Solids* 118:172-185. doi: https://doi.org/10.1016/j.jpcs.2018.02.051.

Babu, K. Vijaya, B. Sailaja, K. Jalaiah, Paulos Taddesse Shibeshi, and M. Ravi. 2018. "Effect of zinc substitution on the structural, electrical and magnetic properties of nano-structured Ni0.5Co0.5Fe2O4 ferrites." *Physica B: Condensed Matter* 534:83-89. doi: https://doi.org/10.1016/j.physb.2018.01.022.

Batoo, Khalid Mujasam, Shalendra Kumar, Chan Gyu Lee, and Alimuddin. 2009. "Study of dielectric and ac impedance properties of Ti doped Mn ferrites." *Current Applied Physics* 9 (6):1397-1406. doi: https://doi.org/10.1016/j.cap.2009.03.012.

Besser, P. J., A. H. Morrish, and C. W. Searle. 1967. "Magnetocrystalline Anisotropy of Pure and Doped Hematite." *Physical Review* 153 (2):632-640. doi: 10.1103/PhysRev.153.632.

Bhujun, Bhamini, Michelle T. T. Tan, and Anandan S. Shanmugam. 2017. "Study of mixed ternary transition metal ferrites as potential electrodes for supercapacitor applications." *Results in Physics* 7:345-353. doi: https://doi.org/10.1016/j.rinp.2016.04.010.

Bindu, K., K. M. Ajith, and H. S. Nagaraja. 2018. "Electrical, dielectric and magnetic properties of Sn-doped hematite (α-SnxFe2-xO3) nanoplates synthesized by microwave-assisted method." *Journal of Alloys and Compounds* 735:847-854. doi: https://doi.org/10.1016/j.jallcom.2017.11.180.

Boda, Sunil Kumar, Anupama A. V, Bikramjit Basu, and Balaram Sahoo. 2015. "Structural and Magnetic Phase Transformations of Hydroxyapatite-Magnetite Composites under Inert and Ambient Sintering Atmospheres." *The Journal of Physical Chemistry C* 119 (12):6539-6555. doi: 10.1021/jp5114027.

Bødker, Franz, and S. Mørup. 2000. *Size dependence of the properties of hematite nanoparticles*. Vol. 52.

Chakrabarti, S., S. K. Mandal, and S. Chaudhuri. 2005. "Cobalt doped γ - Fe 2 O 3 nanoparticles: synthesis and magnetic properties." *Nanotechnology* 16 (4):506.

Chakradhary, Vishal K., Azizurrahaman Ansari, and M. Jaleel Akhtar. 2019. "Design, synthesis, and testing of high coercivity cobalt doped nickel ferrite nanoparticles for magnetic applications." *Journal of Magnetism and Magnetic Materials* 469:674-680. doi: https://doi.org/10.1016/j.jmmm.2018.09.021.

Chella, Santhosh, Pratap Kollu, Eswara Vara P. R. Komarala, Sejal Doshi, Murugan Saranya, Sathiyanathan Felix, Rajendran Ramachandran, Padmanapan Saravanan, Vijaya Lakshmi Koneru, Velmurugan Venugopal, Soon Kwan Jeong, and Andrews Nirmala Grace. 2015. "Solvothermal synthesis of MnFe2O4-graphene composite—Investigation of its adsorption and antimicrobial properties." *Applied Surface Science* 327:27-36. doi: https://doi.org/10.1016/j.apsusc.2014.11.096.

Chen, Jie, Daming Zhao, Zhidan Diao, Miao Wang, and Shaohua Shen. 2016. "Ferrites boosting photocatalytic hydrogen evolution over graphitic carbon nitride: a case study of (Co, Ni)Fe2O4 modification." *Science Bulletin* 61 (4):292-301. doi: https://doi.org/10.1007/s11434-016-0995-0.

Chen, Kunfeng, Shuyan Song, and Dongfeng Xue. 2015. "Faceted Cu2O structures with enhanced Li-ion battery anode performances." *CrystEngComm* 17 (10):2110-2117. doi: 10.1039/C4CE02340D.

Chen, Wei, Shu Cai, Qiong-Qiong Ren, Wei Wen, and Yuan-Di Zhao. 2012. "Recent advances in electrochemical sensing for hydrogen peroxide: a review." *Analyst* 137 (1):49-58. doi: 10.1039/c1an15738h.

Chen, Xiang Ying, Chong Chen, Zhong Jie Zhang, Dong Hua Xie, Xiao Deng, and Jian Wei Liu. 2013. "Nitrogen-doped porous carbon for supercapacitor with long-term electrochemical stability." *Journal of Power Sources* 230:50-58. doi: http://dx.doi.org/10.1016/j.jpowsour.2012.12.054.

Choi, Sun Hee, Joo Sun Kim, and Young Soo Yoon. 2004. "Fabrication and characterization of SnO2–RuO2 composite anode thin film for lithium ion batteries." *Electrochimica Acta* 50 (2):547-552. doi: https://doi.org/10.1016/j.electacta.2004.02.066.

Coey, J. M. D. 1988. "Magnetic Properties of Iron in Soil Iron Oxides and Clay Minerals." In *Iron in Soils and Clay Minerals*, edited by J. W. Stucki, B. A. Goodman and U. Schwertmann, 397-466. Dordrecht: Springer Netherlands.

Cornell, R.M., and U. Scwertmann. 2003. "Electronic, Electrical and Magnetic Properties and Colour." In *The Iron Oxides: Structure, Properties, Reactions, Occurence and uses*. Weinheim: WILEY-VCH Verlag GmbH & Co.

Cui, Xiaoqing, Xian Fang, Hong Zhao, Zengxi Li, and Hongxuan Ren. 2017. "An electrochemical sensor for dopamine based on polydopamine modified reduced graphene oxide anchored with tin dioxide and gold nanoparticles." *Analytical Methods* 9 (36):5322-5332. doi: 10.1039/C7AY00991G.

Dai, Xiangzi, Shuping Wu, and Songjun Li. 2018. "Progress on electrochemical sensors for the determination of heavy metal ions from contaminated water." *Journal of the Chinese Advanced Materials Society* 6 (2):91-111. doi: 10.1080/22243682.2018.1425904.

Dar, M. Abdullah, Khalid Mujasam Batoo, Vivek Verma, W. A. Siddiqui, and R. K. Kotnala. 2010. "Synthesis and characterization of nano-sized pure and Al-doped lithium ferrite having high value of dielectric constant." *Journal of Alloys and Compounds* 493 (1):553-560. doi: http://dx.doi.org/10.1016/j.jallcom.2009.12.154.

DeBoer, Frank E., and P. W. Selwood. 1954. "The Activation Energy for the Solid State Reaction γ-Fe2O3 → α-Fe2O3." *Journal of the American Chemical Society* 76 (13):3365-3367. doi: 10.1021/ja01642a003.

Deng, Yuan, Li Liu, Yue Cheng, Ce-Wen Nan, and Shu-jing Zhao. 2003. "Hydrothermal synthesis and characterization of nanocrystalline PZT powders." *Materials Letters* 57 (11):1675-1678. doi: https://doi.org/10.1016/S0167-577X(02)01050-9.

Ding, Rui, LeiLei Lv, Li Qi, Mingjun Jia, and Hongyu Wang. 2015. "Correction: A facile hard-templating synthesis of mesoporous spinel CoFe2O4 nanostructures as promising electrocatalysts for the H2O2 reduction reaction." *RSC Advances* 5 (48):37978-37978. doi: 10.1039/C5RA90036K.

Elmoussaoui, H., M. Hamedoun, O. Mounkachi, A. Benyoussef, R. Masrour, and E. K. Hlil. 2012. "New results on Magnetic Properties of Tin-Ferrite Nanoparticles." *Journal of Superconductivity and Novel Magnetism* 25 (6):1995-2002. doi: 10.1007/s10948-012-1547-8.

Fan, Mouping, Haiying Yu, and Yu Chen. 2017. "High-capacity sodium ion battery anodes based on CuO nanosheets and carboxymethyl cellulose binder." *Materials Technology* 32 (10):598-605. doi: 10.1080/10667857.2017.1295628.

Farid, Hafiz Muhammad Tahir, Ishtiaq Ahmad, Irshad Ali, Shahid M. Ramay, Asif Mahmood, and G. Murtaza. 2017. "Dielectric and impedance study of praseodymium substituted Mg-based spinel ferrites." *Journal of Magnetism and Magnetic Materials* 434:143-150. doi: http://dx.doi.org/10.1016/j.jmmm.2017.03.039.

Fawzi, Abdul Samee, A. D. Sheikh, and V. L. Mathe. 2010. "Structural, dielectric properties and AC conductivity of Ni(1−x)ZnxFe2O4 spinel ferrites." *Journal of Alloys and Compounds* 502 (1):231-237. doi: https://doi.org/10.1016/j.jallcom.2010.04.152.

Fayemi, Omolola E., Abolanle S. Adekunle, B. E. Kumara Swamy, and Eno E. Ebenso. 2018. "Electrochemical sensor for the detection of dopamine in real samples using polyaniline/NiO, ZnO, and Fe3O4 nanocomposites on glassy carbon electrode." *Journal of Electroanalytical Chemistry* 818:236-249. doi: https://doi.org/10.1016/j.jelechem.2018.02.027.

Feueerbach, Ann. 2005. An investigation of valid technology ound in swords, sabres and blades from the Russian Northern caucasus. In *IAMS*.

Ganesh, V., S. Pitchumani, and V. Lakshminarayanan. 2006. "New symmetric and asymmetric supercapacitors based on high surface area porous nickel and activated carbon." *Journal of Power Sources* 158 (2):1523-1532. doi: http://dx.doi.org/10.1016/j.jpowsour.2005.10.090.

Gao, Hongyan, Shuai Liu, Yafei Li, Eric Conte, and Yan Cao. 2017. "A Critical Review of Spinel Structured Iron Cobalt Oxides Based Materials for Electrochemical Energy Storage and Conversion." *Energies* 10 (11):1787.

Gatelytė, Aurelija, Darius Jasaitis, Aldona Beganskienė, and Aivaras Kareiva. 2011. *Sol-Gel Synthesis and Characterization of Selected Transition Metal Nano-Ferrites*. Vol. 17.

Ghodake, U. R., Rahul C. Kambale, and S. S. Suryavanshi. 2017. "Effect of Mn2+ substitution on structural, electrical transport and dielectric properties of Mg-Zn ferrites." *Ceramics International* 43 (1, Part B):1129-1134. doi: https://doi.org/10.1016/j.ceramint.2016.10.053.

Hankare, P. P., R. P. Patil, U. B. Sankpal, K. M. Garadkar, R. Sasikala, A. K. Tripathi, and I. S. Mulla. 2010. "Magnetic, dielectric and complex impedance spectroscopic studies of nanocrystalline Cr substituted Li-ferrite." *Journal of Magnetism and Magnetic Materials* 322 (18):2629-2633. doi: https://doi.org/10.1016/j.jmmm.2010.03.005.

Hao, Jinhui, Wenshu Yang, Zhe Zhang, Baoping Lu, Bailin Zhang, and Jilin Tang. 2015. "Facile Synthesis of 3D Hierarchical Flower-like Co3-xFexO4 ferrite on Nickel Foam as High-Performance Electrodes for Supercapacitors." *Electrochimica Acta* 152:13-18. doi: https://doi.org/10.1016/j.electacta.2014.11.104.

Haque, Saif Ul, Kallol Kumar Saikia, G. Murugesan, and S. Kalainathan. 2017. "A study on dielectric and magnetic properties of lanthanum substituted cobalt ferrite." *Journal of Alloys and Compounds* 701:612-618. doi: http://dx.doi.org/10.1016/j.jallcom.2016.11.309.

Hassoun, Jusef, Francesco Bonaccorso, Marco Agostini, Marco Angelucci, Maria Grazia Betti, Roberto Cingolani, Mauro Gemmi, Carlo Mariani, Stefania Panero, Vittorio Pellegrini, and Bruno Scrosati. 2014. "An Advanced Lithium-Ion Battery Based on a Graphene Anode and a Lithium Iron Phosphate Cathode." *Nano Letters* 14 (8):4901-4906. doi: 10.1021/nl502429m.

Huang, Ming, Fei Li, Fan Dong, Yu Xin Zhang, and Li Li Zhang. 2015. "MnO2-based nanostructures for high-performance supercapacitors." *Journal of Materials Chemistry A* 3 (43):21380-21423. doi: 10.1039/C5TA05523G.

Islam, Mobinul, Ghulam Ali, Min-Gi Jeong, Wonchang Choi, Kyung Yoon Chung, and Hun-Gi Jung. 2017. "Study on the Electrochemical Reaction Mechanism of NiFe2O4 as a High-Performance Anode for Li-Ion Batteries." *ACS Applied Materials & Interfaces* 9 (17):14833-14843. doi: 10.1021/acsami.7b01892.

Ismail, Fatma M., Mohamed Ramadan, Ahmed M. Abdellah, Ibrahim Ismail, and Nageh K. Allam. 2018. "Mesoporous spinel manganese zinc ferrite for high-performance supercapacitors." *Journal of Electroanalytical Chemistry* 817:111-117. doi: https://doi.org/10.1016/j.jelechem.2018.04.002.

Jaime-González, J., E. Mazario, N. Menendez, J. Sanchez-Marcos, A. Muñoz-Bonilla, and P. Herrasti. 2016. "Comparison of ferrite nanoparticles obtained electrochemically for catalytical reduction of hydrogen peroxide." *Journal of Solid State Electrochemistry* 20 (4):1191-1198. doi: 10.1007/s10008-015-2938-0.

Jayant Kolte1, Paresh H. Salame2, A. S. Daryapurkar1, and P. Gopalan. 2015. "Impedance and AC conductivity study of nano crystalline, fine grained multiferroic bismuth ferrite (BiFeO3), synthesized by microwave sintering." *AIP Advances* 5 (9):097164. doi: 10.1063/1.4931818.

Joshi, Seema, Manoj Kumar, Sandeep Chhoker, Arun Kumar, and Mahavir Singh. 2017. "Effect of Gd3+ substitution on structural, magnetic, dielectric and optical properties of nanocrystalline CoFe2O4." *Journal of Magnetism and Magnetic Materials* 426:252-263. doi: https://doi.org/10.1016/j.jmmm.2016.11.090.

Jotania, Rajshree B., Reshma A. Nandotaria, Chetna C. Chauhan, Mohd Hashim, Sher Singh Meena, and Sagar E. Shirsath. 2016. "Structural phases and Maxwell–Wagner relaxation in magnetically soft-ZnFe2O4 and hard-Sr2Cu2Fe12O22 nanocomposites." *Ceramics International* 42 (2, Part A):2289-2298. doi: https://doi.org/10.1016/j.ceramint.2015.10.023.

K, Bindu, Kishore Sridharan, Ajith K M, H. N. Lim, and H. S. Nagaraja. 2016. "Microwave assisted growth of stannous ferrite microcubes as electrodes for potentiometric nonenzymatic H2O2 sensor and supercapacitor applications." *Electrochimica Acta* 217:139-149. doi: http://dx.doi.org/10.1016/j.electacta.2016.09.083.

Kadam, S. L., K. K. Patankar, C. M. Kanamadi, and B. K. Chougule. 2004. "Electrical conduction and magnetoelectric effect in Ni0.50 Co0.50 Fe2O4 + Ba0.8 Pb0.2TiO3 composites." *Materials Research Bulletin* 39 (14):2265-2272. doi: http://dx.doi.org/10.1016/j.materresbull.2004.07.021.

Kalaie, Mohammad Reza, Amir Ali Youzbashi, Mohammad Ali Meshkot, and Farzad Hosseini-Nasab. 2016. "Preparation and characterization of superparamagnetic nickel oxide particles by chemical route." *Applied Nanoscience* 6 (6):789-795. doi: 10.1007/s13204-015-0498-3.

Kamali, Saeed, Nesa Shahmiri, José S. Garitaonandia, Jonas Ångström, Martin Sahlberg, Tore Ericsson, and Lennart Häggström. 2013. "Effect of mixing tool on magnetic properties of hematite nanoparticles prepared by sol–gel method." *Thin Solid Films* 534:260-264. doi: http://dx.doi.org/10.1016/j.tsf.2013.03.009.

Kambale, R. C., P. A. Shaikh, C. H. Bhosale, K. Y. Rajpure, and Y. D. Kolekar. 2009. "Dielectric properties and complex impedance spectroscopy studies of mixed Ni–Co ferrites." *Smart Materials and Structures* 18 (8):085014.

Khan, Ibrahim, Khalid Saeed, and Idrees Khan. 2017. "Nanoparticles: Properties, applications and toxicities." *Arabian Journal of Chemistry*. doi: https://doi.org/10.1016/j.arabjc.2017.05.011.

Khomenko, V., E. Frackowiak, V. Barsukov, and F. Béguin. 2006. "DEVELOPMENT OF SUPERCAPACITORS BASED ON CONDUCTING POLYMERS." Dordrecht.

Kivrak, Hilal, Orhan Alal, and Dilan Atbas. 2015. "Efficient and rapid microwave-assisted route to synthesize Pt–MnOx hydrogen peroxide sensor." *Electrochimica Acta* 176:497-503. doi: http://dx.doi.org/10.1016/j.electacta.2015.06.151.

Kōō, Iwauchi. 1971. "Dielectric Properties of Fine Particles of Fe 3 O 4 and Some Ferrites." *Japanese Journal of Applied Physics* 10 (11):1520.

Koops, C. G. 1951. "On the Dispersion of Resistivity and Dielectric Constant of Some Semiconductors at Audiofrequencies." *Physical Review* 83 (1):121-124.

Kopanja, Lazar, Irena Milosevic, Matjaz Panjan, Vesna Damnjanovic, and Marin Tadic. 2016. "Sol–gel combustion synthesis, particle shape analysis and

magnetic properties of hematite (α-Fe2O3) nanoparticles embedded in an amorphous silica matrix." *Applied Surface Science* 362:380-386. doi: http://dx.doi.org/10.1016/j.apsusc.2015.11.238.

Kumar, P. Ramesh, and Sagar Mitra. 2013. "Nickel ferrite as a stable, high capacity and high rate anode for Li-ion battery applications." *RSC Advances* 3 (47):25058-25064. doi: 10.1039/C3RA44001J.

Kumar, S., K. M. Batoo, R. Prakash, H. K. Choi, B. H. Koo, J. I. Song, H. Chung, H. Jeong, and C. G. Lee. 2010. "Impedance spectroscopy study on Mn1+xFe2−2xTixO4 (0⩽x⩽0.5) ferrites." *Journal of Central South University of Technology* 17 (6):1133-1138. doi: 10.1007/s11771-010-0608-z.

Kumbhar, V. S., A. D. Jagadale, N. M. Shinde, and C. D. Lokhande. 2012. "Chemical synthesis of spinel cobalt ferrite (CoFe2O4) nano-flakes for supercapacitor application." *Applied Surface Science* 259:39-43. doi: https://doi.org/10.1016/j.apsusc.2012.06.034.

Lavela, P., and J. L. Tirado. 2007. "CoFe2O4 and NiFe2O4 synthesized by sol–gel procedures for their use as anode materials for Li ion batteries." *Journal of Power Sources* 172 (1):379-387. doi: https://doi.org/10.1016/j.jpowsour.2007.07.055.

Lee, Hee Y., V. Manivannan, and J. B. Goodenough. 1999. "Electrochemical capacitors with KCl electrolyte." *Comptes Rendus de l'Académie des Sciences - Series IIC - Chemistry* 2 (11):565-577. doi: http://dx.doi.org/10.1016/S1387-1609(00)88567-9.

Lee, Jin Bae, Hae Jin Kim, Lu, #x17e, Janez nik, Andreja Jelen, Paji, #x107, Damir , Magdalena Wencka, Jagli, #x10d, #x107, Zvonko , Anton Meden, Dolin, #x161, and Janez ek. 2014. "Synthesis and Magnetic Properties of Hematite Particles in a “Nanomedusa” Morphology." *Journal of Nanomaterials* 2014:9. doi: 10.1155/2014/902968.

Lhommée, Eugénie, Alina Batir, Jean-Louis Quesada, Claire Ardouin, Valérie Fraix, Eric Seigneuret, Stéphan Chabardès, Alim-Louis Benabid, Pierre Pollak, and Paul Krack. 2014. "Dopamine and the biology of creativity: lessons from Parkinson's disease." *Frontiers in neurology* 5:55-55. doi: 10.3389/fneur.2014.00055.

Li, Mian, Yueping Xiong, Xiaotian Liu, Xiangjie Bo, Yufan Zhang, Ce Han, and Liping Guo. 2015. "Facile synthesis of electrospun MFe2O4 (M = Co, Ni, Cu, Mn) spinel nanofibers with excellent electrocatalytic properties for oxygen evolution and hydrogen peroxide reduction." *Nanoscale* 7 (19):8920-8930. doi: 10.1039/C4NR07243J.

Li, Songmei, Bo Wang, Jianhua Liu, and Mei Yu. 2014. "In situ one-step synthesis of CoFe2O4/graphene nanocomposites as high-performance anode for lithium-ion batteries." *Electrochimica Acta* 129:33-39. doi: https://doi.org/10.1016/j.electacta.2014.02.039.

Lipparoni, F. R., F. Bonino, S. Panero, and B. Scrosati. 2002. "Electrochemical properties of metal oxides as anode materials for lithium ion batteries." *Ionics* 8 (3):177-182. doi: 10.1007/bf02376066.

Liu, Fangxin, Tongzhong Li, and Huagui Zheng. 2004. "Structure and magnetic properties of SnFe2O4 nanoparticles." *Physics Letters A* 323 (3):305-309. doi: https://doi.org/10.1016/j.physleta.2004.01.077.

Liu, Hongsheng, and Cristiana Di Valentin. 2017. "Band Gap in Magnetite above Verwey Temperature Induced by Symmetry Breaking." *The Journal of Physical Chemistry C* 121 (46):25736-25742. doi: 10.1021/acs.jpcc.7b09387.

Liu, Shixi, Bin Yue, Kun Jiao, Yan Zhou, and Heyong He. 2006. "Template synthesis of one-dimensional nanostructured spinel zinc ferrite." *Materials Letters* 60 (2):154-158. doi: https://doi.org/10.1016/j.matlet.2005.08.008.

Liu, Wei, Hongxiu Zhang, Bin Yang, Zhongjian Li, Lecheng Lei, and Xingwang Zhang. 2015. "A non-enzymatic hydrogen peroxide sensor based on vertical NiO nanosheets supported on the graphite sheet." *Journal of Electroanalytical Chemistry* 749:62-67. doi: http://dx.doi.org/10.1016/j.jelechem.2015.04.037.

Liu, Weiyan, Hongmei Yang, Chao Ma, Ya-nan Ding, Shenguang Ge, Jinghua Yu, and Mei Yan. 2014. "Graphene–palladium nanowires based electrochemical sensor using ZnFe2O4–graphene quantum dots as an effective peroxidase mimic." *Analytica Chimica Acta* 852:181-188. doi: https://doi.org/10.1016/j.aca.2014.08.054.

Liu, Xuyan, Xinjie Zhu, and Deng Pan. 2018. "Solutions for the problems of silicon-carbon anode materials for lithium-ion batteries." *Royal Society open science* 5 (6):172370-172370. doi: 10.1098/rsos.172370.

Liu, Y., D. Luo, K. Shi, X. Michaud, and I. Zhitomirsky. 2018. "Asymmetric supercapacitor based on MnO2 and Fe2O3 nanotube active materials and graphene current collectors." *Nano-Structures & Nano-Objects* 15:98-106. doi: https://doi.org/10.1016/j.nanoso.2017.08.010.

Lu, Haiting, Sheng Yu, Yang Fan, Chunpeng Yang, and Dongli Xu. 2013. "Nonenzymatic hydrogen peroxide electrochemical sensor based on carbon-coated SnO2 supported Pt nanoparticles." *Colloids and Surfaces B: Biointerfaces* 101:106-110. doi: http://dx.doi.org/10.1016/j.colsurfb.2012.05.033.

Lund, Carl R. F., and J. A. Dumesic. 1982. "Strong oxide-oxide interactions in silica-supported magnetite catalysts. 2. The core/shell nature of the interaction." *The Journal of Physical Chemistry* 86 (1):130-135. doi: 10.1021/j100390a027.

Lv, Xincong, Bo Hu, Zhenbing Wang, Jian Peng, and Jian Weng. 2015. "Two-Electron Oxidation of Dopamine Controlled by Surface Modification of Few-Layer Graphene." *Electrochimica Acta* 180:43-52. doi: https://doi.org/10.1016/j.electacta.2015.08.075.

Ma, Ren-Min, and Rupert F. Oulton. 2019. "Applications of nanolasers." *Nature Nanotechnology* 14 (1):12-22. doi: 10.1038/s41565-018-0320-y.

Ma, Zhaoling, Xiaobing Huang, Shuo Dou, Jianghong Wu, and Shuangyin Wang. 2014. "One-Pot Synthesis of Fe2O3 Nanoparticles on Nitrogen-Doped Graphene as Advanced Supercapacitor Electrode Materials." *The Journal of Physical Chemistry C* 118 (31):17231-17239. doi: 10.1021/jp502226j.

Mansour, S. F., and M. A. Abdo. 2017. "Electrical modulus and dielectric behavior of Cr3+ substituted Mg–Zn nanoferrites." *Journal of Magnetism and Magnetic Materials* 428:300-305. doi: http://dx.doi.org/10.1016/j.jmmm.2016.12.039.

Maqsood, Asghari, Kishwar Khan, M. Anis-ur-Rehman, and Muhammad Ali Malik. 2011. "Structural and Electrical Properties of Ni-Co Nanoferrites Prepared by Co-precipitation Route." *Journal of Superconductivity and Novel Magnetism* 24 (1):617-622. doi: 10.1007/s10948-010-0956-9.

Marinho, H. Susana, Carla Real, Luísa Cyrne, Helena Soares, and Fernando Antunes. 2014. "Hydrogen peroxide sensing, signaling and regulation of transcription factors." *Redox Biology* 2:535-562. doi: http://dx.doi.org/10.1016/j.redox.2014.02.006.

Medvedeva, O. I., S. S. Kambulova, O. V. Bondar, A. R. Gataulina, N. A. Ulakhovich, A. V. Gerasimov, V. G. Evtugyn, I. F. Gilmutdinov, and M. P. Kutyreva. 2017. "Magnetic Cobalt and Cobalt Oxide Nanoparticles in Hyperbranched Polyester Polyol Matrix." *Journal of Nanotechnology* 2017:9. doi: 10.1155/2017/7607658.

Miao, Yue- E., Sixin He, Yunlan Zhong, Zhe Yang, Weng Weei Tjiu, and Tianxi Liu. 2013. "A novel hydrogen peroxide sensor based on Ag/SnO2 composite nanotubes by electrospinning." *Electrochimica Acta* 99:117-123. doi: http://dx.doi.org/10.1016/j.electacta.2013.03.063.

Mikhaylova, Maria, Do Kyung Kim, Natalia Bobrysheva, Mikhail Osmolowsky, Valentin Semenov, Thomas Tsakalakos, and Mamoun Muhammed. 2004. "Superparamagnetism of Magnetite Nanoparticles: Dependence on Surface Modification." *Langmuir* 20 (6):2472-2477. doi: 10.1021/la035648e.

Milosevic, Irena, Hicham Jouni, Catalina David, Fabienne Warmont, Dominique Bonnin, and Laurence Motte. 2011. "Facile Microwave Process in Water for the Fabrication of Magnetic Nanorods." *The Journal of Physical Chemistry C* 115 (39):18999-19004. doi: 10.1021/jp205334v.

Mingos, D. Michael P. 1993. "Microwave syntheses of inorganic materials." *Advanced Materials* 5 (11):857-859. doi: 10.1002/adma.19930051115.

Mitra, Sagar, Pavan S. Veluri, Antara Chakraborthy, and Ramesh K. Petla. 2014. "Electrochemical Properties of Spinel Cobalt Ferrite Nanoparticles with Sodium Alginate as Interactive Binder." *ChemElectroChem* 1 (6):1068-1074. doi: doi:10.1002/celc.201400026.

Mitra, Subarna, Soumen Das, Soumen Basu, Puspendu Sahu, and Kalyan Mandal. 2009. "Shape- and field-dependent Morin transitions in structured α-Fe2O3." *Journal of Magnetism and Magnetic Materials* 321 (18):2925-2931. doi: http://dx.doi.org/10.1016/j.jmmm.2009.04.044.

Moradmard, H., S. Farjami Shayesteh, P. Tohidi, Z. Abbas, and M. Khaleghi. 2015. "Structural, magnetic and dielectric properties of magnesium doped nickel ferrite nanoparticles." *Journal of Alloys and Compounds* 650:116-122. doi: https://doi.org/10.1016/j.jallcom.2015.07.269.

Mousavi Ghahfarokhi, S. E., Z. A. Rostami, and I. Kazeminezhad. 2016. "Fabrication of PbFe12O19 nanoparticles and study of their structural, magnetic and dielectric properties." *Journal of Magnetism and Magnetic Materials* 399:130-142. doi: https://doi.org/10.1016/j.jmmm.2015.09.063.

Mujasam Batoo, Khalid. 2011. "Study of dielectric and impedance properties of Mn ferrites." *Physica B: Condensed Matter* 406 (3):382-387. doi: http://dx.doi.org/10.1016/j.physb.2010.10.075.

N., Rezlescu, and Rezlescu E. 1974. "Dielectric properties of copper containing ferrites." *physica status solidi (a)* 23 (2):575-582. doi: doi:10.1002/pssa.2210230229.

Ning, Lingyun, Xinglong Guan, Jingwen Ma, Min Wang, Xiaobin Fan, Guoliang Zhang, Fengbao Zhang, Wenchao Peng, and Yang Li. 2018. "A highly

sensitive nonenzymatic H2O2 sensor based on platinum, ZnFe2O4 functionalized reduced graphene oxide." *Journal of Alloys and Compounds* 738:317-322. doi: https://doi.org/10.1016/j.jallcom.2017.12.161.

Nobre, M. A. L., and S. Lanfredi. 2003. "Dielectric loss and phase transition of sodium potassium niobate ceramic investigated by impedance spectroscopy." *Catalysis Today* 78 (1):529-538. doi: https://doi.org/10.1016/S0920-5861(02)00349-8.

Pati, S. S., S. Gopinath, G. Panneerselvam, M. P. Antony, and John Philip. 2012. "High temperature phase transformation studies in magnetite nanoparticles doped with Co2+ ion." *Journal of Applied Physics* 112 (5):054320. doi: doi:http://dx.doi.org/10.1063/1.4748318.

Pati, S. S., L. Herojit Singh, J. C. Mantilla Ochoa, E. M. Guimarãesa, M. J. A. Sales, J. A. H. Coaquira, A. C. Oliveira, and V. K. Garg. 2015. "Facile approach to suppress γ -Fe 2 O 3 to α -Fe 2 O 3 phase transition beyond 600 °C in Fe 3 O 4 nanoparticles." *Materials Research Express* 2 (4):045003.

Pavithradevi, S., N. Suriyanarayanan, and T. Boobalan. 2017. "Synthesis, structural, dielectric and magnetic properties of polyol assisted copper ferrite nano particles." *Journal of Magnetism and Magnetic Materials* 426:137-143. doi: https://doi.org/10.1016/j.jmmm.2016.10.128.

Pervaiz, Erum, and I. H. Gul. 2014. "High frequency AC response, DC resistivity and magnetic studies of holmium substituted Ni-ferrite: A novel electromagnetic material." *Journal of Magnetism and Magnetic Materials* 349:27-34. doi: http://dx.doi.org/10.1016/j.jmmm.2013.08.011.

Praveena, K., K. Sadhana, and Hardev Singh Virk. 2015. "Structural and Magnetic Properties of Mn-Zn Ferrites Synthesized by Microwave-Hydrothermal Process." *Solid State Phenomena* 232:45-64. doi: 10.4028/www.scientific.net/SSP.232.45.

Puri, Maalti, Sukhleen Bindra Narang, and Shalini Bahel. 2018. "Influence of frequency and temperature on dielectric and electrical properties of Ca-substituted barium iron niobate." *Ceramics International* 44 (8):9112-9124. doi: https://doi.org/10.1016/j.ceramint.2018.02.119.

Qi, Chengcheng, and Jianbin Zheng. 2015. "Novel nonenzymatic hydrogen peroxide sensor based on Fe3O4/PPy/Ag nanocomposites." *Journal of Electroanalytical Chemistry* 747:53-58. doi: http://dx.doi.org/10.1016/j.jelechem.2015.04.004.

Qi, Wen, Joseph G. Shapter, Qian Wu, Ting Yin, Guo Gao, and Daxiang Cui. 2017. "Nanostructured anode materials for lithium-ion batteries: principle, recent progress and future perspectives." *Journal of Materials Chemistry A* 5 (37):19521-19540. doi: 10.1039/C7TA05283A.

Rajendra Prasad, Kalakodimi, and Norio Miura. 2004. "Electrochemically synthesized MnO2-based mixed oxides for high performance redox supercapacitors." *Electrochemistry Communications* 6 (10):1004-1008. doi: https://doi.org/10.1016/j.elecom.2004.07.017.

Ramesh, S., B. Dhanalakshmi, B. Chandra Sekhar, P. S. V. Subba Rao, and B. Parvatheeswara Rao. 2016. "Effect of Mn/Co substitutions on the resistivity and dielectric properties of nickel–zinc ferrites." *Ceramics International* 42 (8):9591-9598. doi: http://dx.doi.org/10.1016/j.ceramint.2016.03.043.

Rathod, V., A. V. Anupama, R. Vijaya Kumar, V. M. Jali, and B. Sahoo. 2017. "Correlated vibrations of the tetrahedral and octahedral complexes and splitting of the absorption bands in FTIR spectra of Li-Zn ferrites." *Vibrational Spectroscopy* 92:267-272. doi: https://doi.org/10.1016/j.vibspec.2017.08.008.

Rezlescu, N., and E. Rezlescu. 1974. "Dielectric properties of copper containing ferrites." *physica status solidi (a)* 23 (2):575-582. doi: 10.1002/pssa.2210230229.

Rosso, Kevin M., Dayle M. A. Smith, and Michel Dupuis. 2003. "An ab initio model of electron transport in hematite (α-Fe2O3) basal planes." *The Journal of Chemical Physics* 118 (14):6455-6466. doi: 10.1063/1.1558534.

S. S. Pati, S. Gopinath, G. Panneerselvam, and M. P. Antony, and John Philip. 2012. "High temperature phase transformation studies in magnetite nanoparticles doped with Co2+ ion." *Journal of Applied Physics* 112 (5):054320. doi: 10.1063/1.4748318.

Salunkhe, Ashwini B., Vishwajeet M. Khot, Juan M. Ruso, and S. I. Patil. 2016. "Water dispersible superparamagnetic Cobalt iron oxide nanoparticles for magnetic fluid hyperthermia." *Journal of Magnetism and Magnetic Materials* 419:533-542. doi: https://doi.org/10.1016/j.jmmm.2016.06.057.

Sankar, Kalimuthu Vijaya, D. Kalpana, and Ramakrishnan Kalai Selvan. 2012. "Electrochemical properties of microwave-assisted reflux-synthesized Mn3O4 nanoparticles in different electrolytes for supercapacitor applications." *Journal of Applied Electrochemistry* 42 (7):463-470. doi: 10.1007/s10800-012-0424-2.

Sattar, A., A., and K. El-Shokrofy, M. 1997. "Rare Earth Doping Effect on the Electrical Properties of Cu-ZnFerrites." *J. Phys. IV France* 07 (C1):C1-245-C1-246.

Shanmugavani, A., and R. Kalai Selvan. 2014. "Synthesis of ZnFe2O4 nanoparticles and their asymmetric configuration with Ni(OH)2 for a pseudocapacitor." *RSC Advances* 4 (51):27022-27029. doi: 10.1039/c4ra01793e.

Shen, Wei, Leihao Zhang, Bowen Zhao, Yichun Du, and Xing Zhou. 2018. "Growth mechanism of octahedral like nickel ferrite crystals prepared by modified hydrothermal method and morphology dependent magnetic performance." *Ceramics International* 44 (8):9809-9815. doi: https://doi.org/10.1016/j.ceramint.2018.02.219.

Shimizu, K., K. Tschulik, and R. G. Compton. 2016. "Exploring the mineral-water interface: reduction and reaction kinetics of single hematite ([small alpha]-Fe2O3) nanoparticles." *Chemical Science* 7 (2):1408-1414. doi: 10.1039/c5sc03678j.

Sidhu, P. S., R. J. Gilkes, and A. M. Posner. 1978. "The synthesis and some properties of Co, Ni, Zn, Cu, Mn and Cd substituted magnetites." *Journal of Inorganic and Nuclear Chemistry* 40 (3):429-435. doi: https://doi.org/10.1016/0022-1902(78)80418-7.

Sidhu, P. S., R. J. Gilkes, and A. M. Posner. 1980. "The Behavior of Co, Ni, Zn, Cu, Mn, and Cr in Magnetite during Alteration to Maghemite and Hematite1." *Soil Science Society of America Journal* 44 (1):135-138. doi: 10.2136/sssaj1980.03615995004400010028x.

Singh, Navneet, Ashish Agarwal, Sujata Sanghi, and Paramjeet Singh. 2011. "Effect of magnesium substitution on dielectric and magnetic properties of Ni–Zn ferrite." *Physica B: Condensed Matter* 406 (3):687-692. doi: https://doi.org/10.1016/j.physb.2010.11.087.

Skinner, H. C. W., and A. H. Jahren. 2007. "8.04 - Biomineralization." In *Treatise on Geochemistry*, edited by Heinrich D. Holland and Karl K. Turekian, 1-69. Oxford: Pergamon.

Sonia, M. Maria Lumina, S. Anand, V. Maria Vinosel, M. Asisi Janifer, S. Pauline, and A. Manikandan. 2018. "Effect of lattice strain on structure, morphology and magneto-dielectric properties of spinel NiGdxFe2-xO4 ferrite nano-crystallites synthesized by sol-gel route." *Journal of Magnetism and Magnetic Materials*. doi: https://doi.org/10.1016/j.jmmm.2018.07.017.

Spencer, Elinor C., Nancy L. Ross, Rebecca E. Olsen, Baiyu Huang, Alexander I. Kolesnikov, and Brian F. Woodfield. 2015. "Thermodynamic Properties of α-Fe2O3 and Fe3O4 Nanoparticles." *The Journal of Physical Chemistry C* 119 (17):9609-9616. doi: 10.1021/acs.jpcc.5b01481.

Sreejesh, M., N. M. Huang, and H. S. Nagaraja. 2015. "Solar Exfoliated Graphene and its Application in Supercapacitors and Electrochemical H2O2 Sensing." *Electrochimica Acta* 160:94-99. doi: http://dx.doi.org/10.1016/j.electacta.2015.02.005.

Sridhar, Ch S. L. N., Ch S. Lakshmi, G. Govindraj, S. Bangarraju, L. Satyanarayana, and D. M. Potukuchi. 2016. "Structural, morphological, magnetic and dielectric characterization of nano-phased antimony doped manganese zinc ferrites." *Journal of Physics and Chemistry of Solids* 92:70-84. doi: https://doi.org/10.1016/j.jpcs.2016.01.006.

Sridharan, Kishore, Eunyong Jang, and Tae Joo Park. 2013. "Deformation assisted fabrication of uniform spindle, tube and rod shaped nanoscale 3D TiO2 architectures and their photocatalytic activity." *CrystEngComm* 15 (41):8241-8245. doi: 10.1039/c3ce41481g.

Sridharan, Kishore, and Tae Joo Park. 2013. "Thorn-ball shaped TiO2 nanostructures: Influence of Sn2+ doping on the morphology and enhanced visible light photocatalytic activity." *Applied Catalysis B: Environmental* 134–135:174-184. doi: http://dx.doi.org/10.1016/j.apcatb.2013.01.017.

Srikrishna Ramya, S. I., and C. K. Mahadevan. 2014. "Preparation and structural, optical, magnetic, and electrical characterization of Mn2+/Co2+/Cu2+ doped hematite nanocrystals." *Journal of Solid State Chemistry* 211:37-50. doi: http://dx.doi.org/10.1016/j.jssc.2013.11.022.

Subramanian, V., Sean C. Hall, Patricia H. Smith, and B. Rambabu. 2004. "Mesoporous anhydrous RuO2 as a supercapacitor electrode material." *Solid State Ionics* 175 (1):511-515. doi: https://doi.org/10.1016/j.ssi.2004.01.070.

Tadić, Marin, Nada Čitaković, Matjaž Panjan, Zoran Stojanović, Dragana Marković, and Vojislav Spasojević. 2011. "Synthesis, morphology, microstructure and magnetic properties of hematite submicron particles." *Journal of Alloys and Compounds* 509 (28):7639-7644. doi: http://dx.doi.org/10.1016/j.jallcom.2011.04.117.

Taffa, Dereje H., Ralf Dillert, Anna C. Ulpe, Katharina C. L. Bauerfeind, Thomas Bredow, Detlef W. Bahnemann, and Michael Wark. 2016.

"Photoelectrochemical and theoretical investigations of spinel type ferrites (M_xFe₃_{−x}O₄) for water splitting: a mini-review."
Tamirat, Andebet Gedamu, John Rick, Amare Aregahegn Dubale, Wei-Nien Su, and Bing-Joe Hwang. 2016. "Using hematite for photoelectrochemical water splitting: a review of current progress and challenges." *Nanoscale Horizons* 1 (4):243-267. doi: 10.1039/C5NH00098J.
Topal, Uğur, and Mehmet Ali Aksan. 2016. "Phase stabilization of magnetite (Fe3O4) nanoparticles with B2O3 addition: A significant enhancement on the phase transition temperature." *Journal of Magnetism and Magnetic Materials* 406:123-128. doi: https://doi.org/10.1016/j.jmmm.2016.01.007.
Umapathy, G., G. Senguttuvan, L. John Berchmans, and V. Sivakumar. 2016. "Structural, dielectric and AC conductivity studies of Zn substituted nickel ferrites prepared by combustion technique." *Journal of Materials Science: Materials in Electronics* 27 (7):7062-7072. doi: 10.1007/s10854-016-4664-5.
Vara Prasad, B. B. V. S., K. V. Ramesh, and Adiraj Srinivas. 2018. "Structural and magnetic properties of nanocrystalline nickel ferrite (NiFe2O4) synthesized in sol-gel and combustion routes." *Solid State Sciences* 86:86-97. doi: https://doi.org/10.1016/j.solidstatesciences.2018.10.008.
Vijatović Petrović, M. M., R. Grigalaitis, A. Dzunuzovic, J. D. Bobić, B. D. Stojanović, R. Šalaševičius, and J. Banys. 2018. "Positive influence of Sb doping on properties of di-phase multiferroics based on barium titanate and nickel ferrite." *Journal of Alloys and Compounds* 749:1043-1053. doi: https://doi.org/10.1016/j.jallcom.2018.03.381.
Voepel, P., C. Suchomski, A. Hofmann, S. Gross, P. Dolcet, and B. M. Smarsly. 2016. "In-depth mesocrystal formation analysis of microwave-assisted synthesis of LiMnPO4 nanostructures in organic solution." *CrystEngComm* 18 (2):316-327. doi: 10.1039/c5ce01946j.
Vulcu, Adriana, Alexandru Radu Biris, Gheorghe Borodi, and Camelia Berghian-Grosan. 2018. "Interference of ascorbic and uric acids on dopamine behavior at graphene composite surface: An electrochemical, spectroscopic and theoretical approach." *Electrochimica Acta* 282:822-834. doi: https://doi.org/10.1016/j.electacta.2018.06.122.
Wang, G. X., Y. Chen, K. Konstantinov, Jane Yao, Jung-ho Ahn, H. K. Liu, and S. X. Dou. 2002. "Nanosize cobalt oxides as anode materials for lithium-ion batteries." *Journal of Alloys and Compounds* 340 (1):L5-L10. doi: https://doi.org/10.1016/S0925-8388(02)00005-1.
Wang, Hongkang, Kunpeng Dou, Wey Yang Teoh, Yawen Zhan, Tak Fu Hung, Feihu Zhang, Jiaqiang Xu, Ruiqin Zhang, and Andrey L. Rogach. 2013. "Engineering of Facets, Band Structure, and Gas-Sensing Properties of Hierarchical Sn2+-Doped SnO2 Nanostructures." *Advanced Functional Materials* 23 (38):4847-4853. doi: 10.1002/adfm.201300303.
Wang, Lei, Zhidong Li, Yin Liang, and Kunyu Zhao. 2014. "Characterization and electromagnetic properties of Ni1−xCuxFe2O4 nanoparticle ferrites synthesized by using egg white." *Advanced Powder Technology* 25 (5):1510-1515. doi: https://doi.org/10.1016/j.apt.2014.04.006.

Wang, Lu, Hongmei Ji, Shasha Wang, Lijuan Kong, Xuefan Jiang, and Gang Yang. 2013. "Preparation of Fe3O4 with high specific surface area and improved capacitance as a supercapacitor." *Nanoscale* 5 (9):3793-3799. doi: 10.1039/c3nr00256j.

Wang, Luyuan Paul, Zhao Yi, Chao Wei, Wong Chuiling, Madhavi Srinivasan, and Zhichuan Xu. 2015. *Polycrystalline zinc stannate as anode material for sodium-ion batteries*. Vol. 3.

Wang, Rongyue, Qun Li, Lulu Cheng, Hongliang Li, Baoyan Wang, X. S. Zhao, and Peizhi Guo. 2014. "Electrochemical properties of manganese ferrite-based supercapacitors in aqueous electrolyte: The effect of ionic radius." *Colloids and Surfaces A: Physicochemical and Engineering Aspects* 457:94-99. doi: http://dx.doi.org/10.1016/j.colsurfa.2014.05.059.

Wang, Wei-Wei, and Jia-Liang Yao. 2012. "Effect of metal ions (Sn and Zn) on the thermal property of akaganeite nanorods." *Materials Research Bulletin* 47 (7):1762-1767. doi: http://dx.doi.org/10.1016/j.materresbull.2012.03.030.

Wang, Wenjuan, Qingli Hao, Wu Lei, Xifeng Xia, and Xin Wang. 2014. "Ternary nitrogen-doped graphene/nickel ferrite/polyaniline nanocomposites for high-performance supercapacitors." *Journal of Power Sources* 269:250-259. doi: http://dx.doi.org/10.1016/j.jpowsour.2014.07.010.

Wiberg, Egon, Nils Wiberg, and Arnold Frederick Holleman. *Inorganic Chemistry. 2001*, *Academic Press*.

Wolfenstine, J., and J. Allen. 2005. "Ni3+/Ni2+ redox potential in LiNiPO4." *Journal of Power Sources* 142 (1):389-390. doi: https://doi.org/10.1016/j.jpowsour.2004.11.024.

Xing, Zheng, Zhicheng Ju, Jian Yang, Huayun Xu, and Yitai Qian. 2012. "One-step hydrothermal synthesis of ZnFe2O4 nano-octahedrons as a high capacity anode material for Li-ion batteries." *Nano Research* 5 (7):477-485. doi: 10.1007/s12274-012-0233-2.

Xu, Gang, Lingling Li, Zhenju Shen, Zhihong Tao, Yi Zhang, He Tian, Xiao Wei, Ge Shen, and Gaorong Han. 2015. "Magnetite Fe3O4 nanoparticles and hematite α-Fe2O3 uniform oblique hexagonal microdisks, drum-like particles and spindles and their magnetic properties." *Journal of Alloys and Compounds* 629:36-42. doi: http://dx.doi.org/10.1016/j.jallcom.2014.11.140.

Yang, Zhiwei, Yizao Wan, Guangyao Xiong, Deying Li, Qiuping Li, Chunying Ma, Ruisong Guo, and Honglin Luo. 2015. "Facile synthesis of ZnFe2O4/reduced graphene oxide nanohybrids for enhanced microwave absorption properties." *Materials Research Bulletin* 61:292-297. doi: https://doi.org/10.1016/j.materresbull.2014.10.004.

Yardımcı, Feyza S., Mehmet Şenel, and Abdülhadi Baykal. 2012. "Amperometric hydrogen peroxide biosensor based on cobalt ferrite–chitosan nanocomposite." *Materials Science and Engineering: C* 32 (2):269-275. doi: https://doi.org/10.1016/j.msec.2011.10.028.

Ye, Haitao, Richard B. Jackman, and Peter Hing. 2003. "Spectroscopic impedance study of nanocrystalline diamond films." *Journal of Applied Physics* 94 (12):7878-7882. doi: 10.1063/1.1622998.

Zhang, Chunmei, Lei Li, Jian Ju, and Wei Chen. 2016. "Electrochemical Sensor Based on Graphene-Supported Tin Oxide Nanoclusters for Nonenzymatic

Detection of Hydrogen Peroxide." *Electrochimica Acta* 210:181-189. doi: http://dx.doi.org/10.1016/j.electacta.2016.05.151.

Zhang, Dongen, Zhiwei Tong, Gaoyang Xu, Shanzhong Li, and Juanjuan Ma. 2009. "Templated fabrication of NiFe2O4 nanorods: Characterization, magnetic and electrochemical properties." *Solid State Sciences* 11 (1):113-117. doi: https://doi.org/10.1016/j.solidstatesciences.2008.05.001.

Zhang, Dongen, Xiaojun Zhang, Xiaomin Ni, JiMei Song, and Huagui Zheng. 2006. "Low-temperature fabrication of MnFe2O4 octahedrons: Magnetic and electrochemical properties." *Chemical Physics Letters* 426 (1):120-123. doi: https://doi.org/10.1016/j.cplett.2006.05.100.

Zhang, Sai, and Jianbin Zheng. 2016. "Synthesis of single-crystal α-MnO2 nanotubes-loaded Ag@C core–shell matrix and their application for electrochemical sensing of nonenzymatic hydrogen peroxide." *Talanta* 159:231-237. doi: http://dx.doi.org/10.1016/j.talanta.2016.06.014.

Zhang, Xin, Yongan Niu, Xiangdong Meng, Yao Li, and Jiupeng Zhao. 2013. "Structural evolution and characteristics of the phase transformations between [small alpha]-Fe2O3, Fe3O4 and [gamma]-Fe2O3 nanoparticles under reducing and oxidizing atmospheres." *CrystEngComm* 15 (40):8166-8172. doi: 10.1039/C3CE41269E.

Zhang, Xuejun, and Qiaoling Li. 2008. "Microwave assisted hydrothermal synthesis and magnetic property of hematite nanorods." *Materials Letters* 62 (6):988-990. doi: http://dx.doi.org/10.1016/j.matlet.2007.07.029.

Zhang, Z., C. Boxall, and G. H. Kelsall. 1993. "Photoelectrophoresis of colloidal iron oxides 1. Hematite (α-Fe2O3)." *Colloids and Surfaces A: Physicochemical and Engineering Aspects* 73:145-163. doi: https://doi.org/10.1016/0927-7757(93)80013-5.

Zhao, Hongxiao, Zhi Zheng, Ka Wai Wong, Shumin Wang, Baojun Huang, and Dapeng Li. 2007. "Fabrication and electrochemical performance of nickel ferrite nanoparticles as anode material in lithium ion batteries." *Electrochemistry Communications* 9 (10):2606-2610. doi: https://doi.org/10.1016/j.elecom.2007.08.007.

Zheng, Yuanhui, Yao Cheng, Yuansheng Wang, Feng Bao, Lihua Zhou, Xiaofeng Wei, Yingying Zhang, and Qi Zheng. 2006. "Quasicubic α-Fe2O3 Nanoparticles with Excellent Catalytic Performance." *The Journal of Physical Chemistry B* 110 (7):3093-3097. doi: 10.1021/jp056617q.

Zhu, Chengzhou, Guohai Yang, He Li, Dan Du, and Yuehe Lin. 2015. "Electrochemical Sensors and Biosensors Based on Nanomaterials and Nanostructures." *Analytical Chemistry* 87 (1):230-249. doi: 10.1021/ac5039863.

Publications

1. **Bindu K**, Kishore Sridharan, Ajith K M, H.N. Lim, H.S. Nagaraja. "Microwave assisted growth of stannous ferrite microcubes as electrodes for potentiometric non-enzymatic H_2O_2 sensor and supercapacitor applications." **Electrochimica Acta,** Volume 217 (2016) 139–149.
2. Dhanush Shanbhag, **Bindu K**, AR Aarathy, Martha Ramesh, Sreejesh M, H S Nagaraja. "Hydrothermally synthesized reduced graphene oxide and Sn doped manganese dioxide nanocomposites for supercapacitors and dopamine sensors". **Materials today Energy,** Volume 4 (2017) 66-74.
3. **Bindu K**, K.M. Ajith, H.S. Nagaraja, "Electrical, dielectric and magnetic properties of Sn-doped hematite (α-SnxFe$_2$-xO$_3$) nanoplates synthesized by microwave-assisted method." **Journal of Alloys and Compounds**, Volume 735 (2018) 847-854.
4. S. Dhanush, M. Sreejesh, **Bindu K**, P. Chowdhury, H.S. Nagaraja, "Synthesis and electrochemical properties of silver dendrites and silver dendrites/rGO composite for applications in paracetamol sensing", **Materials Research Bulletin**, Volume 100, (2018) 295-301.
5. **Bindu K,** Ajith K M, Nagaraja H S. "Influence of cations on the dielectric properties of spinel ferrites", **Material research express**. Volume 6 (4) (2019) 045011.
6. Brijesh K, **Bindu K**, Dhanush Shanbhag, Nagaraja H S, "Chemically prepared Polypyrrole/$ZnWO_4$ nanocomposite electrodes for electrocatalytic water splitting" **International Journal of Hydrogen Energy**. Volume 44 (2) (2019) 757-767.
7. **Bindu K**, Nagaraja H S, "Temperature-dependant phase transformation of $Ni_xFe_{y-x}O_z$ nanoferrites: their dielectric and magnetic properties", **Applied Physics A.** (2019) 125: 448. https://doi.org/10.1007/s00339-019-2737-z.

8. **Bindu K**, Nagaraja H S. "Influence of cations in MFe_2O_4 (M: Fe, Zn, Ni, Sn) ferrite nanoparticles on the electrocatalytic activity in hydrogen peroxide sensor". **Material research express (Accepted manuscript)**

International conference:

- ✓ International Conference on Condensed Matter and Applied Physics organized by Dept. of Physics, Govt. Engineering college, Bikaner on 30-31st October 2015.

  Bindu K, P. Chowdhury, Ajith K M and H S Nagaraja, "Structural and Magnetic Studies of Tin Doped α-Fe_2O_3 (α-$Sn_xFe_{2-x}O_3$) Nanoparticles Prepared by Microwave Assisted Synthesis". *AIP conference proceedings 1728, 020276 (2016).*

- ✓ International conference on nanotechnology: Ideas, Innovations and Initiatives organized by Dept. of Mechanical and Industrial Engineering, IIT Roorkee, Roorkee, India.

Biodata

Bindu K

Research Scholar,

Material Research Laboratory,

Department of Physics,

National Institute of Technology Karnataka, Surathkal

Mangalore – 575 025

Mobile: 8105787220

e-mail: bindukphy@gmail.com

Education qualification

M.Sc. Department of Physics, Government Science College (Davanagere University), Chitradurga, Karnataka, India. (2010-2012)

B.Sc. Sahyadri Science College (Autonomous), Shivamogga, Karnnataka, India (2007-2010)